UNIVERSITÄT
BERN

Graduate School for Cellular and Biomedical Sciences

University of Bern

Statistical models of shape and density for population-based analysis of bone mechanics with applications to fracture risk assessment and implant design

PhD Thesis submitted by
Serena Bonaretti
from **Italy**
for the degree of
PhD in Biomedical Engineering

Supervisors
Dr. Mauricio Reyes and Dr. Philippe Büchler
Institute for Surgical Technology and Biomechanics
Medical Faculty of the University of Bern

Co-advisor
Prof. Daniel Rueckert
Department of Computing
Imperial College London

Accepted by the Medical Faculty, the Faculty of Science and the Vetsuisse Faculty of the University of Bern at the request of the Graduate School for Cellular and Biomedical Sciences

Bern, Dean of the Medical Faculty

Bern, Dean of the Faculty of Science

Bern, Dean of the Vetsuisse Faculty Bern

Thesis spervisors
Dr. Mauricio Reyes and **Dr. Philippe Büchler**
Institute for Surgical Technology and Biomechanics
University of Bern
Switzeland

Thesis co-advisor
Prof. Daniel Rueckert
Department of Computing
Imperial College London
United Kingdom

Thesis mentor
Prof. Stephen J. Ferguson
Institute for Biomechanics
Swiss Federal Institute of Technology Zürich
Switzerland

Thesis external co-referee
Dr. Enrico Schileo
Laboratory of Computational Bioengineering
Istituti Ortopedici Rizzoli Bologna
Italy

Acknowledgements

I thank Prof. Lutz P. Nolte for giving me the possibility to work on my project at the Institute for Surgical Technology and Biomechanics. I thank Dr. Mauricio Reyes for his continuous support at reaching my goals. I thank Dr. Philippe Bücher for teaching me the importance of good scientific communication. I thank Dr. Miguel González Ballester for guiding me at the very beginning of this project.

I thank Prof. Daniel Ruecker for his enthusiasm about my work ad his suggestions. I thank Prof. Stephen Ferguson for his interest in my thesis and his advices. I thank Dr. Enrico Schileo for accepting to review my thesis with great enthusiasm and interest.

I thank the Swiss National Science Foundation and its National Center of Competence in Research (SNSF-NCCR) on Computer Aided and Image Guided Medical Interventions (Co-Me), for founding my PhD project.

I thank Christof Seiler for sharing with me his enthusiasm for medical image analysis and for his help during these years. I thank Dr. Benedikt Helgason for teaching me the importance of details and for always allowing me to bother him, both in Bern and in Zürich. I thank Dr. Christelle Boichon for sharing the mesh morpher and for her continuos help. I thank Dr. Guoyan Zheng for our chats about the present and the future of medical image analysis.

I thank my colleagues, who constitute the interesting international environment of the ISTB. I thank the MIA and CB group guys. A special thank to Juhee, Maryam, Sa, Chrisi, Harry, Huan, Hyungmin, Thiago and Giacomo for having made my life warmer in this cold country.

I heartily thank my family and my dearest old friends who, just with their presence, keep reminding me the priorities of life.

Abstract

Fractures occur when bones can not withstand the applied forces. Among young people, fractures mainly occur during daily activities, whereas, among elderly, fractures occur for bone reduction diseases, like osteoporosis. In case of fractures, surgery is needed to accelerate the healing process. Such surgical interventions require implants to be fixed to bones in order to restore bone anatomy and function.

Experimental and modeling studies have been done to investigate bone response to applied loads. The mechanical behaviour of bone and of bone-implant coupling is usually assessed on a small amount of subjects. For both experimental and modeling investigations, it is difficult to have at disposal large datasets, therefore subject-specific studies are usually performed. The main limitations of subject-specific studies are the impossibility of handling population variability in a rational way, and the difficulty of generalizing findings to a broader population. These limitations can be overcome through population-based studies. Population-based studies can be possible using statistical models. Statistical models describe mathematically the intrinsic variability of the original dataset and allow the generation of large datasets of plausible new instances. Statistical models of appearance describe bone variability in terms of shape and mineral density. Instances created from statistical appearance models represent samples of the original dataset distribution, and contain combinations of shape and mineral density variability.

The first aim of the thesis was to evaluate two different approaches for the creation of statistical appearance models, in order to assess the most suitable for bone finite element simulations. For the creation of statistical models, the main technical challenge consists in the detection of anatomical correspondences. Correspondences can be detected using either mesh morphing algorithm or image registration techniques. The choice of one of these methods leads to the creation of mesh-based or image-based approaches for statistical appearance models. From the comparison of the two approaches, it resulted that the image-based model performed better in terms of accuracy of the volume correspondence and final quality of the generated finite element meshes, whereas the mesh-based approach was able to produce isotopological meshes and performed better in terms of computational efficiency.

The second aim of the thesis was to explore the potential of statistical models for population-based studies. Two studies were performed on new instances created from the models, and mechanical responses were compared for different groups of populations. In the first study, femur fracture risk was evaluated for men and women, in two different configurations, stance and sideways fall. Women resulted to have statistically significant higher fracture risk than men. Influences of bone geometry, bone material properties and applied loading on the risk of fracture was also analyzed. The main fracture risk predictors resulted to be body weight and neck-shaft angle. In the second study, bone-plate coupling was assessed for two different ethnic groups, Asian and Caucasian. The coupling was evaluated in terms of both shape fitting and mechanical response.

Results showed better response for Caucasian than for Asian,in terms of both fitting and mechanical behavior.

This thesis investigated two methods for the creation of population-based studies for finite element modeling, using statistical models and presented two applications that confirmed the potential of the method. The use of statistical models for population-based finite element simulations opens new possibilities for mechanical studies and clinical applications.

Contents

1 Introduction **1**

1.1 Bones . . . 2
1.1.1 Bone fracture . . . 6
1.1.2 Bone functional adaptation . . . 9
1.1.3 Bone shapes . . . 11
1.1.4 Bone mechanics . . . 13
1.2 Finite element method in orthopaedics . . . 16
1.2.1 Patient-specific vs. population-based models . . . 20
1.3 Statistical models in orthopaedics . . . 21
1.3.1 Statistical models of shape, intensity and appearance . . . 21
1.3.2 Applications in bone mechanics . . . 24
1.4 Objectives and structure of the thesis . . . 25

2 Image-based vs. mesh-based statistical appearance model of the femur **27**

2.1 Introduction . . . 28
2.2 Materials and methods . . . 29
2.2.1 Image segmentation (step 1) . . . 30
2.2.2 Surface mesh creation (step 2) . . . 30
2.2.3 Correspondences establishment (step 3) . . . 31
2.2.4 Statistical models (step 4) . . . 32
2.2.5 Instantiation of new samples (step 5) . . . 32
2.2.6 Volume mesh creation (step 6) . . . 33
2.2.7 Models validation and comparison (step 7) . . . 33
2.3 Results . . . 34
2.3.1 Validation of the anatomical correspondence detection (step 3) . . . 34
2.3.2 Validation of the statistical appearance model (step 4) . . . 34
2.3.3 Validation of the creation of FE meshes for the new instances (step 5) . . . 37
2.3.4 Computational costs . . . 37
2.4 Discussion . . . 39

3 Statistical appearance model for fracture risk assessment **43**

3.1 Introduction . . . 44
3.2 Materials and methods . . . 45
3.2.1 Statistical appearance model . . . 46

3.2.2 Finite element model 46
3.2.3 Fracture risk calculation 48
3.3 Results 50
3.4 Discussion 57

4 Statistical shape model for orthopaedic implant design 59
4.1 Introduction 60
4.2 Material and method 60
4.2.1 Statistical model of the tibia 60
4.2.2 Fracture generation and propagation 61
4.2.3 Implant fitting 63
4.2.4 Biomechanical FE simulations 65
4.3 Results 66
4.4 Discussion 68

5 Conclusion and outlook 69

List of Figures

1.1 Bone hierarchical structure at different levels. Macrostructural: cortical and cancellous bone. Microstructural: trabeculae and Haversian system. Sub-microstructure: bone lamellae. Nanostructure: fibrillar with embedded mineral. Sub-nanostructure: constituent molecular structure, i.e. collagen molecules, minerals and proteins. (From [93].) 3

1.2 Bone macrostructure. Bone is composed by cortical and trabecular tissue. Cortical bone is mainly composed by cylindrical components defined osteons, whereas trabecular bones is mainly made by rods called trabeculae. (From http://www.gla.ac.uk/ibls/US/fab/tutorial/clinical/orhip.html and Marotti G., Summer school "Bone Cell and Tissue Mechanics", Udine, Italy, 2010.) 4

1.3 Bone structure. Components of cortical and trabecular bone. (From http://blog.dearbornschools.org/renkom/2011/02/09/microscopic-structure-of-bone/.) 5

1.4 Bone fracture. (a) Simple femur shaft fractures. (b) Bone healing process. (Modified from http://www.aofoundation.org/Pages/home.aspx and http://pathwiki.pbworks.com/w/page/14673867/Bone23-27.) 6

1.5 Fracture risk evaluation from medical images. (a) Areal region of interest in DXA. (b) Volumetric region of interest in QCT. (From http://healthwise-everythinghealth.blogspot.com/2010/08/osteoporosis-testing-with-dxa.html and [84].) 7

1.6 Bone plates. (a) Plate axial compression for bone reduction. Shape of the LCP hole and screws in detail. (b) Hand-held bending pliers. (c) Bending press for plate contouring. (Modified from [23, 22].) 9

1.7 Figure created by Culmann and von Meyer in 1867 which shows the parallel between the crene inner structure that Culmann was warking on (left) and the bone inner structure studied by Mayer (right). (From von Meyer, G.H., Arch. Anat. Physiol. Wiss. Med. Reichert DuBois-Reymonds Arch., 34, 615628, 1867.) . . . 10

1.8 Mechanical stimuli for bone functional adaptation. Different relationships between strains and numbers of cycle cause bone formation, equilibrium and resorption (left). Shaft section of Rubin's turkey ulna showing bone formation, equilibrium and resorption (right, from top to bottom). (Modified from [95] and [78].) . 10

1.9 Bone shapes. Bones can be divided in long, short, flat and irregular based on their shape. (From: http://massasoit-bio.net/courses/201/201_content/topicdir/skeletal/skeletal_RG/skeletal_RG2/skeletal_RG2.html.) 11

1.10 Long bone anatomy. Long bones are constituted by three main parts: epiphysis, metaphysis and diaphysis (left). Their outer layer is made by cortical bone, whereas their inside is composed by trabecular bone and marrow (right). (Modified from: [82] and http://www.sciencephoto.com/media/119084/enlarge.) 12

1.11 Stress-strain curves for trabecular and cortical bone in tension and compression. (Modified from [92, 67, 45].) 14

1.12 Groups of relationships between material properties and density for femur (a) and tibia (b) available in literature. The green line in the femur graph represents Morgan's law [80]. (Modified from [46].) 15

1.13 Four different generations of bone meshes. (a) 1972: Surface triangular mesh . (b) 1977: Eight-node volumetric mesh. (c) 1990: Voxel-based mesh. (d) 1990s: Tetrahedron mesh. (From [13, 117, 65, 120].) 17

1.14 Bone mechanical property assignment from CT images as suggested by [99]. CT intesities, ρ_{QCT} and ρ_{Ash} are measure of the mineral part of the bone, whereas ρ_{App} and E of the complete bone. 18

1.15 High correlation between the strains measured experimentally and the strain calculated with FEM when the Morgan's law is used. (From [101]). 19

1.16 Bone boundary condition measurements and representation. (a) In gait analysis test markers are applied to the subject in order to study the muscle load on bones in the lower limbs. (b) Instrumented hip implants. The implant is modified from a clinical implant (left) adding strain gauges and telemetric receptors (right). (c) Representation of the action of muscles on lower limbs bones. (Modified from [48, 6].) 20

1.17 New instances created from (a) a statistical shape model of tibia and (b) a statistical appearance model of femur. (Modified from [68, 89].) 23

2.1 Mesh-based (left) and image-based (right) statistical appearance model pipelines for the creation of femur finite element meshes. 30

2.2 Landmarks selection for mesh morphing. (a) Selection of four landmarks in the femur head (1: fovea of the femur; 2: posterior lateral femur neck: 3: greater trochanter; 4: small trochanter). (b) and (c) Selection of six landmarks in the femur condyles (anterior and posterior views) (5: lateral epicondyle; 6: medial epicondyle; 7: intercondyle ; 8: patellar surface of femur; 9: lateral condyle; 10: medial condyle). 31

2.3 Compactness of the statistical appearance models calculated with the mesh-based and the image-based approaches. 35

2.4 Validation of the statistical appearance model through representation (a) and generalization (b). For each metric, bone shape and intensity reconstruction errors are represented for both the mesh-based (left) and the image-based (right) approaches. 36

2.5 Comparison of tetrahedron edge ratio (a) and tetrahedron minimum angle (b) for the new instances, in both mesh-based and image-based approaches. Each symbol represents the average (x axis) and the standard deviation (y axis) of the metric for each mesh. 38

3.1 Boundary condition for the calculation of the femur fracture risk for (a) the stance situation and (b) the sideways fall situation. The forces are applied using the coordinate system x,y,z. The boundary conditions are considered in the coordinate system 1,2,3. In the boundary condition coordinate system, U represents the node displacement. 48

3.2 Bone parameters considered for fracture risk evaluation. (a) Geometrical measurement. AB = femur length; CD = femoral neck length; EF = femoral neck diameter; GH = femoral head diameter; α = neck-shaft angle (calculated between femoral axis (KB) and femoral neck length (CD)); β = anteversion angle (calculated between femoral neck length (CD) and posterior condyles (IJ)). (b) Mechanical properties measurements. The red ring represents the volumetric region of interest for the extraction of the Young's modulus. 49

3.3 Single regression between fracture risk and body weight, neck-shaft angle and Young's modulus in the stance configuration for (a) men and (b) women. 53

3.4 Single regression between fracture risk and body weight, neck-shaft angle and Young's modulus in the sideways fall configuration for (a) men and (b) women. . 54

3.5 Comparison between fracture risk measured from the finite element simulations and the fracture risk predicted by multivariate models for both men and female in (a) stance and (b) sideways falling configurations. 56

4.1 Map of the 13 bones created for each ethnic group through shape PCA. Axes correspond to the first and second mode of variation. Each point represents a bone created using the first (red points) and the second mode (blue points) or combining them (green points). The black point represents the mean bone. 61

4.2 Fracture generation and propagation. (a) Fracture generated as a black sagittal slice in the mean bone. (b) Propagation of the reference fracture to a bone instance using deformation fields. Notice the incomplete fracture. (c) Fracture surface created with Delaunay triangulation; a few voxels are still linked at the edge of the fracture. (d) Elimination of the linking voxels and creation of two completely split bone parts. 62

4.3 Delaunay triangulations. (a) Triangulation generated with the black voxels obtained through the deformation fields as vertices. (b) Triangulation generated with the surface voxels as vertices. 63

4.4 Oriented Bounding Box (OBB) decomposition of the implant shape used to measure deviation of the angle between the main axis of the bone and the lower part of the implant shape. Figure (a) shows a 4-level decomposition and figure (b) shows the main axis of the lower part of the implant obtained after applying a further OBB decomposition of the lower part of the implant. 64
4.5 Finite element mesh of the bone (including the fracture) with the implant. Beam elements used to model the screws are shown as blue lines. These elements are 'embedded' within the bone elements. 66
4.6 Maximal (right) and average (left) distance map for the Asian and Caucasian bone populations. Red indicated a small distance (0mm) and blue indicates a large bone/implant distance up to 7mm for the maximal distance in the Asian population. 67

List of Tables

1.1 Cortical and trabecular bone mechanical characteristics. 14

2.1 Evaluation of the anatomical correspondence detection results. (a) Surface measurement of correspondence. The Husdorff distance used for both the mesh-based and the image-based approached. (b) Volume measurement of correspondence. Mask overlapping used for the mesh-based approach, Dice coefficient used for the image-based approach. 34

2.2 Computational costs for the calculation the statistical models and the creation of the new instances for the mesh-based and the image-based pipeline. For the new instance generation, the shown time refers to the creation of one instance; in the image-based pipeline it refers to both the computation of the new CT image and the transformation to a FE mesh. 37

3.1 Compactness of the statistical appearance model for men and women subjects. . . 50

3.2 Measured bone geometry, bone mechanical properties, and applied force for men and women. 51

3.3 Single regression between fracture risk and bone parameters. (a) Stance situation. (b) Side-ways fall situation. For each gender, bone parameters are ordered considering the absolute values of the regression coefficients R^2. 52

3.4 Stepwise multiple regression between fracture risk and bone parameters. (a) Stance situation. (b) Side-ways fall situation. For each step, accumulated R^2 and p-value are indicated for the multiple regression models created with the selected variables. Slope coefficient refer to the model with all variables included. 55

4.1 Comparison of the biomechanical and geometrical variables between the Asian and the Caucasian models. The first row shows the average of the maximal bone/implant distance calculated using the image-based method described in sections 2-4, while the other two rows contain the average of the maximal von Mises stress in the plate and maximal principle stress in the screws. Variations are given in %. 67

Chapter 1

Introduction

When bones can not withstand the applied forces, fractures occur. Among young people, fractures mainly occur during routine activities for traumatic events, like occupational trauma, road accidents and sport-related injuries. To reduce the occurrence of these fractures, protective environments and equipments have been designed. Their aim is to minimize the difference between the load applied to the bone and the load that the bone can bear. Among the elderly, fractures mainly occur for diseases linked to age-related bone reduction, like osteoporosis. In this case, fractures occur for falls from standing height or during lifting activities [122] and they interest hip, spine and wrist [18]. Osteoporotic fractures occur mainly in women, but they cause higher mortality in men [18]. Interventions are mainly focused on fracture prevention, in terms of pharmacological and dietary actions [122]. Osteporotic fractures have a big incidence in medical intervention and costs. It has been estimated that in 2005, more than 2 millions osteoporotic fractures occured in the United States, with a total medical cost of $17 million. By 2025, annual fractures and costs will rise by almost 50%. It has been estimated that fractures will increase of 87% for people that are 65-74 years of age [18].

In order to prevent fractures, efforts have been made to understand how bones respond to mechanical loads. Experimental and modeling studies have been done to investigate the influence of bone geometry, bone material properties, and loading conditions. Investigation have been enhanced by the evolution of imaging techniques, which allow the representation of bones, the visualization of their inner architecture and the quantification of the bone mineral density. Studies have benefited also by the development of engineering models, which use bone geometry, material properties and loading conditions to calculate stress and strains in bones. The calculated mechanical behavior is then assessed comparing the findings with the results obtained in experimental studied [122].

In case of bone fracture, surgery is needed to restore bone anatomy and allow the bone to be loaded soon in order to heal. These tasks are accomplished thanks to the use of implants. Implants are usually designed combining measurements found in literature with tests on few cadaver bones. The resulting implants need then to be adapted to the patient bone shape during the surgery. Bone implants are in fact standardized both in term of shape and mechanical response.

The investigation of the mechanical behavior of bones and bone-implants is usually performed on a small amount of subjects. For experimental tests, it is difficult to have at disposal a large amount of human bones, since regulations are very strict in many countries. For mechanical simulations, processing is required on volumetric images to extract bone geometry and make it compatible with simulation software input formats. In particular, bone segmentation is often still

performed in a semiautomatic way, requiring high time costs. The use of a small amount of samples has two main limitations. On one hand, it is very difficult to take into account in a systematic way the variability of bone geometry and mechanical properties, that are present among different subjects. On the other hand, it is risky to generalize the findings to a broader population. In order to overcome these limitations, tools should be provided to create populations of subjects and perform fast and automatic processing of data.

The transition from patient-specific to population-based studies can be allowed by the use of statistical models. Statistical models of shape, intensity and appearance have been introduced in the medical image analysis field as a tool for describing the intrinsic variability of object datasets. They have gained a remarkable popularity due to their flexibility in different applications, like data analysis, image segmentation and 2D/3D reconstruction. Beyond the analysis of the training dataset variability, statistical models allow the generation of new instances, that are part of the same distribution as the initial data and whose variability can be controlled in a mathematical way. Therefore starting from datasets with different characteristics in terms of age, gender, ethnicity, etc., population groups can be created and population-based studies performed.

The present work aims at using statistical models for population-based studies of bone fracture risk and bone-implant fitting. The models are built considering bone variations in terms of shape and mechanical properties. An introduction to the thesis work is given in this chapter, which can be divided in three main parts. In the first part, basic concepts are given about bone anatomy and structure. They are followed by general notions on bone fractures, fracture risk and implant design. A short paragraph about functional adaptation explains how bone structure and mechanics are closely related and interact. The first part ends with a deeper explanation of bone shape and and bone mechanical properties. In the second part, the mechanical simulation tool, i.e. the finite element method, is described. First a brief history of its development in orthopaedics is presented. Then the three components necessary to the method are analysed: bone geometry, mechanical properties and boundary conditions. In the third part, statistical models are presented. After a more theoretical introduction, their use in bone mechanics is illustrated. The chapter ends with a short state of the art about works similar to the one presented, aims and structure of the thesis.

1.1 Bones

The human skeleton is the supportive and protective structure of the human body. It is composed by bones, characterised by rigidity and hardness. These features allow the skeleton to maintain the shape of the human body, to protect the organs of the cranial, thoracic and pelvic regions, and to propagate the force generated by muscles during the body movement. Moreover bones are a mineral storage for the human body, especially of calcium ions, and the producer of blood particles [55].

Bones can be described at different scale levels since their structure is hierarchical and complex. Each level has its own structural and mechanical characteristics, which are analysed with different measurement techniques [93]. As shown in Fig. 1.1, bones can be analysed at five different scales. At the macrostructural level, bones are subdivided in cortical and trabecular tissue. At the mi-

crostrucural level, the tissue components are considered, i.e. osteons and trabeculae. The objects of the sub-microstructure layer are the bone lamellae. At the nanostructural and sub-nanostructural level, the fibrillar collagen and the molecular composition are considered, respectively. In the following, the five levels will be briefly described.

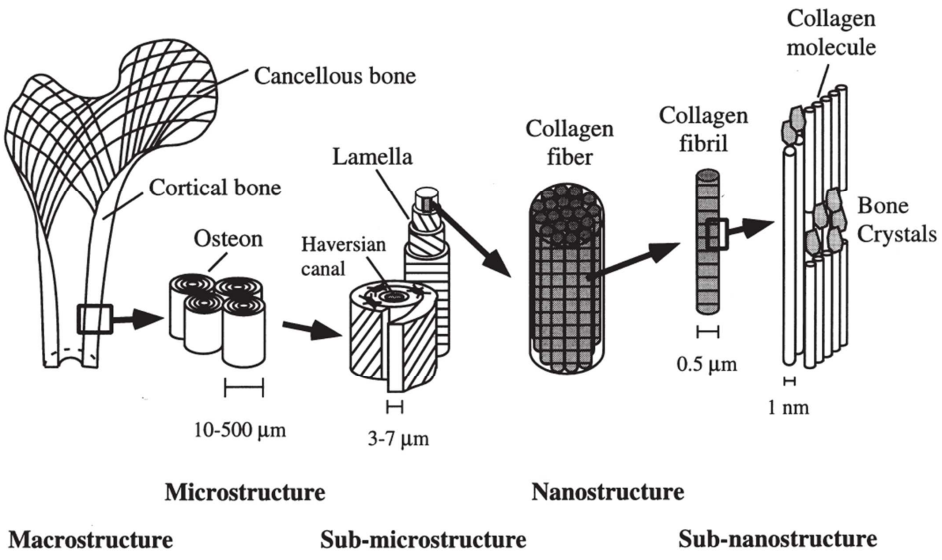

Figure 1.1: Bone hierarchical structure at different levels. Macrostructural: cortical and cancellous bone. Microstructural: trabeculae and Haversian system. Sub-microstructure: bone lamellae. Nanostructure: fibrillar with embedded mineral. Sub-nanostructure: constituent molecular structure, i.e. collagen molecules, minerals and proteins. (From [93].)

Bone macrostructure

Bone tissue can be divided in two main morphological categories: cortical (or compact) bone and trabecular (or cancellous or spongy) bone [76] (Fig. 1.2). *Cortical bone* is a very compact and dense tissue, its hard part covers 90% of its volume. It is the bone dominant tissue, since it constitutes 80% of the human skeleton. *Trabecular bone* appears as a system of rods and arches, called trabeculae. Conversely to cortical bone, in trabecular bone the soft tissue represents 75% of the volume [45]. Cortical and trabecular bone are combined in different ratios in the human bones. The different arrangement of these two bone tissues depends on the structural needs and their functions: cortical bone provides mainly mechanical and protective functions, whereas trabecular bone provides structural and metabolic functions [76].

Bone marrow is a third macroscopical component of bone, and differs from the two previous ones. Bone marrow can be differentiated in yellow and red marrow. Yellow marrow mainly fills in the cavity of long bones and is composed by fat, connective tissue rich of blood vessels and cells. Red marrow is found in short and flat bones and contains mainly water, cell-globulin and nucleo-proteid. It is the generator of the red blood cells, platelets and most white blood cells [42].

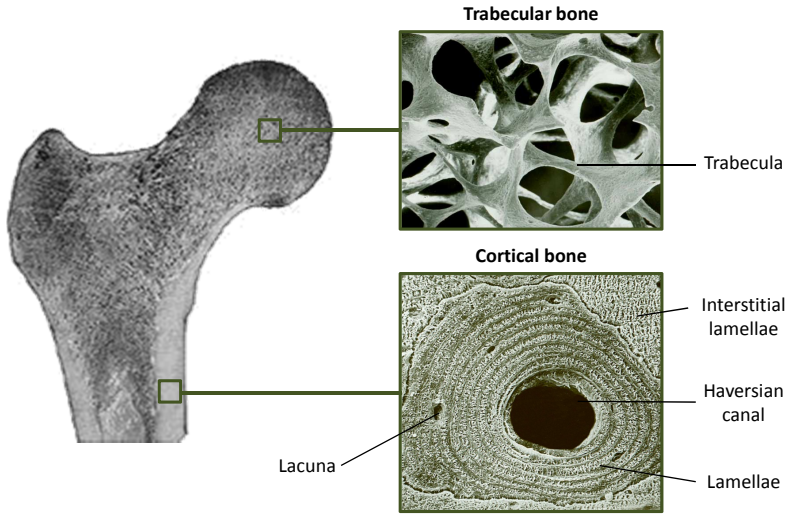

Figure 1.2: Bone macrostructure. Bone is composed by cortical and trabecular tissue. Cortical bone is mainly composed by cylindrical components defined osteons, whereas trabecular bones is mainly made by rods called trabeculae. (From http://www.gla.ac.uk/ibls/US/fab/tutorial/clinical/orhip.html and Marotti G., Summer school "Bone Cell and Tissue Mechanics", Udine, Italy, 2010.)

Bone microstructure

From a microstructural point of view, bones are divided in osteons (or Haversial systems), lamellar bone and woven bone [93]. Differences among these three categories concern mainly the disposition of bone lamellae, the bony sheets which constitute the main component of the bone sub-microstructural level. *Osteons* (or haversial systems) are composed by 4 to 20 rings of lamellae arranged concentrically around a longitudinal vascular channel. Each osteon is surrounded by a cement line, which is a mineralized matrix poor of collagen fibers and separates the osteon from the surrounding components. Osteons contain small holes called lacunae, where osteocytes live and communicate among each other through transverse channels called Volkmann's canals (Fig. 1.3). *Lamellar bone* is constituted by circumferential lamellae, which are found around the circumference of the shaft of long bones. They are either underneath the periosteum or on the internal surface adjacent to the endosteum. Finally, *woven bone* is made by less organized bone, where patterns are not well defined. Woven bone is found in growing bone and is replaced by structured bone during the maturation process [93, 45].

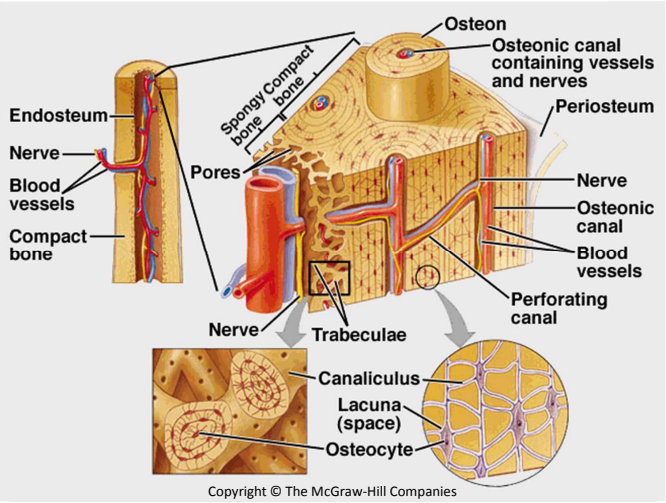

Figure 1.3: Bone structure. Components of cortical and trabecular bone. (From http://blog.dearbornschools.org/renkom/2011/02/09/microscopic-structure-of-bone/.)

At the microstructural level, an important component of bone is represented by bone cells. Bone contains five different types of cells: progenitor cells, osteoblasts, osteoclasts, osteocytes and bone lining cells. *Osteoprogenitor cells* are the generators of osteoblasts [55]. *Osteoblasts* are the cells responsible for the bone matrix production and for the regularization of the mineralization of bone matrix, however the mechanism is not completely understood. *Osteoclasts* are the large multinucleated cells that reabsorb bone. *Osteocytes* are mature osteoblasts that live in the osteons' lacunae and are responsible for the bone maintenance. They communicate through canaliculi in the matrix by means of gap junctions. Finally, *bone lining cells* are flat and elongated cells that cover bone surface. They are inactive cells and it has been hypothesized that they could be precursors for osteoblasts [76].

Other bone levels

Bone sub-microstructure is represented by *lamellae*. Each lamella is 3-7 microns in thickness and contains parallel collagen fibers [93]. Lamellae are mainly made of fibers of collagen that are parallel in each lamella. In osteons, which are a structured unit, lamella fibers change orientation from one lamella to the other, alternating a longitudinal lamella, where collagen fibers are situated along the main axis of the lamellar sheet, with a trasverse one, where collagen fibers are perpendicular to the main axis [93].

Bone nanostructure is constituted of *collagen fibers* surrounded by mineral [93]. Collagen is a protein synthesized and secreted by osteoblasts, and it performs a structural role in the extracellular matrix [55]. Bones are mainly constituted of collagen I. In bones, collagen I has different charac-

teristics than in other body tissues. It calcifies more, most likely because of phosphoproteins, it is less soluble, more densely packed and less hydrated [45].

Bone sub-nanostructure is made of minerals and organic matrix components. *Minerals* constitute 75% of bone weight. The main mineral contained in the extracellular matrix is the hydroxyapatite ($Ca_{10}(PO_4)_6(OH)_2$), which is mainly made of calcium and phosphorus. Hydroxyapatite is embedded in the collagen frame and its interaction with collagen is the cause of the rigidity and hardness of the bone. Other minerals present in the matrix are carbonate, citrate sodium and magnesium. The *organic matrix* is composed of about 90% of collagen and 10% proteins and glycoproteins and a small amount of proteoglycans, lipids and peptides [45].

1.1.1 Bone fracture

Fractures occur when a bone can not withstand applied forces. Bone fractures can be caused by trauma or by disease, like osteoporosis [122]. According to the AO classification, bone fractures are categorized depending on the location in the body, their morphological complexity, the difficulties of their treatment and their prognosis (Fig.1.4a) [23]. Bone is genetically programmed to heal after fracture and no treatment is needed [22]. The healing process is constituted by three main phases: the inflammatory phase, where hematoma and granulation tissue are generated, the reparative phase where a cartilagineous callus is created and then transformed to a bony callus, and the remodelling phase, where the woven bone of the bony callus is replaced by lamellar bone through a remodeling process (Fig.1.4b) [23]. However this healing process can be faster and more efficient with a surgical intervention. The surgical intervention is performed for two reasons: to restore the bone anatomy, and to produce bone stability. Bone stability is needed to allow the patient to load the bone as soon as possible [22]. From the principals of functional adaptations, in fact, bone production occurs when bone is subjected to dynamic strains, as explained in below.

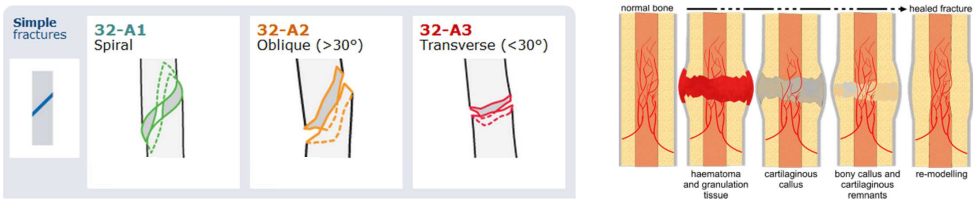

(a) (b)

Figure 1.4: Bone fracture. (a) Simple femur shaft fractures. (b) Bone healing process. (Modified from http://www.aofoundation.org/Pages/home.aspx and http://pathwiki.pbworks.com/w/page/14673867/Bone23-27.)

Fracture risk assessment

Among the elderly, fractures often occur from events that involve little energy of impact, like falls from standing or lifting activities. These bone fractures are often associated with age-related reductions in bone strength and mainly involve hip, spine and wrist [122].

The probability of incurring in this kind of fractures is assessed in terms of fracture risk. In clinical practice fracture risk is usually measured through imaging techniques, like dual-energy X-ray absorptiometry (DXA) and quantitative computer tomography (QCT). These techniques detect bone mineral density (BMD), that is strictly related to bone strength (for more details see Section 1.1.4). DXA is a standardized X-ray technique which eliminates the effect of soft tissues by measuring the attenuation of X-rays at two different energy levels. In DXA images, the bone mineral content is normalized with respect to a predefined rectangular area (aBMD) as shown in Fig. 1.5a, and compared with standard tables in order to classify the risk of fracture of the patient. DXA is the most spread technique in clinical practice, due to the low amounts of radiations to the patients and low associated economical costs. However, in DXA images the discrimination between cortical and trabecular bone is not possible, and only an areal measurement of bone density is provided [59]. QCT consist in acquiring CT scan of the anatomical site of interest with a calibration phantom. The phantom is composed of different materials whose density is known and can be related to bone-equivalent values. QCT allows volumetric BMD to be determined (Fig. 1.5b), distinguishing between cortical and trabecular bone [59]. This implies higher precision in the calculation of the BMD and therefore of fracture risk. However, radiation exposure and costs are high and a standardization is still missing [84].

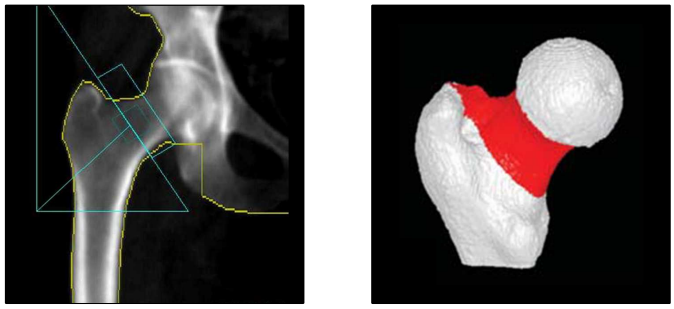

(a) (b)

Figure 1.5: Fracture risk evaluation from medical images. (a) Areal region of interest in DXA. (b) Volumetric region of interest in QCT. (From http://healthwise-everythinghealth.blogspot.com/2010/08/osteoporosis-testing-with-dxa.html and [84].)

Beyond the clinical evaluation, fracture risk can be assessed from mechanical calculations. In this case the current bone situation is compared with a limit situation obtained from experimental results. The limit situation considered is often the yield point, that represents the point at which

the bone starts to deform in an irreversible way. The measurements that are taken into account are strains [101], stresses [71] or strengths [65]. Calculations are performed using finite element methods (see Section 1.2 and Chapter 3). The main limitations of these calculations is that little is known about magnitude and direction of the load applied to the bones in case of fracture. However, it has been proofed that they add useful information to the fracture risk clinical evaluation, both in case of DXA [114] and QCT [70].

Plate fixation and design

When a fracture occurs, it can be healed through indirect or direct reduction techniques. In indirect techniques, the fracture is not directly exposed during the healing and the fracture area remains covered by the surrounding soft tissue. An example of indirect techniques are external fixators. In direct techniques the fracture area is exposed. Examples of direct techniques are screws, plates and implants [23]. Since in Chapter 4 plate design is considered, a few details will be given about plates.

Plates provide rigid fixation to fractured bones. Since their introduction in the 1960s, plates have had a firm place in fracture treatment. Three main generations of plates have been used. In 1969 dynamic compression plates (DCP) were introduced. They had a hole design which allowed them axial compression of the two bone fragments by eccentric screw insertion. During the surgery, screws were first inserted in one bone fragment. Then the two fragments were compressed one to the other in order to allow faster bone healing. Finally screws were inserted in the other fragment to stabilize the bone. DCP were designed for different functions (compression, neutralization, tension band and as buttress) and in different sizes according to the dimension of bones in different anatomical sites. One of the disadvantages of these plates was the formation of necrotic tissue in the bone-plate contact area. Some years later, the limited contact dynamic compression plates (LC-DCP) were introduced. They limited the contact between the bone and the plate, creating less damage to the capillary network of the periosteum [23]. In 2000 the AO technical commission approved the locking compression plate (LCP) as the new plate standard (Fig. 1.6a). This plate combined the advantages of the previous plates with the locking screw head principle. Screw holes, in fact, were specially designed to accept both standard screws with hemispherical heads, and locking screws with threaded heads (details in Fig. 1.6a). The fixation procedure was the same as for the previous plates, but screws could be inserted in any direction, guaranteeing a better fracture stability [22]. One of the main disadvantages of plates concerns their shape. Bone plates are produced with standardized shape. In order to make them patient-specific, they need to be contoured. If the plate does not fit the anatomy of the patient's bone, the fracture reduction will not succeed. In order to accomplish plate contouring, a hand-held bending plier is first used as template to detect the bone shape (Fig. 1.6b). Then, according to the shape detected with the template, the plate to be fixed in the patient is bent using the bending press (Fig. 1.6c). The disadvantages are that this process is time consuming and repeated bending of the plate must be avoided since it weakens the plate itself [23].

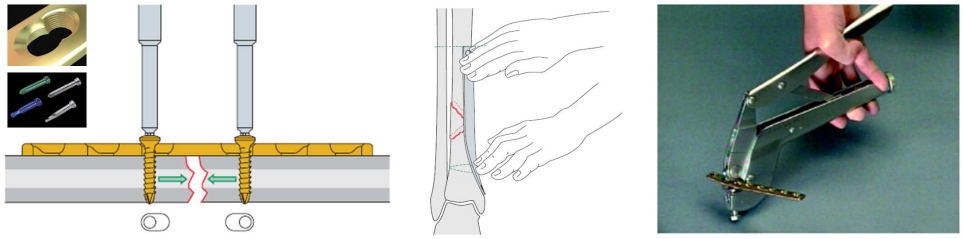

(a) (b) (c)

Figure 1.6: Bone plates. (a) Plate axial compression for bone reduction. Shape of the LCP hole and screws in detail. (b) Hand-held bending pliers. (c) Bending press for plate contouring. (Modified from [23, 22].)

1.1.2 Bone functional adaptation

From a metabolic point of view, bone is a very active tissue. The effect of this activity is to keep the bone optimally designed for its functional requirements. The discovery of this activity has a fascinating history and is still in development. The pioneers of bone functional adaptations were Culmann, a structural engineer, and von Meyer, an anatomist, in 1867. They pointed out the similarity between the principal stress trajectories in a crane-like curved bar, which Culmann was designing, with a sketch of the femur head structure drawn by von Meyer (Fig. 1.7). A few years later, in 1892, Wolff published a book [124] from which the so called Wolff's law was deduced: Skeletal elements are strategically aligned to the prevailing direction of loading, and their mass is optimized for bearing the magnitude of the prevailing load. Some decades later, in the 1960s, starting from Wolff's deductions, Frost elaborated a model called 'mechanostat': biological mechanisms fit skeletal mass and architecture to the needs of ones physical activities with processes of bone modeling and remodeling. According to this principle, which is commonly summarised as 'use it or loose it', in case of reduced load bones start a process of bone resorption, like it happens to astronauts after a space flight, whereas in case of higher load there occurs bone production, as it happens for the upper limb bones of tennis players [27, 40]. Bone resorption and production occur during bone modeling and remodeling. Bone *modeling* involves bone resorption and formation in different bone sites at the same time. It allows not only the development of bone architecture during bone growth, but also the adaptation of bone architecture and mass when mechanical conditions change. Bone *remodelling* occurs at the same site at different times and involves the resorption of immature or old bone followed by formation of new lamellar bone. It allows the removal of microdamages, the replacements of dead bone and the adaptation of bone microarchitecture to local stresses [55]. In the 1980s, Rubin experimentally showed how bone formation and resorption are strictly linked to the kind of stimulus given to the bone. In a famous experiment on a turkey ulna he showed how, in order to have functional adaptation, the mechanical stimulus must be not only dynamic but also with an optimal strain rate [94]. As shown in Fig. 1.8, in physiological situations there is a strong relationship between the microstrains and the number

of loading cycles for bone formation, equilibrium and resorption.

Bone functional adaptation is still a very open topic and a very interesting challenge in bone behavior knowledge.

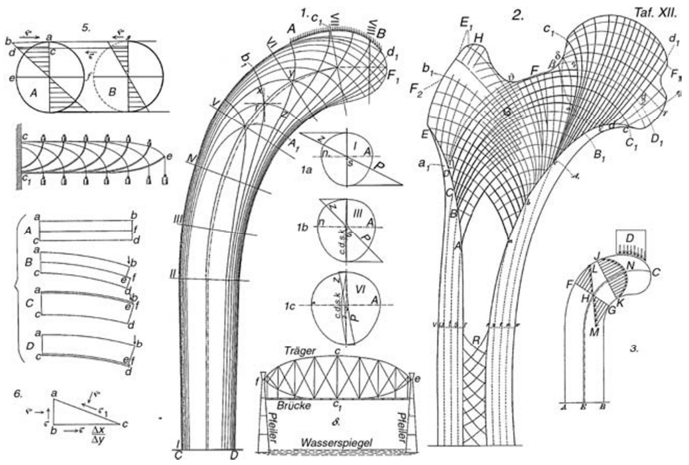

Figure 1.7: Figure created by Culmann and von Meyer in 1867 which shows the parallel between the crene inner structure that Culmann was warking on (left) and the bone inner structure studied by Mayer (right). (From von Meyer, G.H., Arch. Anat. Physiol. Wiss. Med. Reichert DuBois-Reymonds Arch., 34, 615628, 1867.)

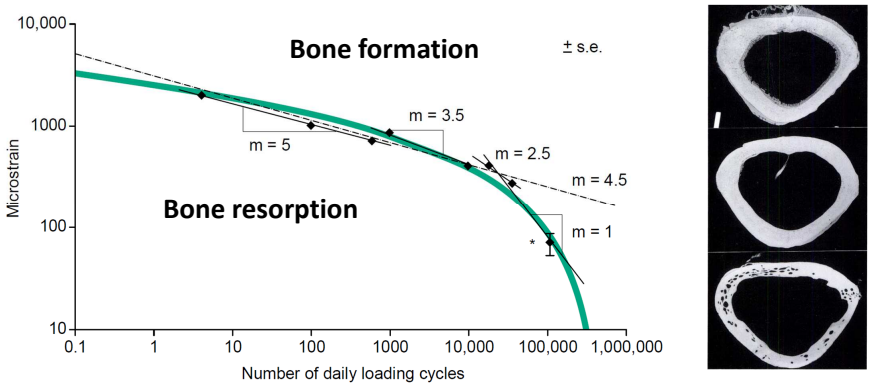

Figure 1.8: Mechanical stimuli for bone functional adaptation. Different relationships between strains and numbers of cycle cause bone formation, equilibrium and resorption (left). Shaft section of Rubin's turkey ulna showing bone formation, equilibrium and resorption (right, from top to bottom). (Modified from [95] and [78].)

1.1.3 Bone shapes

The human body is composed of about 200 bones, which are part of spine, cranium, face, hyoid bone with sternum and ribs, upper extremities and lower extremities [42]. Bones can be grouped in four different categories depending on their shapes [42]: long, short, flat and irregular bones (Fig. 1.9) [42, 110]. Following evolutionist theories, these shape-based group are strictly related to bone functions [30]. *Long bones* are designed by nature to constitute a system of levers to sustain the weight of the trunk and to transmit power for the body locomotion. Long bones are found mainly in the upper and lower limbs. *Short bones* are placed in those parts of the skeleton that are strong and compact and where the movement is limited. These bones are mainly made of trabecular tissue and are surrounded by a thin layer of cortical bone. Example of short bones are the carpal and the tarsal bones. *Flat bones* are found where the skeleton needs protection or broad structures for the attachment of the muscles. Flat bones consist of two layers of cortical bone separated by a layer of trabecular bone. Flat bones are placed in the skull and the shoulders. Finally, *irregular bones* are those bone which, given their particular shape, can not be grouped in any of the previous categories. They are made of a core of trabecular bone surrounded by cortical bone of variable thickness. Example of irregular bones are the vertebrae [42, 110]. Since the thesis project focused on lower limbs long bones, in particular femur and tibia, a more detailed description will be given about this bone group shape.

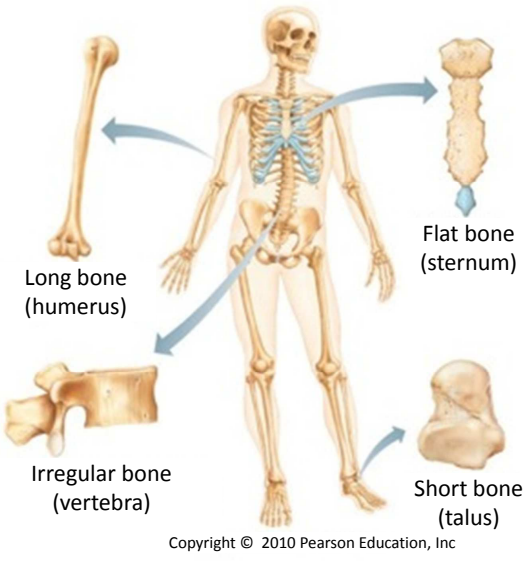

Figure 1.9: Bone shapes. Bones can be divided in long, short, flat and irregular based on their shape. (From: http://massasoit-bio.net/courses/201/201_ content/topicdir/skeletal/skeletal_ RG/skeletal_ RG2/skeletal_ RG2.html.)

Long bones are externally surrounded by the *periosteum*, a membranous tissue through which vessels can reach the inner parts of the bone. The interior cavity of the bone is instead covered by a vascularized cell layer, called *endosteum*, which separates the marrow from the bone cylindrical cavity [42]. Long bones are composed by three parts: epiphysis at the extremities, diaphysis in the middle, and metaphysis as joint between the other two parts. (Fig. 1.10). The *epiphysis* constitute the bone extremities. They are mainly made of trabecular bone surrounded by a thin layer of cortical bone. The cortical bone is then surrounded by a small outer layer of sinovial cartilage. The epiphyis are the parts of long bones involved in joint articulation, and this determines their swollen shape. The sinovial cartilage is not a strong tissue, due to its low tensile and compressive strengths, therefore when loads are transferred from one bone to the other, they must be spread over a large area of cartilage in order not to damage it. Moreover large joints have large angles of movement since the need of low stresses for the sinovial cartilage implies the presence of large radii of curvature [30]. In young human beings, the epiphysis ends towards the bone shaft, with the growth plate line [110]. This is the site where the bone production occurs during the body growing phase. The growth plate is made of a layer of cartilage cells and matrix, blood vessels and newly formed bone. In adults the growth plate disappears and it is substituted by a small line of compact bone. The growth plate is connected to the bone diaphysis through the metaphysis. The *metaphysis* is mainly made of trabecular bone, surrounded by cortical bone in the outer part of the bone. The

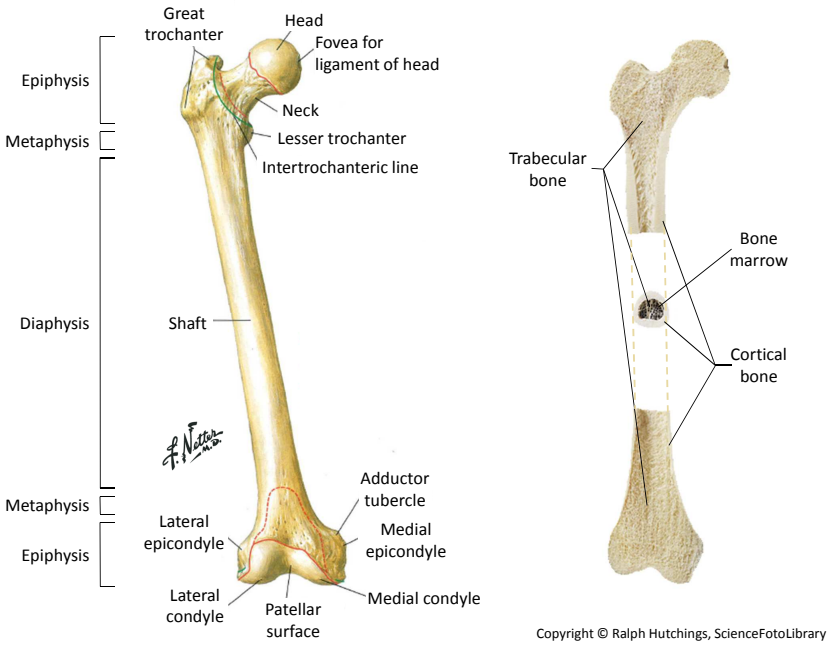

Figure 1.10: Long bone anatomy. Long bones are constituted by three main parts: epiphysis, metaphysis and diaphysis (left). Their outer layer is made by cortical bone, whereas their inside is composed by trabecular bone and marrow (right). (Modified from: [82] and http://www.sciencephoto.com/media/119084/enlarge.)

diaphysis is the bone shaft; it is a compact hollow cylinder that contains the bone marrow. From an evolutionist point of view, the shaft of long bones has shape and size determined by the optimization need of bearing the imposed load with the minimum bone mass [30]. The shape of the section of long bone diaphysis depends on the load distribution with respect to the bone neutral axis. If the loads are distributed in a homogeneous way, the section of the shaft has a circular perimeter, e.g. in case of femur. If loads are distributed in a more articulated way, the shaft has a different shape perimeter, like the triangular one for tibia. The size of the cortical ring of the bone diaphysis is mainly regulated by the local buckling phenomenon. The local buckling occurs when the bone walls are so thin relatively to the size of the complete structure that the structure itself is not able to support the wall from an excessive bending [30, 110].

1.1.4 Bone mechanics

Bone is considered an inhomogeneous material, since it is composed of different constituents, i. e. cells and organic and inorganic substances, which have different mechanical properties. Moreover, these bone components constitute the bone in different percentages, depending on age, gender, type of bone and type of bone tissue. Furthermore the bone structural arrangement is different depending on the hierarchical level being examined (Fig. 1.1). Therefore the bone mechanical characterization implies different techniques at different levels [93, 45]. Details will be given about the mechanical properties of bone considering first bone as a whole, and then analyzing separately its two tissues, i.e. cortical and trabecular bone.

Bone is a slightly *viscoelastic* material. Its stiffness and strength are in fact rate dependent, although experimental results suggest that the effect of the viscous component is small [30]. Bone viscoelasticity depends on bone conditions. When the bone is dried, its viscous behavior disappears and the bone can be compared to a perfect spring. On the other hand, when the bone is wet it behaves like a spring with a small shock absorber due to its strain rate dependence [115]. Bone is also an *anisotropic* material since its mechanical properties depend on the direction of the applied load. In particular, bones are stronger when bearing compressive loads than when bearing tensile forces [45]. This can be seen as a result of natural evolution, which gave bones functions of skeleton support and locomotion [30].

The mechanical interpretation of bone tissues is still controversial. From a mechanical point of view, it is still not clear if cortical and trabecular bone are two different tissue with peculiar characteristics or if the cortical bone can be considered as a very dense trabecular bone [45]. However, traditionally bone mechanical properties are separately treated for the two types of bone tissues, therefore the distinction will be kept also in this introduction. The mechanical properties of bone have been measured in different experimental studies, mainly in vitro, using either human cadaver specimens or animal specimens. There is a large variability between the results obtained. Studies differ for testing methods (mechanical testing, nano indentation, ultrasound), specimen geometry (size and shape), specimen anatomical origin (femur, tibia, vertebra), specimen support during testing (end caps, platens, confined or unconfined compression), strain rate, patient characteristics, etc. [45]. In general, we can represent bone tissue mechanical behavior as stress-strain curves

(Fig. 1.11). These curves have similar behavior for both cortical and trabecular bone, both in tension and compression. The initial linear behaviour represent the elastic deformation of bone at the beginning of tests. The slope of this curve is defined as Young's modulus and represents the bone stiffness. The elastic behavior ends at the yield point, where the plastic response starts. From this point, inner structures of bone change in an irreversible way. Unloading the specimen will not allow the bone to recover its original characteristics, since part of the deformation is maintained in the specimen. Finally the curves finish at the fracture point where stresses and strains are so high that bone specimen breaks. Beyond these common characteristics, a few distinctions can be made between the two bone tissues, as shown in Table 1.1 and Fig 1.11.

Table 1.1: Cortical and trabecular bone mechanical characteristics.

Bone tissue	Young's modulus	Yield strain	Ultimate strain
Cortical bone	12-20GPa [46, 45]	0.6-1.2% [3, 45]	2.5% [45]
Trabecular bone	70-673MPa [46, 45]	0.6-1.2% [61, 67, 45]	1.59-7.6% [61, 45]

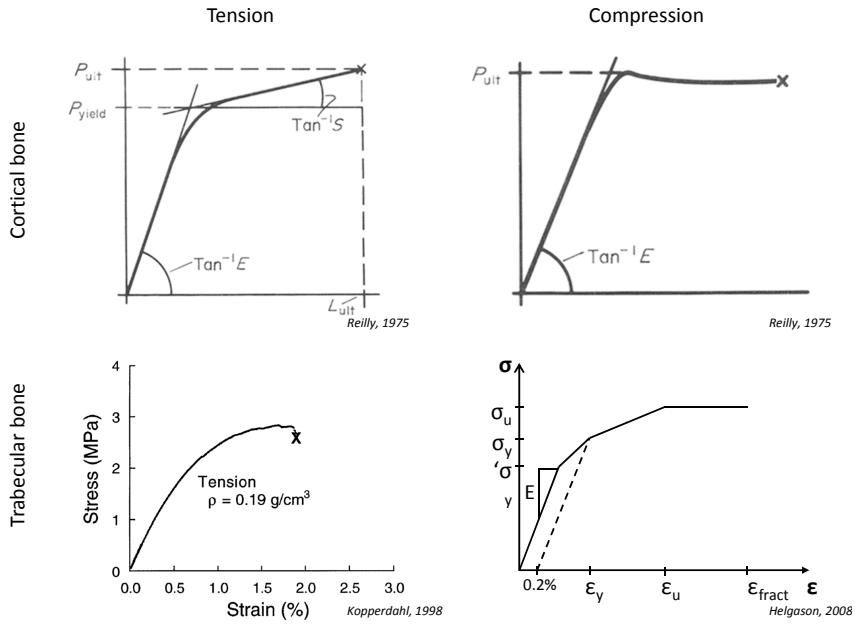

Figure 1.11: Stress-strain curves for trabecular and cortical bone in tension and compression. (Modified from [92, 67, 45].)

Starting from the 1970s, efforts were made to study the relationship between bone mechanical properties and *bone density*. In 1977 Carter and Hayes conducted experiments to study bone mechanical properties, considering the bone as a composite material, made of a solid phase, i.e. mineralized bone tissue, and a fluid phase, i.e. blood vessels, blood, marrow, nerve, cells, interstitial fluid. They found that bone Young's modulus and bone density are related by a power law that contains experimentally derived constants, as it was hypothesised in previous studies [19]. Since then, a large amount of experiments have been performed in order to mathematically correlate bone mechanical properties to bone density. However these experiments were performed varying many parameters, like the bone tissue type (cortical or trabecular), the size and the anatomical origin of the specimen, the conditions both of bone and testing machine, etc. This caused difficulties at directly comparing different experiments and at extrapolating a common knowledge of the relationship of bone material properties with bone density. Many of these methods were collected and analized in 2008 by Helgason et al. [46]. In this review paper, it was shown that even after normalization of the results, a high inter-study variability persists and it is not clear if this can be explained only by the use of different measurements protocols. The topic is therefore still quite open. In Fig. 1.12 some of these laws for femur and tibia are reported. As state of the art, Morgan's material law is considered the most reliable [80]:

$$E = 6.850\rho_{app}^{1.49} \tag{1.1}$$

where E is the Young's modulus in [GPa], and ρ_{app} is the apparent density in [g/cm^3], that is the hydrated tissue mass over the total specimen volume.

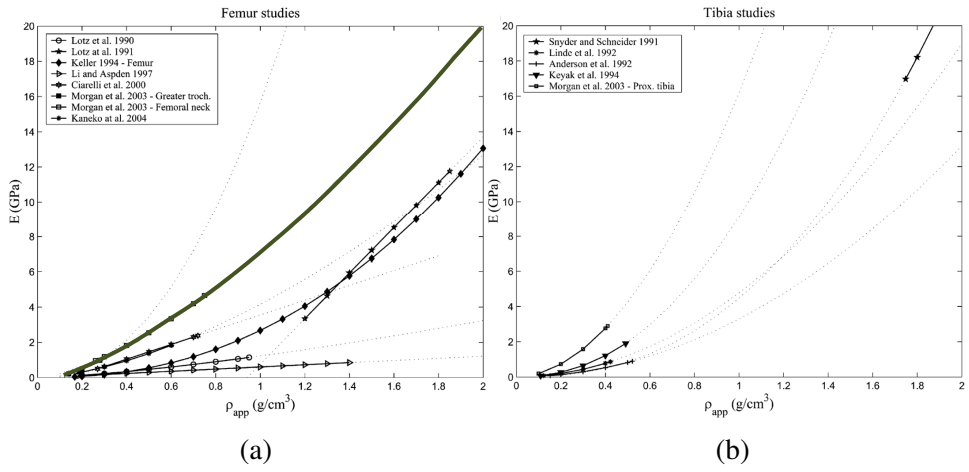

(a) (b)

Figure 1.12: Groups of relationships between material properties and density for femur (a) and tibia (b) available in literature. The green line in the femur graph represents Morgan's law [80]. (Modified from [46].)

Beyond experimental testing, bone mechanics is studied with mathematical models. As all mathematical models, bone models must be able to describe reality using appropriate and essential parameters. Moreover it must be possible to verify the correctness of the model through the available experimental data. When using models, the main advantages are that parameters can be varied in an easier and controlled way, the information obtained is extensive and the results can be generalized [13]. The main tool used to study bones in silico is finite element methods.

1.2 Finite element method in orthopaedics

The finite element method (FEM) is a powerful tool for the numerical solution of engineering problems. In this method, a continuum is defined by a complex region, which is discretized into geometric units called finite elements. For each element, material properties and governing relationships are considered and expressed as unknown at the integration points. An assembly process, which takes into account the boundary conditions, results in a set of equations whose solution give the approximate behavior of the considered continuum. The finite element method originated in the 1940s and started to be used in 1960s. After the introduction of the personal computer, it has been extensively used for mechanical simulations in many engineering subjects [20].

The finite element method was introduced in orthopaedics about 40 years ago, in 1972, by Brekelmans to analyse stresses in a human femur under physiological loads [13]. At the beginning of 1980s, FEM were already used in different applications, like stress analysis of bones, fracture fixation, and artificial joint design and fixation. At the same time, the first studies on articular cartilage and intervertebral discs appeared. At the beginning of the 1990s, FEM applications had extended from the structural failure assessment of the previous decade to the study of constitutive tissue behaviour, biological processes and microstructural modeling [53]. Finally from the end of 1990s technological development affected positively the use of FEM in orthopaedics. For example, advancements were made in model geometries thanks to the extraction of structures from CT images [88]. During these years, many issues had to be taken into account. FEM is a tool which needs a proper problem formulation [52], correct simplifications when modeling the complexity of human tissues [53], and accurate validation with experimental data [88].

In order to compute valid simulations using FEM, three main issues must be taken into account: geometry, which describes the object shape, material properties, which define the object mechanical behavior, and boundary conditions, which describe the loading and the constraints applied to the object.

Geometry

In the finite element model, object's geometry is represented as a mesh, i.e. a grid of elements which discretize the object itself. The first mesh by Brekelmans [13] in 1972 was a surface mesh made of triangles (Fig. 2.5a). Later in the 1970s volumetric meshes also appeared (Fig. 2.5b). In 1990, Keyak et al. [63] proposed an automatic method for creating meshes directly from CT images, converting the image voxels into FEM elements (voxel-based meshes) (Fig. 2.5c). In the

following years, thanks to the development of commercial and non commercial FEM software, different shaped elements became available and standardized mesh procedures were developed. In 1998, Viceconti et al. [120] compared different methods for automatic meshing of the human femur. They compared mapped meshes, which are created decomposing the femur in sub-volumes separately meshed, tetrahedron meshes, made of quadratic elements, hexahedral meshes, made of 8-node elements, and voxel-based meshes, where the elements are directly derived by CT voxels. Results showed that the hexahedral mesh was the most precise at predicting experimental displacement, followed by mapped, tetrahedron and voxel-based meshes. Commonly the most used meshes are quadratic tetrahedron meshes. In order to have reliable simulation, it was shown for femurs that they should be composed at least of about 125000 quadratic elements [47].

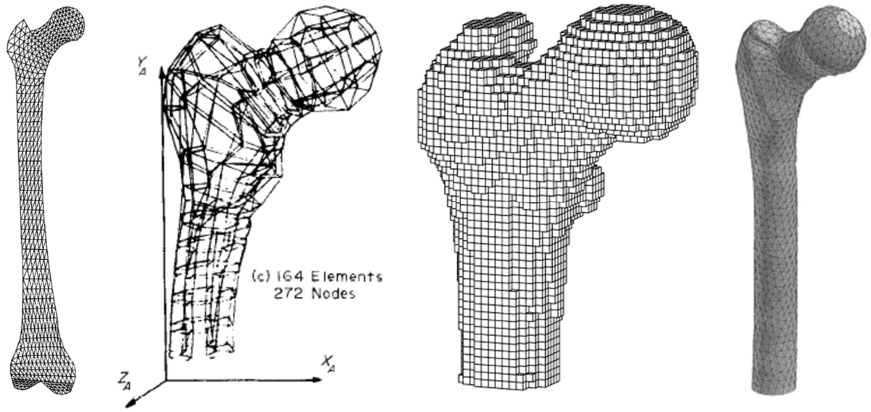

Figure 1.13: Four different generations of bone meshes. (a) 1972: Surface triangular mesh . (b) 1977: Eight-node volumetric mesh. (c) 1990: Voxel-based mesh. (d) 1990s: Tetrahedron mesh. (From [13, 117, 65, 120].)

Material properties

Since the very first simulations in the 1970s, bones were considered homogeneous, isotropic and linear elastic materials. A constant Young's modulus was assigned to either the whole bone [13] or its cortical and trabecular components [117]. Also in some recent studies constant mechanical properties are assigned to bone tissues [108]. In 1985, McBroom et al. found strong correlations between the intensities of computer tomography (CT) images and the apparent density (ρ_{app}) of trabecular bone of vertebrae [77]. CT image grey levels represent the attenuation of X-rays when they pass through materials. The apparent density of the bone is the density of a bone specimen, as described above. This finding opened the possibility of determining bone density directly from CT images, calculating mechanical properties from bone density and using the obtained values for FEM simulations. In 2008, Schileo et al. pointed out the importance of an accurate estima-

tion of bone densities for reliable FEM mechanical properties assignement [99]. They related CT image intensities with Young's modulus measuring three different bone densities: ρ_{QCT}, which is the mineral content of the bone represented by the grey levels of the CT image, ρ_{ash} which is the mineral content of the bone specimen and is calculated as bone ash mass over the specimen volume, and ρ_{app}, defined above (Fig. 1.14). After calibrating the CT image with a proper phantom, they linearly related ρ_{QCT} with the CT grey level intensities, and ρ_{ash} with ρ_{QCT}. Then, from the measurement of the mineral part of the bone, he took into account the bone as a whole, converting ρ_{ash} to ρ_{app} and finally calculated the Young's modulus with the Morgan's law (Eq. 1.1). A very similar procedure has been used in the experiments of Chapter 3, with a small modification at the beginning of the pipeline. The images of our dataset were acquired without a phantom, therefore image calibration was not possible.

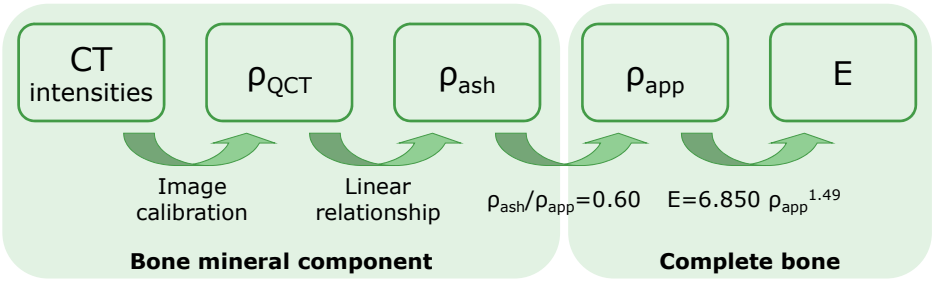

Figure 1.14: Bone mechanical property assignment from CT images as suggested by [99]. CT intesities, ρ_{QCT} and ρ_{Ash} are measure of the mineral part of the bone, whereas ρ_{App} and E of the complete bone.

The use of the proper material law is fundamental for the correctness of the simulations. As shown in Section 1.1.4, several different laws are available from experimental studies. In 2007, Schileo et al. proved that the Morgan's law (Eq. 1.1) is the one that better describes the relationship between ρ_{app} and Young's modulus [101]. Strains measured on bone specimens and strains calculated with FE simulations resulted to be highly correlated when the Morgan's law was used (Fig. 1.15). For this reason, Morgan's law was used in the simulations of this work (see Chapter 3 and Chapter 4).

To perform FE simulations, the calculated mechanical properties must be associated to meshes. In 1990 Keyak et al., while introducing their voxel-based mesh, presented a new way of assigning mechanical properties to the mesh elements [63]. From calibrated CT numbers they computed the bone apparent density and used it to estimate the Young's modulus using the equation found by Carter et al. [19]. In 1998 the method was extended to tetrahedron meshes by Zannoni et al. [127]. They assigned the average of the CT intensities extracted at the element nodes to the mesh elements. The method was subsequently refined in 2004 by Taddei et al. who integrated the CT intensities over the element volume [111]. In 2008 Helgason et al. proved that more accurate FE results are obtained if the mechanical properties are assigned directly to nodes (and not to

elements) and the partial volume effect is taken into account [47].

The assignment of mechanical properties to mesh elements or nodes still has some limitations. Trabecular bone is generally treated as a continuum, despite being a discontinuous material [88]. Bone is often considered linear elastic, and not slightly viscoelastic. Finally, bone is considered isotropic, despite being anisotropic. In this last case, corrections are done using either a tension or a compression law when relating density and Young's modulus.

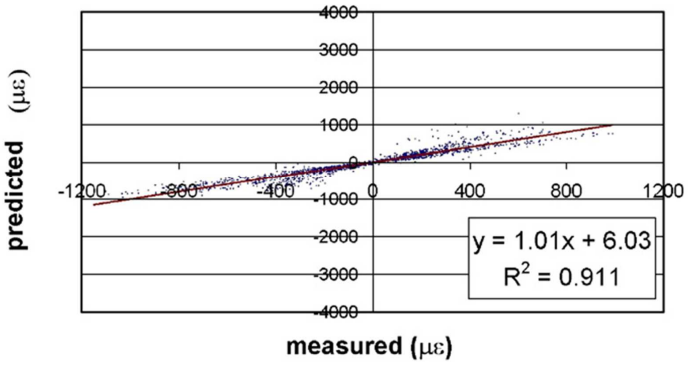

Figure 1.15: High correlation between the strains measured experimentally and the strain calculated with FEM when the Morgan's law is used. (From [101]).

Boundary conditions

Boundary conditions define loads and constraints applied to the geometry of interest. In case of bones, boundary conditions are determined by the interaction of bones with muscles and ligaments. The experimental measurement of boundary conditions in vivo is not trivial. Generally, they are studied during gait analysis tests [14]. In these tests, subjects are asked to walk or climb following predefined protocols (Fig. 1.16a). Infra-red markers are applied to the subject lower limbs in order to record their position during the movement. As an example, the walking gait cycle of an healthy subject consists of a stance phase, when the leg is in contact with the ground, and a swing phase, when the leg is not in contact with the ground. During the cycle, force magnitudes and directions can be measured both directly and indirectly. Direct measurement imply the use of either strain gauges applied on bone surface or incorporated in instrumented implants. Instrumented implants are clinical implants modified to measure strains (Fig. 1.16b) [6]. These measurements can be either invasive, if the strain gauges are connected to the acquisition instrumentation through wires, or non invasive, when the connection is telemetric [37]. However, these instruments detect very local surface changes and they are strictly linked to the presence of an implant, implying on one side the need of an invasive intervention on the human body, and on the other the measurement in an situation which has been altered due to the surgery and the presence of the implant. Indirect measurements are performed to quantify muscle forces, that can not be measured directly. Data collected from gait analysis and instrumented implants are analyses in inverse kinematics prob-

lems. The action of muscles and acting forces is simplified (Fig. 1.16c), and the points of the system are considered in equilibrium. The system is solved through optimization [14].

Despite the developments that have been made for geometry description and material properties assignment, still many challenges remain in the quantification of the boundary conditions.

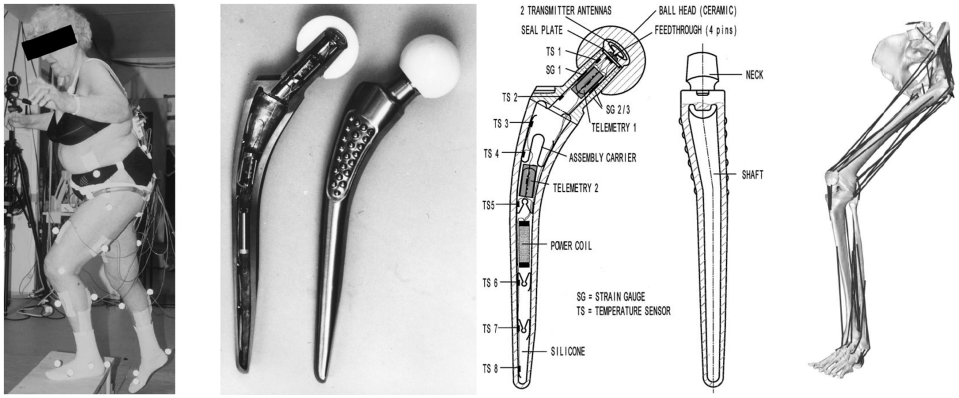

(a) (b) (c)

Figure 1.16: Bone boundary condition measurements and representation. (a) In gait analysis test markers are applied to the subject in order to study the muscle load on bones in the lower limbs. (b) Instrumented hip implants. The implant is modified from a clinical implant (left) adding strain gauges and telemetric receptors (right). (c) Representation of the action of muscles on lower limbs bones. (Modified from [48, 6].)

1.2.1 Patient-specific vs. population-based models

Nowadays the use of finite element models in orthopaedics is mainly patient-specific. Authors usually perform studies only on a few cases of interests [65, 108, 47, 99]. In this setting, one of the main issue is the generalisation of the findings from some particular cases to a more extended group of subjects. Different individuals of a population can vary in terms of age, gender, ethnicity, etc., and these differences can have effects on the bone mechanical behaviour. The extension to population studies could therefore overcome this issue and allow a broader generalisation of the findings. The first requirement for this kind of approach would be to collect a high amount of data, which in many countries is regulated by strict rules. The second one would be developing automatic tools to analize and process the big amount of data, both in terms of creation of the geometry, assignment of mechanical properties and boundary conditions, and post-processing of the findings. Whereas the second requirements can be easily implemented thanks to the technical development, the first requirement is still difficult to realize. Therefore an alternative can be used to create a plausible population starting from a smaller dataset. The population will have the basic characteristics of the original data, but the variations between subjects can be analized, rationalized and controlled using mathematical tools. One of the techniques which allow creating a plausible

population from a training dataset are the statistical models of shape, intensity and appearance.

1.3 Statistical models in orthopaedics

1.3.1 Statistical models of shape, intensity and appearance

Statistical models are a tool to estimate population variability starting from a training dataset. The patterns of the variability of the data are parametrized through statistical analysis and are used to provide a compact and efficient representation of the data [31].

Statistical models were introduced in 1995 by Cootes and Taylor with the aim of creating a model able to capture the variability of shapes in a dataset [25]. The implementation core of the method consists in finding correct correspondences among the subject of the dataset, and calculating principal component analysis (PCA) on them. The calculation of correct correspondences is considered the main issue in statistical models because on one side the task is technically not trivial, and on the other side wrong correspondences would lead to a wrong model [31]. There are different techniques to detect point-to-point correspondences, based on either manual procedures, like manual annotation of homologous landmarks, or automatic approaches, based on parametrisation, distances, features, physical properties and image characteristics [31]. After point-to-point correspondences are established, PCA is calculated. PCA is a multivariate statistical technique which aims at reducing the dimensionality of a dataset retaining as much as possible of the variation present in the dataset. This is achieved by transforming data to a new set of variables, which are uncorrelated and ordered from the most to the less important in terms of variation [57]. More technically, PCA can be defined as the eigenvector decomposition of the data covariance matrix.

The first statistical model introduced was the *statistical shape model* [25]. Correspondences within a set of shapes were manually annotated and PCA was computed. Any shape of the training dataset could then be approximated by the mean shape and a weighted sum of the deviations obtained by the modes:

$$x \approx \bar{x} + \sum_i \Phi_{s_i} b_{s_i} \tag{1.2}$$

where x is the shape of the dataset, $\bar{x}$ is the average shape, Φ_{s_i} are the model modes (or eigenvectors), b_{s_i} are the model parameters, and i is the number of the retained modes and parameters.

Following the statistical shape model, the *statistical intensity model* was proposed [26]. The same procedure was considered, but performed on image intensities. The model was described as follows:

$$g \approx \bar{g} + \sum_i \Phi_{g_i} b_{g_i} \tag{1.3}$$

where g is an intensity distribution of the dataset, $\bar{g}$ is the average intensity, Φ_{g_i} are the model modes, b_{g_i} are the model parameters, and i is the number of the retained modes and parameters.

The combination of the two previous models naturally led to the *statistical appearance model* [26]. Object shapes and intensities are linked together in the analysis of their variation. For each object both shape and intensity parameters are extracted:

$$b = \begin{pmatrix} W_s b_s \\ b_g \end{pmatrix} = \begin{pmatrix} W_s \Phi_s^T (x - \bar{x}) \\ \Phi_g^T (g - \bar{g}) \end{pmatrix}, \tag{1.4}$$

where b represents the combined parameter matrix of one instance of the dataset, and b_s and b_g represent all the modes from the statistical shape and intensity model, respectively. Since shape and intensity parameters are represented by different units, the shape parameters are multiplied by the matrix W_s in order to make the parameters directly comparable. W_s is calculated as $W_s = rI$, where r is the square root of the ratio between the total variation obtained from the statistical intensity model and the total variation calculated from the statistical shape model, and I is the identity matrix. The statistical appearance model is then created using:

$$b \approx \sum_i \Phi_{c_i} b_{c_i} \tag{1.5}$$

where b are the combined parameters of one instance of the training dataset, b_{c_i} are the retained combined parameters of the model and Φ_{c_i} are the corresponding retained combined modes given by:

$$\Phi_{c_i} = \begin{pmatrix} \Phi_{c,s_i} \\ \Phi_{c,g_i} \end{pmatrix} \tag{1.6}$$

where Φ_{c,s_i} represents the shape component of the combined modes and Φ_{c,g_i} represents the intensity part of the combined modes.

Creation of plausible instances

Besides describing the variability of the original dataset in an efficient and compact way, statistical models allow the creation of new instances which are part of the same statistical distribution as the original dataset.

From the *statistical shape model* new instances are created assigning defined values to the shape parameters of Eq. 1.2. In order to have plausible new shapes, the parameters b_{s_i} have to be within bounds:

$$-3\sqrt{\lambda_i} \leq b_{s_i} \leq +3\sqrt{\lambda_i} \tag{1.7}$$

where the λ_i are the considered model eigenvalues. The parameters b_{s_i} are limited by three times the variance since most of the population lies within three standard deviations of the mean (Fig.1.17a) [25].

New plausible instances can be created also for the *statistical intensity model* and the *statistical appearance model*. In the first case, the intensity parameters b_{g_i} substitute the shape parameters b_{s_i} in Eq. 1.7 and are then used in Eq.1.3 to create the new instances. In the second case the combined

parameters are fist calculated substituting b_{s_i} with b_{c_i} in Eq. 1.7. Then the calculated parameters are used to create the new instances, which combine shape and intensity variations:

$$\begin{aligned} x &= \bar{x} + \Phi_s W_{s_i}^i \Phi_{c,s_i} b_{c_i} \\ g &= \bar{g} + \Phi_g \Phi_{g,s_i} b_{c_i} \end{aligned} \tag{1.8}$$

In this case the new instances are created generating the shape-free grey level distribution g and warping it to the shape described by x (Fig.1.17b) [24].

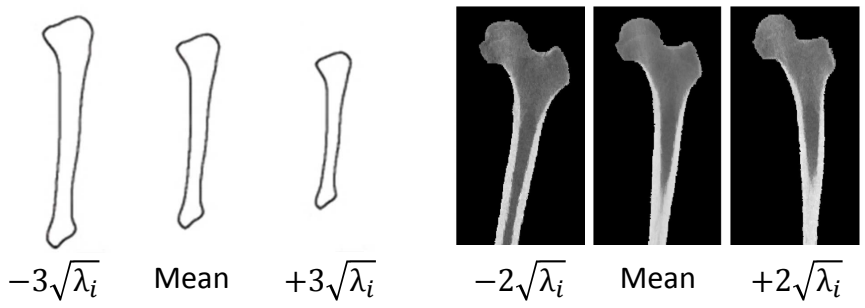

Figure 1.17: New instances created from (a) a statistical shape model of tibia and (b) a statistical appearance model of femur. (Modified from [68, 89].)

Since their development, statistical models have been applied in many fields of medical image analysis. They have been used to study both human anatomy [2, 74, 109, 86, 69] and morphological changes induced by various pathologies [12, 16, 106]. Moreover they have been used as a powerful technique in many medical images analysis challenges, like model-based segmentation [25, 36, 103], 2D/3D reconstruction [126, 4, 8, 35, 129] and prediction of shapes from sparse data [72, 90, 91, 7, 128].

Validation of statistical models

The validation of statistical models concerns two aspects of the model. One one hand the quality of the representation is evaluated, i.e. the ability of the model to map each element of the training dataset to the points in the object space. On the other hand the quality of the model is assessed, i.e. the ability of the model to create a probability density function in the object space based on the representation [31]. In the following, formulations will be presented for the statistical shape model, but they can be easily extended to the statistical intensity model and statistical appearance model.

The quality of the *representation* is evaluated on the training dataset. After building the model, for each shape the parameters can be extracted:

$$b_s = \Phi_s (x - \bar{x}) \tag{1.9}$$

A retained number of modes and parameters is then considered and substituted in Eq. 1.2 to recreate the original shape. The distance between the original shape and the reconstructed one gives a measure of the representation of the model.

The quality of the *model* is evaluated considering three different metrics. The model *compactness* detects the ability of the model at describing the original data with the smallest possible numbers of parameters. A measurement of the compactness is represented by the proportion in percentage of the current eigenvalue with respect to all eigenvalues. The model *generalization* is the ability of the model to create shapes that are not part of the dataset. The same formulation as the representation is used (Eq. 1.9), with the difference that the tested shapes are not part of the training dataset. If the training dataset is constituted by a small number of examples, the leave-one-out procedure is used, where the model is created from all elements but one and tested on the missing element. Finally the model's *specificity* is the ability of the model to create plausible shapes, i.e. shape which are valid example of the class of the object, not only the specific instance of the training dataset. The specificity is measured as the smallest distance between a newly created shape and its closest neighbour in the shape space [31].

1.3.2 Applications in bone mechanics

In the last few years, statistical models have been introduced in orthopaedics. They have been used for description of bone geometry [2, 15, 51, 12], segmentation of bones from volumetric images [36], 2D/3D reconstruction of bones in terms of geometry [4, 128], and geometry combined with mineral density [54]. Moreover statistical models have been used for discrimination of patological subjects from non pathological [12], fracture risk assessment [16, 106] and implant design [68, 11].

More recently, statistical appearance models have been used in bone mechanics as a tool to analyze bone shape and mechanical properties, and their strict interdependence. In 2006, Querol et al. proposed a preliminary study on statistical appearance model for the evaluation of bone stiffness [89]. She created a femur appearance model from 11 non-rigidly registered CT images and tested vertical loading on three new instances. Three years later, Bryan et al. created a mesh-based appearance model from a dataset of 46 femur CT images and evaluated the risk of fracture on 1000 new instances using FE simulations [16, 15]. In 2010, Schuler et al. used an image-based approach to create an appearance model from 100 femur CT images and to predict femur fracture risk using a multilinear regression model [106]. In some of these studies [15, 16], bones were represented as volumetric meshes, and anatomical correspondences were detected using mesh morphing techniques. Statistical appearance models were then calculated on mesh points and bone densities at the corresponding mesh points. New instances were finally generated as meshes associated to bone densities. In other studies [89, 106], bones were represented as volumetric images, and correspondences were calculated using image registration techniques. Statistical models were computed on images, and also new instances were generated as images. Images were then transformed into volume meshes in order to perform FEM calculations. So far, no clear evidence of the most suitable approach for finite element studies has been available. Moreover, in all these

studies [16, 15, 89, 106], statistical models were used as a tool to perform population-based studies. However, the potential of statistical models for comparisons among different populations was not exploited. In all cases, models were build on one single dataset representing an homogeneous population and new instances were created from that population.

1.4 Objectives and structure of the thesis

The present thesis had two aims. The first aim was the comparison of image-based and mesh-based approaches for the creation of statistical appearance models, in order to understand which approach is the most suitable for finite element calculations.

The second aim was to explore the potential of statistical models for population-based comparison studies. Statistical models were created for two different orthopaedic applications: bone fracture risk assessment and bone-implant fitting. In the first case femur fracture risk was analysed and compared between male and female subjects. In the second case, bone implant fitting was evaluated for Caucasian and Asian groups.

The body of the present thesis is composed of three main chapters. In Chapter 2, the comparison of image-based and mesh-based statistical appearance models of the femur is presented, underlining the implication for FEM simulations. In Chapter 3, the first population-based application is shown. The femur fracture risk analysis for males and females is calculated using finite element simulations. In Chapter 4, the second application is presented. Bone-implant fitting is evaluated for two different ethnic populations, Caucasian and Asian. The thesis ends with conclusive discussion and outlook in Chapter 5.

Chapter 2

Image-based vs. mesh-based statistical appearance model of the femur

Statistical appearance models have been introduced in bone mechanics for population-based studies. For the creation of statistical models, the main challenge concerns the detection of accurate anatomical correspondences. Correspondences can be calculated with two main approaches: mesh-based and image-based. In the mesh-based approach, objects are represented as meshes and correspondences are detected with mesh morphing techniques. In the image-based approach, objects are represented as images and the correspondences are calculated with image registration algorithms. The correspondence detection method influences not only the representation of the object, but also the creation of the model. In the mesh-based approach, bones shapes are represented by volumetric meshes, and bone mechanical properties are directly associated to mesh nodes. New instances are created as volumetric meshes with mechanical properties associates, and are directly suitable for finite element simulations. In the image-based approach, bones are represented as volumetric images, containing both shape and density information. The new instances are generated as volumetric images and meshes must be created for the mechanical analysis. Finally mesh-based approaches are computational less expensive than image-based approaches.

In this chapter, the comparison of a mesh-based and an image-based approach for finite element simulations is presented. Benefits, drawbacks and computational costs were assessed. Implication for mechanical simulations were considered in terms of quality of the finite element meshes created with the two approaches. The work is described in a paper entitled *Image-based vs. mesh-based approaches to create statistical appearance models of the human femur: Implications for finite element simulations*, which was submitted to 'Medical engineering & physics'. A preliminary conference paper entitled *Mesh-based vs. image-based statistical appearance model of the human femur: A preliminary comparison study for the creation of finite element meshes* was previously presented as oral presentation at the workshop 'Mesh Processing in medical image analysis' during the conference '14^{th} International conference on medical image computing and computer assisted surgery - MICCAI 2011'.

Image-based vs. mesh-based approaches to create statistical appearance models of the human femur: Implications for finite element simulations

Abstract

Statistical models have recently been introduced in computational orthopaedics to investigate the bone geometry and mechanical properties across populations, such as gender or ethnic groups. A fundamental aspect to construct reliable statistical models concerns the establishment of accurate anatomical correspondences among the objects of the training dataset. Various methods have been proposed to solve this problem, such as mesh morphing or image registration algorithms. The objective of this study was to compare a mesh-based and an image-based statistical appearance model for the creation of finite element (FE) meshes. A computer tomography (CT) dataset of 155 human left femurs was used for the comparison. For each approach, 1000 finite element meshes were generated using the respective statistical appearance models. The calculated models were compared according to three main aspects: the quality of the anatomical correspondence detection, the validity of the statistical model and the quality of the obtained FE meshes. Results showed that the mesh-based pipeline had better ability at detecting surface correspondences, could create a more compact model and had low computational costs. On the other side, in the image-based pipeline the volume correspondence detection showed better results and produced finite element meshes of higher quality. In conclusion, the mesh-based approach seemed more suitable when calculation speed is critical, while the image-based approach seemed more appropriate for applications where volumetric accuracy is essential.

2.1 Introduction

During the last decade, statistical shape analysis gained a remarkable popularity within the medical image analysis community. This technique has been extensively used to study human anatomy [2, 74, 109, 86, 69] or the morphological changes induced by various pathologies [12, 16, 106]. In addition, a wide range of clinical applications and tools rely on statistical shape models, such as model-based segmentation [25, 36, 103], 2D/3D reconstruction [126, 4, 8, 35, 129] and prediction of the organ anatomical shape from sparse data [72, 90, 91, 7, 128].

More recently, in orthopaedics these techniques have been extended to include mechanical information. The main function of the human skeleton is to provide a strong mechanical framework that supports the body. Bone shape and mechanical properties are the two most significant parameters responsible for the mechanical stiffness of skeletal structures. For this reason, statistical appearance models have been proposed to combine anatomical shape variations with the local mechanical properties retrieved from CT scan datasets. This approach has been combined with finite element modeling to assess the fracture risk amongst given population groups of femoral

bones [16, 106].

The major difficulty to construct statistical shape model resides in the establishment of accurate correspondences between samples of the training populations. In case of statistical appearance model, this issue becomes even more critical since correspondences have to be established correctly not only on the object surface but also within the object volume. Two different approaches have been proposed to establish volumetric correspondences. The first approach uses volume meshes to establish the correspondence. The reference model is meshed with volumetric elements, which are similar to meshes required for finite-element calculations. Morphing techniques are then used to deform the reference mesh to each object in the training dataset [15, 50]. The second approach uses non-linear image registration techniques to establish the correspondence directly in the image space. Various registration algorithms have been used for this purpose, among others, popular techniques include B-spline registration [98] and the demons algorithm [118].

The image-based and mesh-based methods have distinct advantages and drawbacks when building appearance models for biomechanical calculations. Using a mesh-based approach provides an output directly suitable for the finite element calculations. However, we hypothesize that constrains to ensure well-shaped elements could penalize the accuracy of the anatomical correspondence. As a matter of fact, some degree of smoothing is usually required to regularize the element shape. On the other hand, the image registration approach is not constrained by the element quality, but the resulting model needs to be meshed in a separate post-processing step to be suitable for finite element calculations. As a consequence, meshes obtained for distinct created instances are different, making direct comparison of the mechanical calculations more difficult. In addition, the registration procedure is complex and needs to produce invertible deformation field in order to allow the creation of new instances.

The objective of this study is to compare the statistical models of appearance obtained with the mesh-based and the image-based approaches. Our aim is to determine the best approach to develop a modeling pipeline for biomechanical simulations. Therefore, not only the intrinsic quality of the shape models, but also the quality of the obtained finite element meshes to be used for mechanical finite elements calculations will be assessed.

2.2 Materials and methods

A total of 155 left femur CT images were used in this study; 124 subjects were Caucasian, 28 Asian and 3 African. 70 patients were male and 85 female. The average age was 62 ($\pm$16) years, the average height was 166 ($\pm$7) cm and the average weight was 71 ($\pm$16) Kg. The resolution of the images was between 0.61x0.61 mm and 1.171x1.171 mm, with a slice thickness of 1 mm. From the 155 datasets, 25 were randomly selected for the validation process. The remaining 130 datasets were used for the calculation of the statistical appearance models.

The statistical appearance model was created using two different approaches, namely mesh-based and image-based, as shown in Figure 1 (in the following, the pipeline step listing will refer to the numbering of Fig. 2.1). A similar workflow was used for the two approaches. Both started

from segmented CT images (step 1), established bone anatomical correspondences (step 3), built statistical appearance models (step 4) and created new instances (step 5). In the mesh-based approach, FE meshes were created at the beginning of the pipeline (step 2) and all subsequent computations were executed on these meshes. In the image-based approach, all calculations were done in the image space and the FE meshes were created at the end of the pipeline (step 6). All computations were done using VTK 5.6.1 (Visualization Toolkit, Kitware) and ITK 3.20.0 (Insight Toolkit, Kitware) libraries.

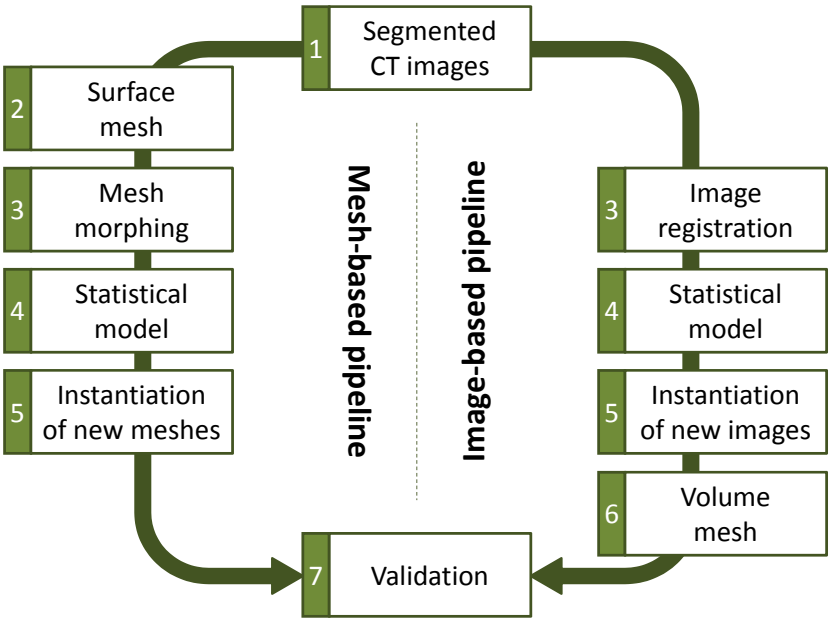

Figure 2.1: Mesh-based (left) and image-based (right) statistical appearance model pipelines for the creation of femur finite element meshes.

2.2.1 Image segmentation (step 1)

From the original CT images, femur volume segmentations were performed using Amira (Amira 4, Visage Imaging Inc., USA). For each bone three different labels were created to define cortical bone, trabecular bone and bone marrow, respectively. The three labels were used for the validation of the correspondence detection (step 7).

2.2.2 Surface mesh creation (step 2)

In the mesh-based approach, a surface mesh describing the bone outer surface was generated for each dataset at the beginning of the pipeline. From the segmented CT image, the surface mesh was created using the marching cube algorithm [73]. The obtained mesh was decimated to about 40,000 nodes and smoothed using the Laplacian operator to improve its quality. Since in many

6 cases this procedure caused problems in maintaining a good mesh topology, node connections were reestablished using MRFSurface [85].

2.2.3 Correspondences establishment (step 3)

Bone anatomical correspondences among the dataset objects were found using a mesh morphing technique in the mesh-based approach, and using an image registration algorithm in the image-based approach. In both cases, correspondences were calculated with respect to the same reference bone. The choice of the reference bone was done using an iterative procedure. First one bone was randomly selected as the reference and all the remaining bones of the dataset were registered to it. The average transformation was then calculated and the bone whose transformation was the closest to the average transformation was considered as the new reference femur. These steps were repeated until convergence.

In the mesh-based pipeline,mesh morphing was performed using the algorithm developed by [9]. First, the reference bone was converted from a surface mesh to a FE volume mesh using NETGEN [105]. The mesh was composed of about 130,000 quadratic tetrahedrons, to satisfy the necessary level of mesh refinement for femur FE simulations [121]. To compute the mesh morphing, 10 landmarks were manually selected on the surface of the reference volume mesh (Fig. 2.2). As for the reference, the 10 landmarks were manually selected on each surface mesh of the dataset. After a rigid alignment, the reference surface mesh was morphed to each bone of the dataset by means of radial basis functions (RBF), constraining the transformation with the selected landmarks. In order to ensure geometrical accuracy, the reference surface mesh was projected onto the bone geometry, and then smoothed to enhance its quality. Finally the volume morphing was executed, positioning each volume node by interpolating the displacement of the surface nodes and optimizing its location to avoid element distortion.

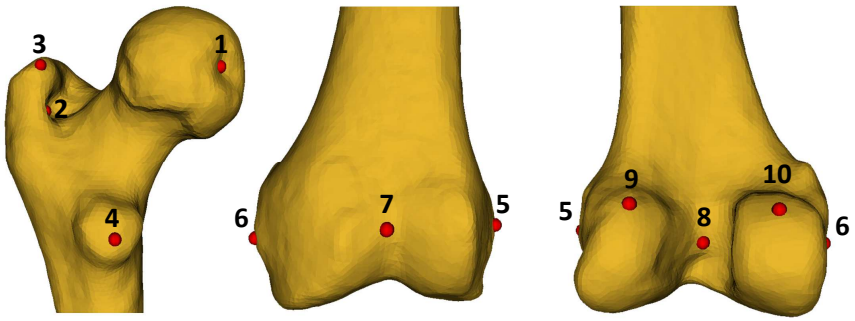

Figure 2.2: Landmarks selection for mesh morphing. (a) Selection of four landmarks in the femur head (1: fovea of the femur; 2: posterior lateral femur neck: 3: greater trochanter; 4: small trochanter). (b) and (c) Selection of six landmarks in the femur condyles (anterior and posterior views) (5: lateral epicondyle; 6: medial epicondyle; 7: intercondyle ; 8: patellar surface of femur; 9: lateral condyle; 10: medial condyle).

In the image-based pipeline, correspondences were detected using the Log-Demons registration algorithm. A very important feature of this technique is that deformation vector fields (DVF) obtained from the registration are smooth and invertible [118]. DVF are generated as the exponential of stationary velocity fields (SVF), which are the primary results of the registration optimization process [1]. Demons were regularized with a femur-specific polyaffine model [107] to properly capture the main anatomical variation of the femur shape. In the polyaffine model, femurs were divided in three regions (femur head, shaft and condyles). The parameters of the polyaffine model where then jointly estimated using a closed form least square solution during each iteration of the calculation of the SVF.

2.2.4 Statistical models (step 4)

For each pipeline, first a *statistical shape model* was calculated in order to detect and define the variability of the shapes within a dataset [25]. In the mesh-based approach, the statistical shape model was computed on the nodal coordinates of the FE mesh. In order to calculate the principal component analysis (PCA), the volume meshes were previously rigidly aligned using the Procrustes algorithm [39]. In the image-based approach, the statistical shape model was computed as a statistical deformation model [97], therefore the PCA was calculated on the SVF obtained from the image registration process.

As second step, a *statistical intensity model* was computed in order to find and describe the variability of intensities within a dataset [26]. It has been shown that CT intensities and bone mechanical properties are strictly correlated [99]. CT image grey levels are linked to bone mineral density [21], which is related to the Young's modulus through empirical relationships [46]. For the mesh-based approach, the statistical intensity model was created considering the image intensity values at the corresponding nodal positions. In order to take into account the partial volume effect that occurs on the bone surface [47], the bone outer layer was first eroded to delete the partial volume effect area and then dilated to rebuild the cancelled outer cortical bone. At each node of the mesh, intensities were calculated through a linear interpolation of 26 neighboring voxels. For the image-based approach, all images were warped to the reference bone shape, in order to have spatial correspondence among the grey level of the dataset images. The PCA was computed on the warped images.

Finally a *statistical appearance model* was created by combining the parameters obtained from both the statistical shape model and the statistical intensity model [26].

2.2.5 Instantiation of new samples (step 5)

For both pipelines, new instances were created from the statistical appearance model. The new instances plausibility was guaranteed by considering the variation of each mode within the 95% of the Gaussian distribution. The sampling of the variation parameters was done using the latin hypercube algorithm. To create each new instance, the calculated intensities were assigned to the reference bone shape. The obtained grey level distributions were then transformed to the calculated

new instance bone morphology.

2.2.6 Volume mesh creation (step 6)

At the end of the image-based approach, a FE mesh was created for each new instance. The meshing procedure is the same as the one used at the beginning of the mesh-based pipeline (step 2); from each CT image, the bone surface mesh was extracted using the marching cubes algorithm. The mesh was then simplified, smoothed and its topology reestablished. Finally each surface mesh was converted to a quadratic FE mesh consisting of about 130,000 tetrahedral elements.

2.2.7 Models validation and comparison (step 7)

Evaluation of the anatomical correspondence detection (step 3)

On the bone surface, for each femur, the Hausdorff distance was calculated bidirectionally between the original surface and the surface obtained after the non-rigid deformation. The highest distance among the two was considered in order to highlight the failures of the non-rigid transformation techniques. In the bone volume, the overlapping between the reference bone and the transformed bone was calculated for cortical bone, trabecular bone and bone marrow. For the mesh-based pipeline, the overlapping was computed considering the number of nodes in the overlapping region, whereas the Dice coefficient [116] was used for the image-based pipeline.

Validation of the statistical appearance model (step 4)

Both statistical appearance models were validated using three criteria [31]. The model compactness measured the ability of the model at describing the data using the smallest amount of parameters, and was calculated as the accumulation of the normalized PCA variance. The model representation measured the ability of the model at mapping the original dataset in the new PCA space. It consisted in the recreation of 25 randomly selected bones from the original training dataset, using the model parameters. The model generalization measured the ability of the model at recreating objects that were not part of the original. It was computed on the 25 bones excluded from the model creation. For each metric, each femur was recreated starting from mode number 1 and adding 10 modes for each recalculation, until reaching the total amount of modes, where the bone was eventually completely rebuilt.

Validation of the creation of FE meshes for the new instances (step 5)

Three criteria were used to evaluate the quality of the finite element meshes: Jacobian, edge ratio and minimum angle, which correspond to metrics describing the element volume, size and shape, respectively. The *Jacobian* described the distortion of the element from the ideal shape. A Jacobian value lower than zero characterized a strongly distorted (negative volume) element, inappropriate for finite element calculations. The *edge ratio* was calculated as the ratio between

the longest and the shortest edge of each element. The *minimum angle* was computed as the smallest angle between two side planes of each element.

2.3 Results

2.3.1 Validation of the anatomical correspondence detection (step 3)

On the *bone surface*, the mesh-based pipeline average Hausdorff distance for the validation of the surface correspondences was less than 3 mm, which was nearly half of the distance calculated for the image-based pipeline (Table 2.1a). In the *bone volume*, the layer overlapping showed lower registration accuracy for the mesh-based pipeline (Table 2.1b), whereas an overlapping ratio greater than 80% was calculated for the image-based pipeline.

Table 2.1: Evaluation of the anatomical correspondence detection results. (a) Surface measurement of correspondence. The Husdorff distance used for both the mesh-based and the image-based approached. (b) Volume measurement of correspondence. Mask overlapping used for the mesh-based approach, Dice coefficient used for the image-based approach.

surface metric	mesh-based pipeline	image-based pipeline
Hausdorff distance [mm]	2.71 ± 1.21	5.10 ± 1.17

(a)

volume metric	mesh-based pipeline	image-based pipeline
cortical bone overlapping [%]	65.67 ± 6.02	85.42 ± 7.90
trabecular bone overlapping [%]	73.29 ± 11.15	85.64 ± 9.14
marrow bone overlapping [%]	75.29 ± 15.11	79.24 ± 10.34

(b)

2.3.2 Validation of the statistical appearance model (step 4)

The mesh-based statistical appearance model had a greater *compactness* than the image-based model from about 6% to 15% for the first 60 modes (Fig. 2.3). The mesh-based model was able to describe the 95% of the dataset variation at the 66^{th} mode, whereas the image-based model reached the 95% of compactness at the 98^{th} mode.

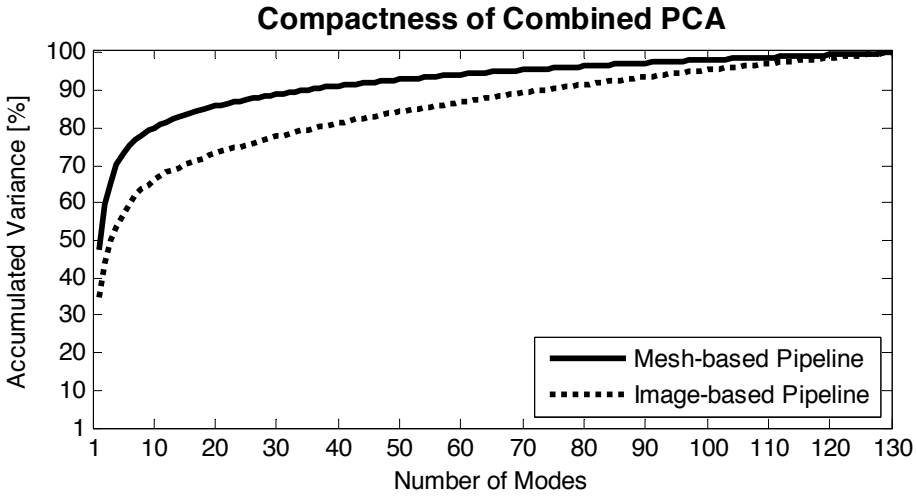

Figure 2.3: Compactness of the statistical appearance models calculated with the mesh-based and the image-based approaches.

For the model *representation* (Fig.2.4a), the mesh-based approach performed better at recreating the original bone shape with a small amount of modes. The reconstruction error was less than 2 mm for the first mode, whereas it was more than 5 mm for the image-based method. On the other hand, in the recreation of the original intensities, the image-based pipeline was able to recreate the original values with a reconstruction error of about 0.3% for the first mode, whereas the mesh-based approach had reconstruction error of about 7%.

Similarly to the representation, in the model *generalization* (Fig.2.4b), the mesh-based approach showed better capability at recreating the shape using a low number of modes. For both methods, a plateau of the reconstruction error was reached at mode 30, where the error was of about 1mm for the mesh-based approach and less than 2mm for the image-based approach. The recreation of the intensity was better performed by the image-based approach, which had a reconstruction error of about 6HU (0.3% of the HU range) at the first mode, and did not decrease significantly for further increase of the number of modes. The mesh-based approach, instead, had a reconstruction error that decreased from about 125HU (7% of the HU range) at the first mode of variation to about 80HU (4% of the HU range) at mode number 40, where the plateau started.

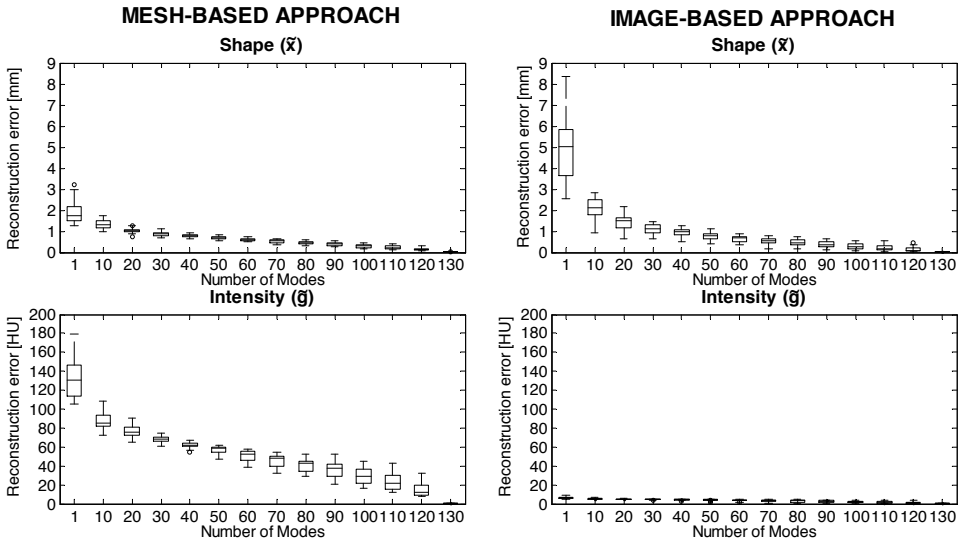

(a)

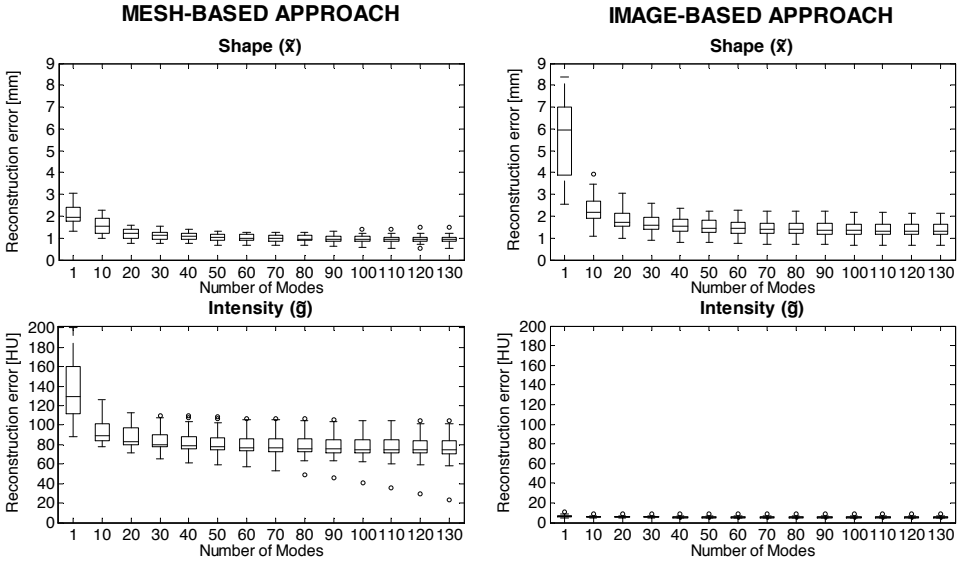

(b)

Figure 2.4: Validation of the statistical appearance model through representation (a) and generalization (b). For each metric, bone shape and intensity reconstruction errors are represented for both the mesh-based (left) and the image-based (right) approaches.

2.3.3 Validation of the creation of FE meshes for the new instances (step 5)

For both the mesh-based and the image-based approaches, 1000 new instances were created in order to cover 90% of the variation included in the statistical appearance model. Therefore the new bones were calculated using 34 modes of variation for the mesh-based pipeline and 73 modes of variation for the image-based pipeline. In the mesh-based pipeline, 139 meshes out of 1000 had elements with null or negative *Jacobians*. All the meshes created with the image-based pipeline were suitable for FE calculation and had a positive Jacobian. The FE meshes created with the mesh-based pipeline had less homogeneous *edge ratio* than the meshes created with the image-based pipeline, both in terms of average and standard deviation (Fig. 2.5a). A similar behavior was shown for the *minimum angle* results (Fig. 2.5b).

2.3.4 Computational costs

The differences in terms of computational costs between the mesh-based and the image-based approach are shown in (Table 2.2). In the mesh-bases approach the computation of the model was in the order of minutes, whereas for the image-based approach the timing was in the order or hours. The creation of the new instances required seconds in the mesh-based pipeline, whereas it required minutes in the image-based pipeline.

Table 2.2: Computational costs for the calculation the statistical models and the creation of the new instances for the mesh-based and the image-based pipeline. For the new instance generation, the shown time refers to the creation of one instance; in the image-based pipeline it refers to both the computation of the new CT image and the transformation to a FE mesh.

Process	Mesh-based pipeline	Image-based pipeline
Shape Model	11 min[2]	4.2 hrs[1]
Intensity Model	2 min[2]	1.2 hrs[1]
Appearance Model	1 min[2]	65 hrs[2]
New instance	10 sec[2]	6 min[2]

[1] Processor: Intel Xeon CPU, X5550 @ 2.67GHz. RAM: 48GB
[2] Processor: Intel Core Duo, E8500 @ 3.16GHz. RAM: 8GB

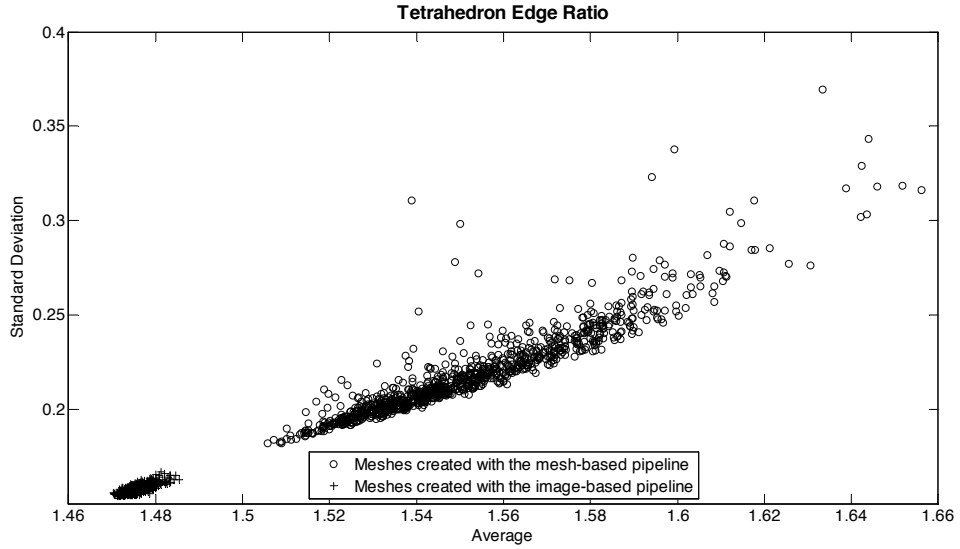

(a)

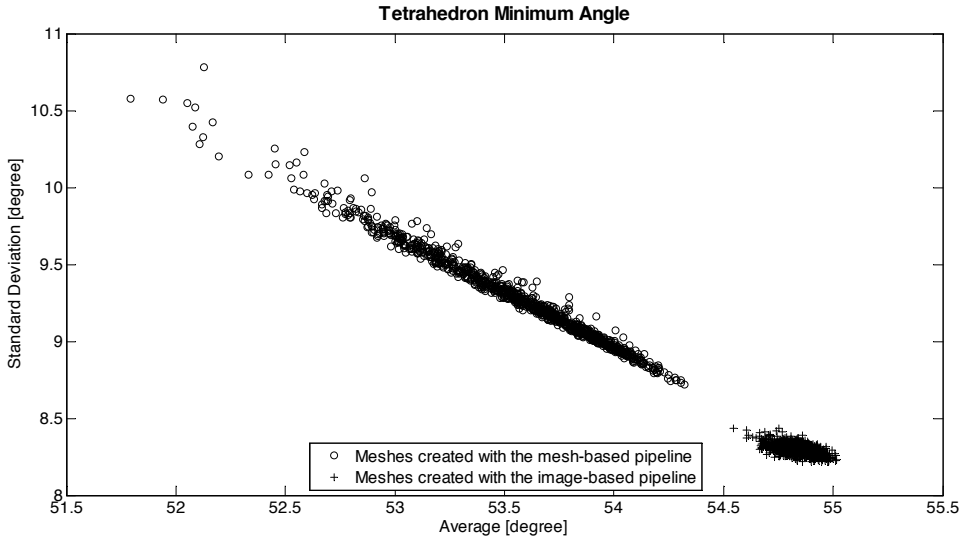

(b)

Figure 2.5: Comparison of tetrahedron edge ratio (a) and tetrahedron minimum angle (b) for the new instances, in both mesh-based and image-based approaches. Each symbol represents the average (x axis) and the standard deviation (y axis) of the metric for each mesh.

2.4 Discussion

Two approaches to build statistical models of appearance were compared in order to assess their respective strength and weaknesses towards accurate mechanical simulations. Each approach is based on a different method to determine the anatomical correspondences, but the methods used for the construction of the statistical appearance model and the generation of new instances were identical. Results showed that the accuracy of the mesh-based method was high on the bone surface, whereas the image-based method proved to be more accurate inside the bone volume.

One of the major differences between the proposed approaches concerns the establishment of the anatomical correspondence. The detection of bone anatomical correspondences was performed using a landmark-based mesh morphing technique for the mesh-based pipeline and a polyaffine log-demon registration algorithm in the image-based pipeline. These two techniques were used in recent publications [9, 106] and they can be considered as state of the art for each approach. Each technique had to fulfill constrains to ensure accurate results in order to allow producing both valid statistic appearance models and plausible new instances. In the image-based pipeline, the correspondence detection step created DVF describing voxel displacements from the target image (each bone of the original dataset) to the reference image. During the creation of the new instances the direction of the DVF had to be inverted in order to generate new instances from the reference image. DVF inversion is guaranteed by diffeomorphic registration techniques, such as Large Deformation Diffeomorphic Metric Mapping [79], Log-Demons [118] and Free Form Deformation [96]. In this work, the Log-Demons were chosen considering their higher computational efficiency [119] and their existing implementation for femurs [107]. In the mesh-based pipeline, the correspondence detection step guaranteed the quality of the mesh, but this did not imply the creation of valid meshes as new instances.

The quality of the correspondence obtained on the bone surface by the mesh-morphing technique resulted from the algorithm used to calculate the morphing parameters. The landmarks selected on the bone surface were used to constrain the morphing process. In addition, the mesh outer surface was iteratively back-projected onto the target bone geometry, which avoided large deviation between the morphed and target geometry shapes. On the other hand, no information was used to control the volumetric morphing, which was only constrained by the quality of the finite elements. Consequently, Laplacian smoothing was performed to ensure good element quality, which penalized the quality of the correspondence inside the bone volume. The situation was different in the image registration case, where correspondences were determined based on the grey level of the image voxels, without taking into account any shape-specific geometrical information. As a result, the calculated registration accuracy was higher in the bone volume for the image-based approach than for the mesh-based technique, whereas opposite findings were obtained concerning the correspondence accuracy on the bone surface. However, it is important to note that the evaluation of the performances of the correspondence establishment step was calculated globally. The assessment of the exact local correspondence on the bone surface had limitations due to the small amount of anatomical features that could be accurately compared among different geometries. The exact correspondence detection appeared even more challenging in the bone volume,

where no precise morphological structures could be identified.

The compactness of the statistical appearance model was higher in the mesh-based approach, where the original data variation could be described using a smaller number of modes. However, in the mesh-based approach, the correspondence between the anatomical points inside the volume mesh were mostly driven by the requirement to maintain the elements quality in the finite element mesh, limiting the correctness of the anatomical correspondences. This behavior is expected to decrease the variability of the information included in the PCA model, while keeping the shape distribution of the finite element mesh similar to the reference 'well-shaped' mesh. Similarly, results concerning representation and generalization of the statistical models reflected the achievements of the correspondence detection algorithms. Therefore the mesh-based pipeline showed a better ability to re-create the shape of the femur, whereas the image-based pipeline showed a better ability at reproducing bone density.

The FE meshes created with the two pipelines showed striking difference in terms of mesh quality. More than 10% of the meshes created with the mesh-based pipeline had null or negative Jacobian, which means that they could not be used for FE simulations. On the other side, all the meshes created at the end of the image-based pipeline could be used for mechanical computations. The high quality of the FE mesh obtained with the image-based approach was not surprising, since it was calculated at the end of the process and did not suffer from constrains required by the mesh-morphing registration step. However, the percentage of inappropriate elements obtained after mesh-morphing is surprisingly high and could be problematic to calculate population-based biomechanical behavior. It should also be noted that it would not be possible to simply use the deformation vector field calculated with the image registration to morph a generic finite element mesh to all bone instances. This morphing would result in many distorted elements for each mesh generated. This observation highlights the strong constrains required to maintain the element quality during the morphing procedure and, consequently, the trade-off between element quality and registration accuracy required for the mesh-based approach.

Finally, the mesh-based and the image-based approaches showed remarkable differences in terms of computational costs. In the mesh-based pipeline, the calculation of the model and the creation of new instances required lower computational memory and time. Computational costs could be critical for some applications, especially for application of the models involving optimization procedures or real time prediction. However, the issue is not always critical, for example when dealing with population-based studies or implant design. In addition, the actual finite element calculations, which constitute the next step of the process, could also involve heavy costs especially for non-linear contact problems, which occur frequently in biomechanical applications. In addition, most of the time is required to build the shape mode, which is only done once, and the generation of new instances only takes a limited amount of time.

Finite element models developed from CT data are commonly used to evaluate the mechanical performance of the bone. However, most analyses take no account of the wide variation in material properties and geometry that may occur in natural tissues. Only few studies investigated the use of statistical appearance models to include of bone variability [15, 89, 106]. In a recent publication,

Bryan et al. [15] used a mesh-based approach, very similar to the one presented in this study, to create a statistical appearance model of the femur for the prediction of fracture risk in a given bone population. Not enough data are available to directly compare the morphing results, but the values obtained for the model compactness and representation were similar to the values obtained in the presented work. An image-based approach has been followed by Schuler et al. [106] to build a statistical appearance model from a dataset of 100 femurs. They used diffeomorphic demons as registration technique in order to ensure the invertibility of the DVF, but they did not investigate the creation and quality of FE meshes, therefore no further comparison could be investigated.

The comparison of the two pipelines for the creation of a statistical appearance model was done considering the current state-of-the-art techniques. As a consequence, the algorithms used to detect the anatomical correspondences had some methodological differences, which did not affect the conceptual finding of the study. Moreover the creation of two completely independent pipelines allowed avoiding possible bias. Another limitation of the current study is the lack of proper calibration for the CT datasets, which is critical when dealing with mechanical simulations. However, this aspect does not affect the results of the present study, because we compared the ability of the approach to generate statistical models and not the performance of these models when simulating reality.

In conclusion, this study demonstrates that the image-based pipeline performs better in terms of accuracy of the volume correspondence detection and the quality of the FE mesh, while the mesh-based approach produces iso-topological meshes and performes better in term of computational efficiency. Based on these results it is impossible to give a definitive answer concerning the method to adapt, which should be determined for each specific application, but we can conclude that the mesh-based approach seems more suitable when calculation speed is critical, while the image-based approach seems more appropriate for applications where volumetric accuracy is essential.

Chapter 3

Statistical appearance model for fracture risk assessment

When bones cannot withstand applied forces, fractures occur. Fracture risk is a measure of the probability of incurring fractures. Clinically, fracture risk is calculated evaluating bone mineral density from X-ray images. However it has been shown that mechanical calculation add information to the assessment of fracture risk. One of the main limitations of mechanical studies is the small amount of subject involved. This implies difficulties at generalizing the findings for a broader population. Statistical models have the potential to overcome this limitation, since they are able to describe a dataset in terms of shape and intensity variability, and allow the creation of new instances that are part of the same distribution as the original dataset. Moreover population-based studies can be performed when considering various groups, based on different population characteristics, like gender, age groups, etc.

In this chapter, a study about statistical appearance model for fracture risk evaluation is presented. The original dataset of left femur computer tomography images was divided in two groups, using gender as criterion. From each dataset, a statistical appearance model was calculated and a large number of new instances was created. From the created instances, volume meshes were generated in order to perform finite element simulations. Fracture risk was calculated both in stance and sideways fall conditions. A comparison between men and women was performed. Moreover, for each new bone, correlations between fracture risk and geometrical measurements, mechanical properties and applied loads were evaluated. This study is described in the paper in the following pages and represent a preliminary step towards a submission to a journal paper.

Statistical appearance model of the human femur for fracture risk assessment: comparison between men and women in stance and sideways fall situation

Abstract

Fractures occur when bones can not withstand the applied force. Mechanical evaluations of the risk of fracture are performed on few patient-specific cases, implying difficulties at generalizing the findings to a broader population. Statistical appearance models have recently been introduced in bone mechanics to perform population-based studies, since they allow both the description of shape and mineral density variability, and the creation of a large number of new plausible instances. In this study, image-based statistical appearance models of the human femur were created using a dataset of 72 computer tomography (CT) images for men and 72 for women. For both genders, 1000 new bones were instantiated from the model and transformed to finite element (FE) meshes. Bone fracture risk was calculated using a maximum principal strain criterion in stance and sideways fall configuration. The fracture risk was then correlated to bone geometrical features, femoral neck Young's modulus and applied load using linear simple and multiple linear regression. Results showed that women had a statistically significant higher fracture risk than men, both in stance and sideways fall configuration. The applied load resulted to be the prevalent predictor for fracture risk. Among geometrical features, the neck-shaft angle was the predominant factor, especially in the stance situation. Mechanical properties showed low contribution to fracture risk prediction.

3.1 Introduction

Fractures occur when the externally applied force exceeds the bone strength [60]. In case of elderly people, fractures happen for age-related bone reduction diseases, like osteoporosis [122]. In 2000, 1.6 million femur osteoporotic fractures were reported worldwide. Female patients represented the 70% of the total amount [56]. Osteoporotic fractures are affected by several clinical factors, such as age, smoking, parental history of hip fracture, etc. [58]. They are also correlated to bone geometry and bone mineral density, both for men and women [43, 29].

The fracture risk is a measure of the probability of incurring in a fracture. Clinically, the fracture risk is evaluated through imaging techniques that are able to capture bone mineral density [59]. In dual energy X-ray absorptiometry (DXA) images, bone mineral density is calculated in a standardized rectangular area of the femoral neck. The computed bone mineral density is then compared to classified values, in order to define the patient's fracture risk. In quantitative computed tomography (QCT) images, bone mineral density is evaluated in a volume of interest of the femoral neck, considering also the differentiation between cortical and trabecular bone. A standardized technique for the fracture risk assessment is however still missing [84].

Mechanical calculations add relevant information to the clinical evaluation of the fracture risk, both in case of DXA [114] and QCT images [70]. In mechanical computations, the fracture risk is calculated as the ratio of mechanical measurements, i.e. strains [64], stresses [71] or strengths [65], to a limit value obtained through experimental results. It has been proven that strains give more accurate assessment for fracture risk calculation [100]. Strains are compared to the yield strain, which differs for tensile and compressive situations [3]. The initial failure site for femur fractures is the femoral neck ([28, 100, 32]). In femoral neck, tensile areas are present in the proximal part during stance, and in the distal part during a sideways fall. The opposite occurs for compressive areas [32]. One of the main limitation of mechanical studies is the small amount of subjects involved. Studies are performed for patient-specific situations, therefore generalizations of the findings to a larger population is often difficult. Population-based investigations can overcome this limitation allowing not only the study of the mechanical behavior of a large amount of bones, but also the comparison among different groups of populations.

Statistical models have recently been used for femur mechanics [89, 16, 106]. The aim of statistical models is to the describe anatomical variability within a dataset in a compact way [25]. Morever statistical models allow the creation of new instances belonging to the same distribution as the initial dataset. Statistical models of appearance are a suitable tool in bone mechanics since they describe the variability of bone shape and density and allow the creation of new plausible instances. In previous studies, new femur instances were created from the original dataset and tested mechanically [89, 16] or correlated to mechanical measurements [106]. However these studies were conducted on instances belonging to one population, without exploiting the potential for population comparison.

The aim of this study was twofold. On one side, we aimed at exploiting the suitability of statistical models for population-based studies in bone mechanics. We therefore created statical appearance models of the human femur for two different populations, men and women, and generated new instances for each group. On the other side, we aimed at evaluating the fracture risk in the femur neck using a strain-based procedure. The fracture risk was compared for men and women and correlated with bone geometry, mineral density, and applied loadings.

3.2 Materials and methods

For the present study a dataset of 72 left femur CT images was used for both men and for women. Among men, 50 subjects were Caucasian, 21 Asian and 1 African. For 19 patients, data were missing. For the remaining, the average age was 60 years (range from 23 to 85 years), the average height was 170($\pm$6) cm, the average weight was 74($\pm$17) Kg and the body mass index (BMI) was 25.5($\pm$4.9) Kg/m^2. Among women, 64 subjects were Caucasian, 7 Asian and 1 African. For 10 patients, data were missing. For the remaining, the average age was 46 years (range from 21 to 90 years), the average height was 163($\pm$6) cm, the average weight was 70($\pm$16) Kg and the body mass index (BMI) was 26.4($\pm$6.0) Kg/m^2. CT images had original resolution ranging from 0.610x0.610 mm to 1.171x1.171 mm and a slice thickness of 1 mm.

3.2.1 Statistical appearance model

For each gender, the statistical appearance model was calculated using the image-based approach described by Bonaretti et al. [10]. In order to find anatomical correspondences, bone images were registered to a reference image using polyaffine demons [107]. Then for each group, principal component analysis was calculated and statistical appearance model computed. For each gender, 1000 bones were created as new CT images, transforming the reference bone to new instances through deformation vector fields. The new bones were generated as linear combination of 13 modes, which represented 75% of the dataset variation both in terms of shape and intensity. Each mode was weighted by a factor ranging between ± 1.5 standard deviation of the corresponding variability, represented by the principal component eigenvalue. The weighting factor was selected using latin hypercube sampling in order to generate a plausible parameter distribution.

3.2.2 Finite element model

Finite element simulations were computed to assess the femur fracture risk in stance and sideways fall conditions for both men and women.

Bone geometries were automatically computed from the images created with the statistical appearance models, following the pipeline proposed by Bonaretti et al. [10]. From each image, surface meshes were extracted, simplified and smoothed, in order to make them suitable for the following step. Then surface meshes were converted to quadratic tetrahedron meshes using NetGen [105]. The number of elements of the resulting meshes ranged from about 92000 to about 145000, in order to guarantee adequate mesh refinement [47].

Bone material properties were automatically calculated from the CT image Hounsfield Units (HU), as proposed by Schileo et al. [99]. However the dataset at our disposal was constituted of non calibrated images. Therefore a pseudo-calibration was performed to convert HU to ρ_{ash}, which represents the mineral part of the bone. The same empirical regression line was used for all new instances. The minimum bone density was set to 0.10 g/cm^3, whereas the maximum bone density was set to 1.08 g/cm^3 [63]. Bone mineral density was then converted to ρ_{app}, the density of the bone when considering both its fluid and solid phases. The conversion was done using a ratio of 0.60, which is within the range identified in the literature [41, 62]. Finally the apparent density was used to calculate the Young's modulus for each node of bone meshes, using the femur-specific equation proposed by Morgan et al. [80]:

$$E = 6.850\rho_{app}^{1.49} \tag{3.1}$$

For each node of the meshes, the corresponding grey level was calculated considering the average on 26 neighbouring voxels. The resulting HU was transformed to Young's modulus and associated to the corresponding node. The partial volume effect was also considered. The bone outer layer was first eroded to delete the partial volume effect area and then dilated to rebuild the cancelled outer cortical bone [47]. A Poisson ratio of 0.3 was assumed [123]. Simulations were

run in Abaqus 6.10 (Simulia, Providence, USA) using a nodal approach. In this approach the Young's modulus is associated to the temperature variable through a linear relationship [47].

Forces and boundary conditions were applied using two different coordinates systems (Fig 3.1). The force coordinate system was created considering the bone shaft axis as the z axis, and the neck axis as the x axis [5]. The boundary condition coordinate system was built considering the first axis passing through femur head fovea and intercondyle area, whereas the second axis as connecting the two epicondyles [108].

For each bone, the applied forces were computed as function of the body weight. Since the bones were created from the two statistical appearance models, body weights had to be calculated. Weights were predicted from subjects' body heights using the BMI formulation [16]. Each subject's height was calculated considering the femur length to be the 26.75% of the total height. Given the body height, the BMI was then randomly selected from the BMI distribution of the original dataset, considering an interval within ± 1.5 standard deviation.

In the stance situation (Fig 3.1a), the applied force included body weight and muscle action, resulting in a total applied force of 2.5 times the body weight [49]. The body weight was applied in the hip contact (P0). Muscles forces were calculated as a percentage of the body weight, in x, y and z directions. The forces due to abductor, tensor fascia latae proximal and tensor fascia latae distal were applied in P1, whereas the force due to vastus lateralis was applied in P2. Physiological boundary conditions were considered [108]. At the femur head, one node (P0) was constrained in two translational degrees of freedom, in order to allow only bone head deflection towards the epicondyles. In the intercondyle area, one node (P4) was constrained in three degrees of freedom to represent the knee joint. Finally in the lateral epicondyle, a node (P1) was constrained with one degree of freedom to prevent the rotation of the bone around its axis.

In the sideways fall situation (Fig 3.1b), the applied force had a magnitude of 2.5 times the body weight, as in the stance situation. The force was applied in the hip contact node (P0), considering an angle of 10 degrees with respect to the ground and of 15 degrees with respect to the neck axis [87]. The action of muscles was considedered neglectable. Femurs were fully constrained in three nodes. The full constrains were located in a node of the greater trochanter (P1), to simulate the contact to the floor, in a node in the intercondyle area (P4), to simulate the knee joint, and in a node in the laterial epicondyle (P3), to avoid torsion of the femurs along its axis.

Forces and boundary condition application points were selected on the reference bone and then automatically propagated to each new bone, exploiting the deformation vector fields used for the creation of the new bones.

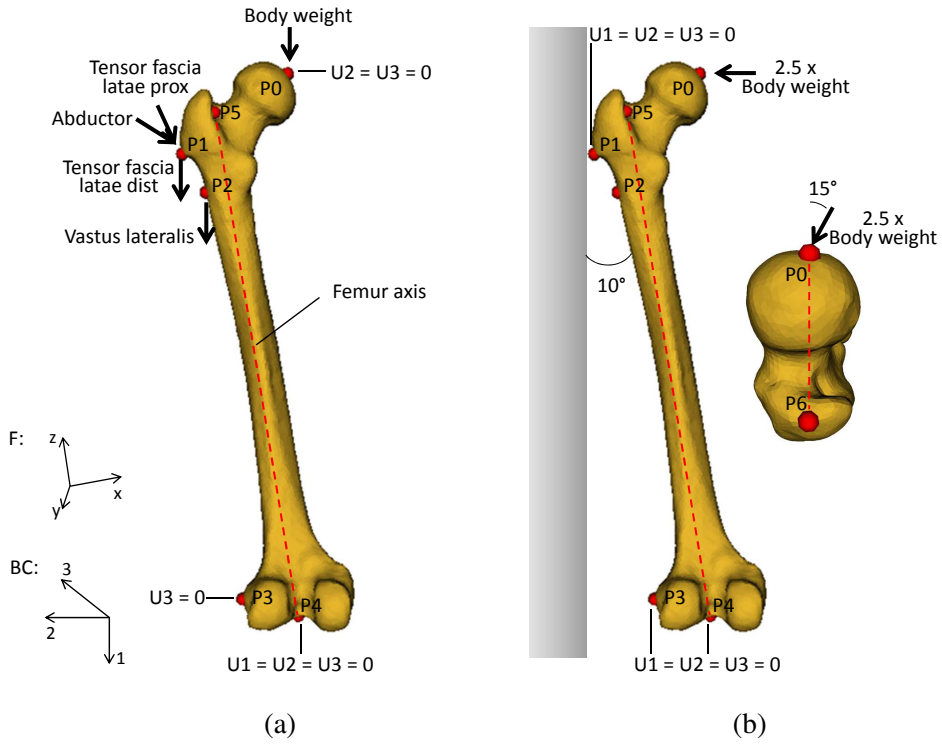

Figure 3.1: Boundary condition for the calculation of the femur fracture risk for (a) the stance situation and (b) the sideways fall situation. The forces are applied using the coordinate system x,y,z. The boundary conditions are considered in the coordinate system 1,2,3. In the boundary condition coordinate system, U represents the node displacement.

3.2.3 Fracture risk calculation

The fracture risk was calculated in the femur neck, which is the initial failure site in case of fracture. In stance situations, fractures start in the proximal neck, whereas in sideways fall conditions, fractures begin either in the proximal or in the distal neck [28, 100, 32]. To calculate the fracture risk, volumes of interest in proximal and distal neck were extracted with a two step procedure. In the first step, two seed points were selected on the reference bone, one in the proximal anterior side and one in the proximal posterior side. The points were then propagated to each instance with the corresponding deformation vector field. For each instance, from the two seed points, four layers of connected elements were considered and united to create the volume of interest. Within the volume of interest, the point of maximum strain was then selected as new seed point. In the second step, from the new seed point, four layers of connected elements were selected as final volume of interest. To create the distal neck region or interest, a similar procedure was used, but starting from one seed point positioned below the femur neck. One initial point was sufficient since in the distal neck the high strain region was concentrated in the same site for all bones. For

each volume of interest, the femur fracture risk was calculated using the maximum principal strain criterion [100]. The fracture risk was computed as the ratio between the average strains in the volume of interest to a threshold strain (ε_{lim}). In case of compression, $\varepsilon_{lim} = 1.04\%$, in case of tension $\varepsilon_{lim} = 0.73\%$ [3]. In stance configuration, the fracture risk was calculated only for the proximal neck. In sideways fall configuration, the fracture risk considered was the maximum between the fracture risk in the proximal neck and the fracture risk in the distal neck. Men and women fracture risks were compared using the unpaired Student's t-test, both for the stance and the sideways fall configurations.

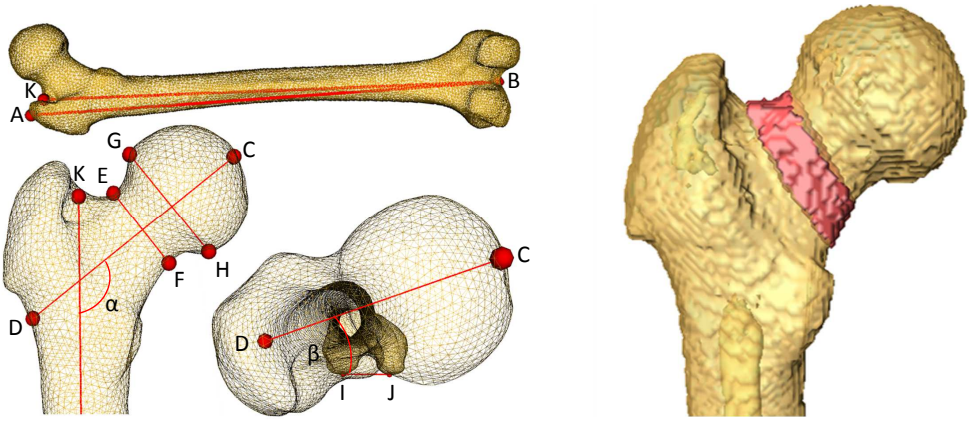

(a) (b)

Figure 3.2: Bone parameters considered for fracture risk evaluation. (a) Geometrical measurement. AB = femur length; CD = femoral neck length; EF = femoral neck diameter; GH = femoral head diameter; α = neck-shaft angle (calculated between femoral axis (KB) and femoral neck length (CD)); β = anteversion angle (calculated between femoral neck length (CD) and posterior condyles (IJ)). (b) Mechanical properties measurements. The red ring represents the volumetric region of interest for the extraction of the Young's modulus.

For both men and women, and for both stance and sideways fall situations, fracture risks were correlated to bone parameters that represent possible fracture risk predictors. The considered predictors were geometrical measurements, mechanical properties and body weight. A total of 6 geometric measurements were considered [43, 16] (Fig. 3.2a): femur length, neck length, neck width, head width, neck-shaft angle and anteversion angle. The points defining the geometrical measurements were manually picked on the reference femur and then automatically propagated to all femurs using deformation vector fields. Mechanical properties were selected in the femoral neck. A cylindrical volume was manually defined in the reference bone (Fig. 3.2b) and then propagated to all bones using deformation vector fields. For each bone, the average of the Young's modulus in the femoral neck was considered. In order to calculate regressions, each fracture risk predictor was centered and normalized. Relationships between fracture risk and bone parameters were evaluated in two different ways. First, single regression was computed. Fracture risks were regressed with one bone parameter at a time, using linear correlation. Then, stepwise linear

multiple regression was calculated. Fracture risks were regressed with all variables in a forward selection modality. The regression started with no variables. Then variables were included in the model one by one, adding each time the variable with higher statistical significance. Finally a multiple regression model was calculated with the bone parameters selected by the stepwise procedure, and the predicted fracture risks were compared to the measured fracture risks.

3.3 Results

Two left femur statistical appearance models were created, one for men and one for women. Both models described their original dataset with very similar compactness (Table 3.1). For each gender, 1000 instances were created as CT images and converted to finite element volume meshes. All meshes were considered valid for finite element simulations by the quality check tool of the finite element software Abaqus.

Table 3.1: Compactness of the statistical appearance model for men and women subjects.

Model compactness	Men (# modes)	Women (# modes)
50%	2	3
75%	13	13
80%	20	20
90%	40	40
95%	54	53
100%	71	71

Bone strains were calculated for each gender and both in stance and sideways fall configurations. In stance, strains were $0.08 \pm 0.02\%$ for men and $0.09 \pm 0.03\%$ for women. In sideways falling, strains were $0.17 \pm 0.05\%$ for men and $0.19 \pm 0.05\%$ for female. From bone strains, fracture risk was computed. In stance, the fracture risk resulted for men and $13 \pm 4\%$ for women. In 1 case for men and in 4 cases for women, the fracture risk was higher in compression than in tension. In side-ways falling, the fracture risk was $17 \pm 4.5\%$ for men and $19 \pm 5\%$ for women. In 815 cases for men and in 891 cases for women, the fracture risk was higher in the proximal femoral neck, where the maximum strains were found in compression. When the highest risk of fracture was located in the distal femoral neck, the maximum strains were found in tension. Both in stance and side-wise fall situations, unpaired Student t-tests were performed to evaluate the difference between men and women. In both configurations, fracture risks were higher for women than for men ($p<0.01$).

For each gender and for each configuration, relationships between fracture risk and geometrical measurements, mechanical properties and applied loadings (Table 3.2) were investigated.

Table 3.2: Measured bone geometry, bone mechanical properties, and applied force for men and women.

Measurements	Men (Mean ± Std.dev)	Women (Mean ± Std.dev)
Length (AB) [cm]	42.6 ± 2.9	40.8 ± 2.5
Neck length (CD) [cm]	10.5 ± 0.8	9.9 ± 0.5
Neck width (EF) [cm]	3.9 ± 0.3	3.6 ± 0.2
Head width (GH) [cm]	5.0 ± 0.5	4.5 ± 0.5
Neck-shaft angle (α) [degree]	128 ± 4	130 ± 4
Anteversion angle (β) [degree]	15 ± 7	19 ± 7
Young's modulus [GPa]	2.7 ± 0.7	3.4 ± 0.5
Body weight [Kg]	64 ± 14	60 ± 14

First, single linear regression between bone fracture risk and bone parameters was calculated. In stance configuration, body weight and neck-shaft angle had the highest coefficients both for men and women (Table 3.3a). In both cases, the coefficient values were very close within the gender group. For men, the neck-shaft angle was the highest, followed by the body weight, whereas for women it was the opposite. Mechanical properties had lower coefficients for both genders. All regressions had statistical significance for men, whereas regressions with head width, Young's modulus and femur length had not statistical significance for women. In side-ways fall configuration, body weight was the main predictor both for men and women (Table 3.3b). Mechanical properties had higher influence on fracture risk than in the stance configuration. Among the geometrical measurements, femur length was the most significant for men, whereas neck length was the most significant for women. For women, the regression of the fracture risk with the anteversion angle was not statistically significant. Regression with body weight, mechanical properties and neck-shaft angle, are illustrated in Fig. 3.3a for the stance configuration, and in Fig. 3.3b for the sideways fall configuration.

Table 3.3: Single regression between fracture risk and bone parameters. (a) Stance situation. (b) Side-ways fall situation. For each gender, bone parameters are ordered considering the absolute values of the regression coefficients R^2.

Men				Women			
Measurement	Coeff	R^2	p-value	Measurement	Coeff	R^2	p-value
N-s. angle (α) [1]	-0.41	0.17	< 0.01	Body weight	0.51	0.26	< 0.01
Body weight	0.39	0.15	< 0.01	N-s. angle (α) [1]	-0.50	0.25	< 0.01
Neck width (EF)	-0.24	0.06	< 0.01	Antev. angle (β) [2]	-0.40	0.16	< 0.01
Head width (GH)	-0.21	0.04	< 0.01	Neck length (CD)	0.12	0.01	< 0.01
Neck length (CD)	-0.17	0.03	< 0.01	Neck width (EF)	0.04	< 0.01	0.15
Length (AB)	-0.15	0.02	< 0.01	Head width (GH)	0.04	< 0.01	0.16
Young's modulus	0.13	0.02	< 0.01	Young's modulus	0.04	< 0.01	0.18
Antev. angle (β) [2]	-0.13	0.02	< 0.01	Length (AB)	-0.007	< 0.01	0.81

[1] Neck-shaft angle (α)
[2] Anteversion angle (β)

(a)

Men				Women			
Measurement	Coeff	R^2	p-value	Measurement	Coeff	R^2	p-value
Body weigth	0.83	0.69	< 0.01	Body weigth	0.69	0.47	< 0.01
Length (AB)	0.56	0.32	< 0.01	Young's modulus	-0.13	0.02	< 0.01
Young's modulus	-0.58	0.34	< 0.01	Neck length (CD)	0.11	0.01	< 0.01
Head width (GH)	0.53	0.28	< 0.01	Neck width (EF)	0.10	< 0.01	< 0.01
Neck length (CD)	0.47	0.23	< 0.01	N-s. angle (α) [1]	0.10	0.01	< 0.01
Neck width (EF)	0.43	0.18	< 0.01	Length (AB)	0.07	< 0.01	< 0.01
N-s. angle (α) [1]	0.34	0.12	< 0.01	Head width (GH)	0.07	< 0.01	< 0.01
Antev. angle (β)[2]	0.12	0.02	< 0.01	Antev. angle (β)[2]	0.02	< 0.01	0.77

[1] Neck-shaft angle (α)
[2] Anteversion angle (β)

(b)

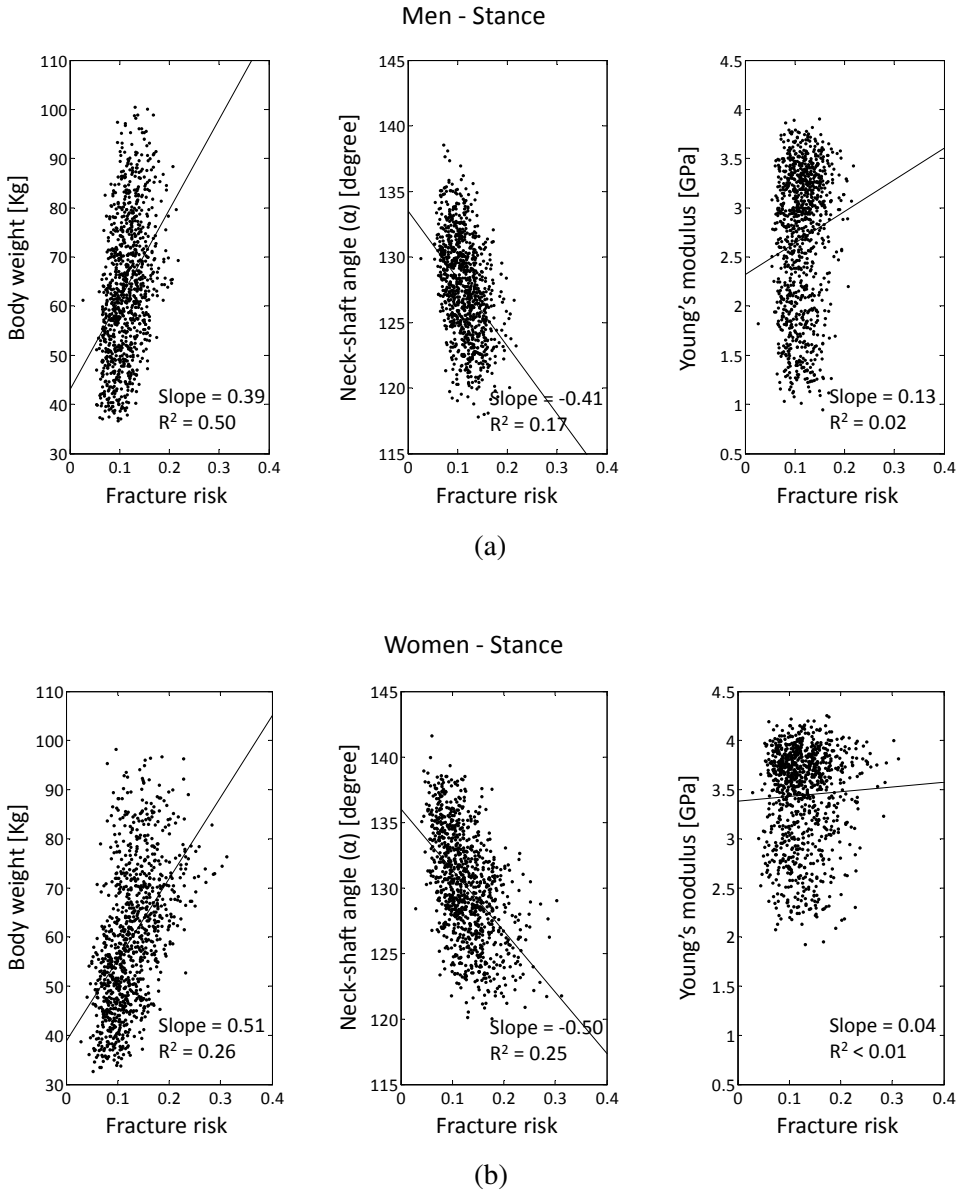

Figure 3.3: Single regression between fracture risk and body weight, neck-shaft angle and Young's modulus in the stance configuration for (a) men and (b) women.

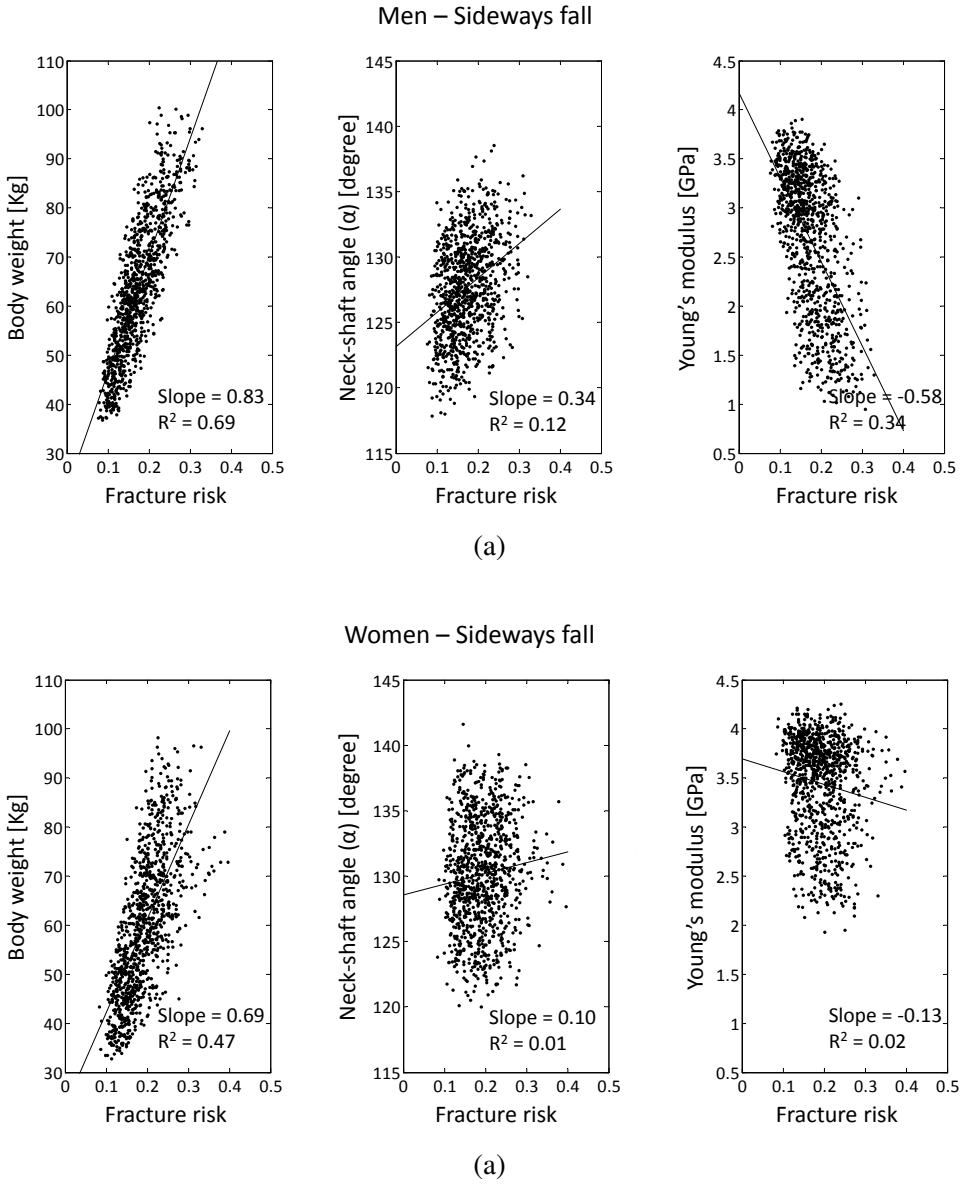

Figure 3.4: Single regression between fracture risk and body weight, neck-shaft angle and Young's modulus in the sideways fall configuration for (a) men and (b) women.

Finally multiple linear regression between bone fracture risk and bone parameters was calculated. A stepwise approach was used to select the parameters with statistical significance. In the stance situation (Table 3.4a), both for men and women, body weight and neck-shaft angle resulted to be the first two included parameters, confirming the findings of single regressions. The mechanical properties were not included in the model for women, and were the least significant parameters for men. In total 7 significant parameters were identified for men and 4 for women.

Fig. 3.5a shows the comparison between fracture risks measured from simulations and fracture risks calculated from multiple regression models using the significant parameters. In the sideways fall situation (Table 3.4b), body weight was the most significant predictor for men and women, as found for single correlations. The Young's modulus resulted more significant for men than for women. Among the geometrical measurements, the neck-shaft angle resulted the most significant for men and the second most significant for women. A total of 7 predictors for men and 6 predictors for women were identified as significant. The comparison between fracture risks measured from finite element calculations and fracture risks predicted with multiple regression models using the significant parameters are shown in Fig. 3.5b.

Table 3.4: Stepwise multiple regression between fracture risk and bone parameters. (a) Stance situation. (b) Sideways fall situation. For each step, accumulated R^2 and p-value are indicated for the multiple regression models created with the selected variables. Slope coefficient refer to the model with all variables included.

	Men				Women			
Step	Measurement	R^2	p-value	Coeff	Measurement	R^2	p-value	Coeff
1	N-s. angle (α) [1]	-0.49	< 0.01	0.17	Body weight	0.69	< 0.01	0.26
2	Body weight	0.84	< 0.01	0.36	N-s. angle (α) [1]	-0.45	< 0.01	0.43
3	Neck width (EF)	-0.73	< 0.01	0.64	Length (AB)	-0.61	< 0.01	0.62
4	Antev. angle (β) [2]	-0.24	< 0.01	0.68	Antev. angle (β) [2]	-0.31	< 0.01	0.70
5	Length (AB)	-0.45	< 0.01	0.69				
6	Neck length (CD)	0.42	< 0.01	0.70				
7	Young's modulus	-0.16	< 0.01	0.71				

[1] Neck-shaft angle (α)
[2] Anteversion angle (β)

(a)

	Men				Women			
Step	Measurement	R^2	p-value	Coeff	Measurement	R^2	p-value	Coeff
1	Body weight	0.78	< 0.01	0.69	Body weight	0.89	< 0.01	0.47
2	N-s. angle (α) [1]	0.23	< 0.01	0.76	Length (AB)	-0.44	< 0.01	0.59
3	Young's modulus	-0.28	< 0.01	0.77	N-s. angle (α) [1]	0.16	< 0.01	0.61
4	Neck width (EF)	-0.56	< 0.01	0.79	Neck length (CD)	0.27	< 0.01	0.62
5	Neck length (CD)	0.32	< 0.01	0.80	Young's modulus	-0.23	< 0.01	0.63
6	Length (AB)	-0.26	< 0.01	0.80	Head width (GH)	-0.34	< 0.01	0.63
7	Head width (GH)	0.27	< 0.01	0.80				

[1] Neck-shaft angle (α)

(b)

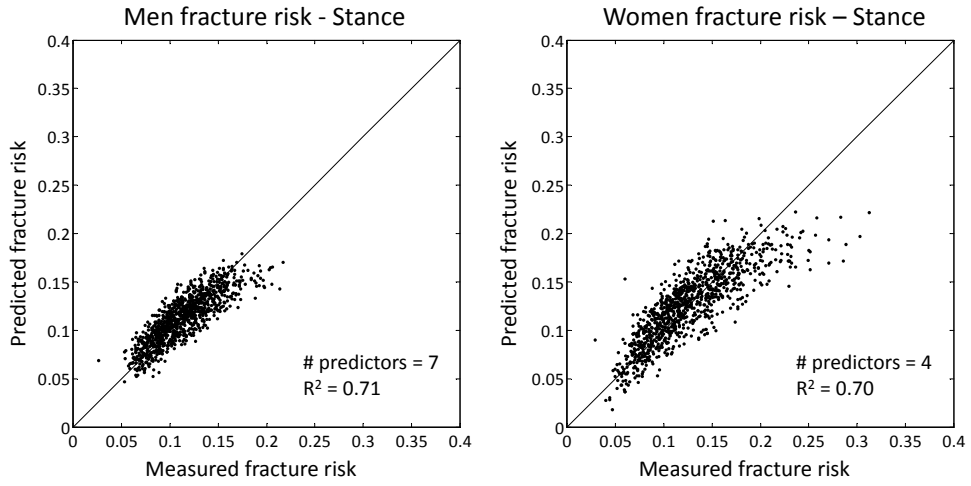

(a)

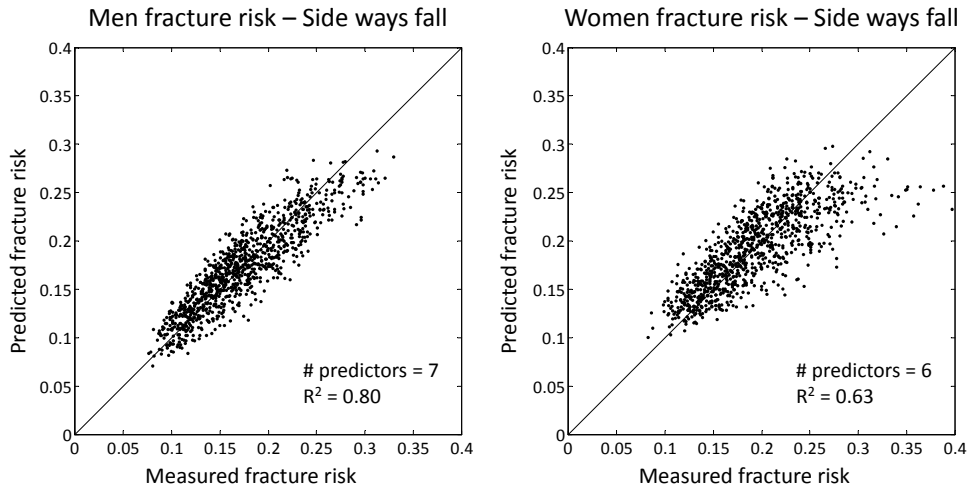

(b)

Figure 3.5: Comparison between fracture risk measured from the finite element simulations and the fracture risk predicted by multivariate models for both men and female in (a) stance and (b) sideways falling configurations.

3.4 Discussion

In this study, a statistical appearance model of the human femur for population-based fracture risk assessment was presented. Fracture risk was calculated for men and women, both in stance and sideways fall conditions. Moreover fracture risk prediction was considered with respect to bone geometry, material properties and applied loads. Results showed a statistically significant higher fracture risk for women than for men. Among predictors, applied loads had the main influence on fracture risk, neck-shaft angle represented the most predominant geometrical predictor, and neck Young's modulus showed low contribution.

Femoral neck fracture risk was calculated for men and women using a maximum principle strain criterion. A maximum principle strain criterion was chosen since it resulted to have higher estimation accuracy than stress criteria [100]. In stance configuration, strains were largely below the yield strain (0.20%) [3], whereas in sideways fall situation, strains were very close to the yield strain. This implied the calculation of lower fracture risks for stance condition than for sideways fall condition [75]. The result could be explained considering that bone can bear vertical loads more than transverse loads. Fracture risks were statistically significant higher for women than for men, confirming differences between the two genders, as found in other studies that analyzed bone mineral density [29] and strength [66] with relation to fracture risk.

For both genders and configurations, body weight resulted to be the most relevant predictor for fracture risk. An exception was represented by men in stance, where the body weight was the second most relevant predictor. However also in this case, the weight added relevant contribution to the model. In all cases, body weight was positively correlated to fracture risk. This could be explained if considering bone as a beam. Body weight was linearly related to the applied load. The increase of load magnitude determines the rise of higher strains and therefore of risk of fracture.

Bone mechanical properties resulted to have low influence on fracture risk for both genders. Mechanical properties seemed to have slightly higher importance in stance configuration, although their contributions remained small. Low influence was confirmed by some studies [83] and contradicted by others [29]. However the impossibility of having calibrated images for this study could have influenced these findings, as explained below.

Among geometrical properties, the neck-shaft angle showed a predominant role in stance configuration, and a lower contribution in sideways fall configuration, both for men and women. The neck-shaft angle was negatively correlated with fracture risk in stance configuration, and positively correlated in falling situation. Both positive and negative correlations were found in previous studies [38, 16]. Magnitudes and signs of these correlations could find explanation in beam theory. In stance configuration, the load is applied vertically and a larger angle allows bones to better sustain the applied force. In sideways fall configuration, loads are applied laterally and small angles increase shear. From the multiple regressions analysis, two other geometrical features resulted relevant. In stance configuration, anteversion angle added relevant contribution to the regression model. The negative regression could be explained by an increase of the lever arm.

The calculated multiple regression models had good prediction accuracy. Regression models were able to predict 60-80% of the risk of fracture. Moreover, the most prevalent part of the

prediction was due to two parameters, body weight and neck-shaft angle. Information to fracture risk assessment could therefore be add with a few measurements easily performed in clinics.

The assessment of femoral fracture risk from population studies based on statistical appearance models has been addressed in two different work [16, 106]. In the first work, femoral fracture risk was assessed for a population of 1000 new instances and in sideways fall configuration. A total of 28 femur were found at risk of fracture. However the loading conditions were slightly different from the current study and the fracture risk was evaluated in the whole femoral head. Correlations between fracture risk, bone density and geometrical measurements were also investigated. Bone mineral density resulted to have high influence on the fracture risk, differently to what found in this study for the Young's modulus, to which density is exponentially related. However the bone mineral density was considered not only in the femoral neck, but in the whole femoral head. In the second, femur fracture risk was predicted from statistical appearance models calculated in different regions of femurs. For each region, the statistical appearance model parameters were used as predictors of fracture risk using linear regression. Statistical and not physical predictors were used, therefore a direct comparison with the present work is difficult.

The main limitation of this study concerned the use of non calibrated CT images. Calibration is fundamental for a correct calculation and interpretation of the results from mechanical simulations. However efforts were made to perform a pseudo-calibration, in order to obtain plausible results. Care was taken also in the assignment of the mechanical properties to the finite element meshes to minimize other sources of possible imperfections, such as partial volume effect. Moreover, since all images were pseudo-calibrated with the same linear relationship, the findings of the study can be considered consistent. An other limitation concerned the determination of the body weight for the new instances. Both in stance and load configurations, the applied load was 2.5 times the body weight. For each instance, the body weight was calculated from the body mass index, excluding other possible parameters. The inclusion of bone mineral density in the computation of the applied forces could add more plausibility to the instances body weight. Finally linear single and multiple regressions were used to correlate bone fracture risk with geometrical measurements, mechanical properties and applied loads. They could relate data with good correlation, missing from 40 to 20% of the complete information. The remaining missing information could be investigated with non linear regression.

In conclusion, this study has confirmed the potential of statistical appearance models for population-based studies. Fracture risk was evaluated on large groups of plausible instances, distinguishing between men and women. The complete automation of the processes allowed also the assessment of correlations with applied loading, geometrical measurements and mechanical properties. Statistical appearance models offer therefore the potential of moving from case-specific to population-based studies in bone finite element modeling.

Chapter 4

Statistical shape model for orthopaedic implant design

Orthopaedics implants are designed integrating knowledge on bone anatomy from literature with results obtained from experimental tests on cadaver bones. In these studies, variations in bone shapes and mechanical properties, which depend on age, gender, ethnicity, etc., are rarely taken into account in a rationalized way. This limitation implies the need of implant contouring during the surgery in order to fit the bone anatomy. No patient-specific adjustment is made to adapt implant and screw position to the subject's bone characteristics. In order to overcome this situation, ideally patient-specific implant would be preferable. However high time and economical costs are required, and a practical solution is far from being available. One intermediate solution could be the creation of population-based implants. Implants could therefore be created specifically for different groups, such as male and female, Caucasian, Asian and African, etc.

In the following pages, a preliminary study about the use of statistical models for implant design is presented. Two population groups were involved, considering the ethnicity criterion, Caucasian and Asian. The comparison between the two groups involved the evaluation of both bone-implant fitting and mechanical assessment. The study was conceived and realized at the beginning of my PhD studies. My main contribution regarded the creation of the fracture of the instances and the creation of the results for the bone-implant fitting. This work was presented as an oral presentation entitled *Assessment of peri-articular implant fitting based on statistical FE modeling* during the workshop 'Computational Biomechanics for Medicine III' at the '11$^{\text{th}}$ International Conference on Medical Image Computing and Computer Assisted Intervention - MICCAI 2008'.

Since 2008, a few studies have been proposed for bone implant design using statistical models. In particular, statistical shape models have been used for fitting assessment using mesh-based approaches. Implant shapes were adapted to bone anatomy through optimization processes on bone groups created from statistical shape models [68]. Minimization of plate torsion and bending during surgery was also considered as a criterion to optimize plate shape [11]. However, no study has been presented that considers statistical models for the analysis of bone-implant coupling in terms of mechanical behaviour. Bone-implant mechanical response is still analysed using subject-specific approaches [44, 102].

Assessment of peri-articular implant fitting based on statistical FE modeling

Abstract

We present a framework for statistical finite element analysis allowing the statistical evaluation of biomechanical performance of peri-articular implants across a given population. In this paper, we focus on the design of orthopaedic implants that fit a maximum percentage of the target population, both in terms of geometry and biomechanical stability. A statistical shape model of left tibia was built and used to automatically create fractures at the same anatomical site. An automatic implant fitting algorithm was developed as well to optimize implant position to best fit the bone surface. Afterwards finite element analysis is performed to analyze the biomechanical performance of the bone/implant construct. The mechanical behavior of different PCA bone instances is compared for tibia representing the Asian and Caucasian populations.

4.1 Introduction

Current design processes for orthopaedic implants rely on very limited information about the shape of the target bone. Such information may be in the form of a small set of shape parameters (e.g. lengths and angles) derived from the existing literature, which fails to capture the complexity of real anatomical shapes. Alternatively, tests on cadaver bones can be performed. However, extrapolating the findings reached by such tests to the whole target population can lead to implants that may fit some patients, but not others.

For this reason, the current project uses novel population-based design methods to develop market-specific trauma implants. Our technology allows a compact model that represents the range of shape variation encountered in a given population. The model is computed on a large collections of CT scans, using statistical analysis techniques to determine the average bone shape, as well as the shape distribution around this average in the form of principal components of shape variation. Once the model is built, it allows generating as many bone instances as required to accurately represent the population. Finite element calculations are used to evaluate the biomechanical properties of the generated bone instances. By doing so, we are able to reconstruct the statistical distribution of bone biomechanical properties across the population. Initial evaluations focused on bone strength.

4.2 Material and method

4.2.1 Statistical model of the tibia

Two input datasets composed respectively by 43 Caucasian left tibia CT sets (23 males and 20 females) and 47 Asian left tibia CT sets (28 males and 19 females) were used. The size of each

image was 120x130x140 voxels, with an image resolution of $1mm^3$.

All the input images were pre-processed: after their manual segmentation executed with Amira 4.1.1, they were first rigidly registered and then non-rigidly registered using the methodology presented in [104]. Bone creation was implemented in Matlab 7.0. New shape instances were created using Principal Component Analysis (PCA) [24] applying the following formula:

$$x = \bar{x} + \sum_i \phi_i b_i \tag{4.1}$$

where x contains the coordinates of the new shape, $\bar{x}$ contains the coordinates of the mean one, ϕ_i is the eigenvector and b_i is the shape parameter: $|b_i| \leq \pm 3\sqrt{\lambda}_i$, with λ_i as eigenvalue. As shown in Fig. 4.1 from the shape statistical model, 13 new instances were created for each ethnic group combining the first mode and second mode that represent about 75% of the total variance. Grey level intensities were created warping the mean intensity distribution on each bone. Finally these new instances were used to simulate bone fractures, implant fitting and to study biomechanical properties of the bone-implant structure.

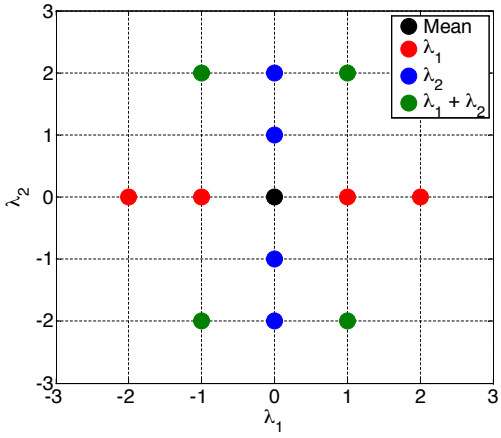

Figure 4.1: Map of the 13 bones created for each ethnic group through shape PCA. Axes correspond to the first and second mode of variation. Each point represents a bone created using the first (red points) and the second mode (blue points) or combining them (green points). The black point represents the mean bone.

4.2.2 Fracture generation and propagation

The type of fracture used for the simulation was 41-B1, according to the A.O. group classification [81]. It is a partially articular fracture in which the lateral condyle is split from the rest of the tibia by an almost vertical cut. This kind of fracture shape allowed us to both simulate a situation that is close to reality and to implement calculations with a reduced computational effort. All the implementation was done with Matlab 7.0. The fracture was created in the same way for Asian and Caucasian image sets. In each group and for the mean bone, the fracture was conceived as an

exact vertical cut (below called 'reference fracture'). The reference fracture was then propagated to all the instances created through PCA in order to obtain 'equivalent' fractures located at the same anatomical site for all the bones (the fractures created in this way will be called 'propagated fractures').

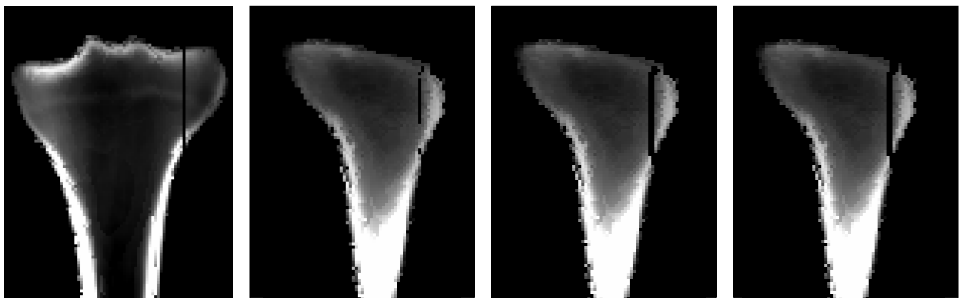

(a) (b) (c) (d)

Figure 4.2: Fracture generation and propagation. (a) Fracture generated as a black sagittal slice in the mean bone. (b) Propagation of the reference fracture to a bone instance using deformation fields. Notice the incomplete fracture. (c) Fracture surface created with Delaunay triangulation; a few voxels are still linked at the edge of the fracture. (d) Elimination of the linking voxels and creation of two completely split bone parts.

The reference fracture was created simply changing to black all the voxels belonging to the same sagittal slice for both Asian and Caucasian (Fig. 4.2a). The creation of the propagated fractures was implemented in an automatic way. The deformation fields obtained after non-rigid registration and used to establish points correspondences for the PCA model, were added to the mean bone fracture coordinates in order to obtain the position of the fracture in the current instance. Differently from the reference fracture, each propagated fracture was not positioned just on one single slice, but it involved modification on more slices (up to 4). Moreover the propagated fractures were not created as a black continuous but as black points spread in few slices (Fig. 4.2b). This is due to the discrete nature of images and deformation fields. In order to perform the following biomechanical analysis the fracture should be continuous, i.e. the bone had to be completely split into two separated parts to create two different meshes. To create a continuous fracture the first approach involved morphological operators (based on connectivity). The obtained results were not satisfactory in terms of fracture thickness. Better results were achieved with an approach that considers the fracture as a continuous surface, created as a Delaunay triangulation, which splits the bone in exactly two parts without any links between them. The black voxels generated through the deformation fields were considered as vertices of the triangles (Fig. 4.3a). Then all the voxels still belonging to the bone that were crossed by a triangle were turned to black and the complete fracture was created, as shown in Fig. 4.2c. However, as it can be seen in Fig. 4.2c, it could happen that at the edges of the fracture there were a few voxels still linking the two parts of the bone. To solve this last issue another triangulation was created with all the black surface voxels as vertices

(Fig. 4.3b). This second surface was expanded one voxel outwards, i.e. turning to black all the voxels that were in the same sagittal slice as the surface edge voxels and next to them. With this last operation the fractures were completed and the bones exactly split into two parts (Fig. 4.2d).

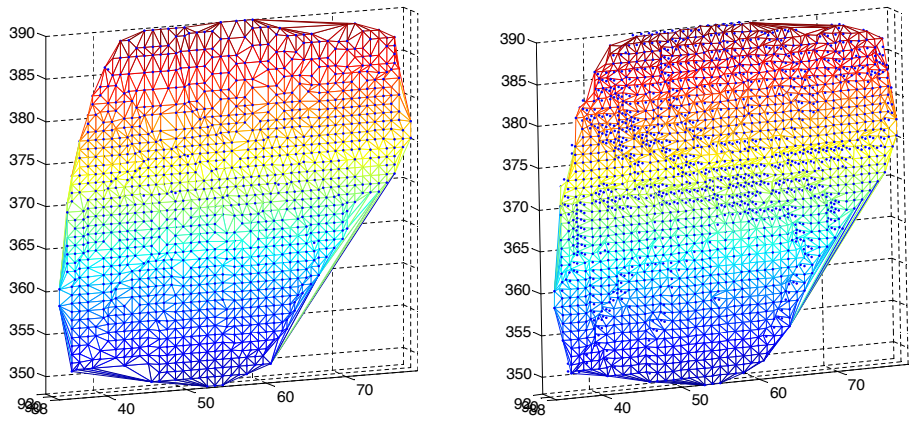

(a) (b)

Figure 4.3: Delaunay triangulations. (a) Triangulation generated with the black voxels obtained through the deformation fields as vertices. (b) Triangulation generated with the surface voxels as vertices.

4.2.3 Implant fitting

The constrained ICP algorithm was used to determine the optimal implant placement on the bone surface. The objective is to minimize the bone/implant distance while taking into account different constraints given by the experience of the implant manufacturer and physical considerations, such as surface collision. The algorithm is based on the optimization of the following functional:

$$argmin \sum_i W_i e_i \tag{4.2}$$

where W_i and e_i are the corresponding weight and distance error for point i in the implant mesh model, respectively. The weights W_i are computed as a linear combination of constraint-specific weights for collision, implant-bone co-linearity and tibia plateau. The last two constraints come from the implant manufacturer and have been established to favour implant fitting:

$$W_i = W_i^C + W_i^{\|} + W_i^p \tag{4.3}$$

The collision weight W_i^C is computed as follows:

$$W_i^p = \begin{cases} 1 & p_i \notin V_{in} \\ k_i^c \parallel e_i \parallel & p_i \in V_{in} \end{cases} \tag{4.4}$$

To detect if a point p_i is inside or outside the bone model, the sign of the dot product between the normal vector on the bone surface closest to p_i and the vector formed by p_i and its closest point on the bone surface is computed. In order to avoid biases due to the number of points inside and outside the volume, the variable k_i^c in Eq. 4.4 was analytically found to be:

$$k_i^c = \frac{N_{tot} - N_{in}}{\sum_{i \in V_{in}} \| e_i \|} \tag{4.5}$$

with N_{tot} the number of points of the implant mesh, N_{in} the number of points falling inside the bone model, and V_{in} the 3-D space inside the bone model. We have found that adjusting the weight k_i^C we avoid biases due to the variations on the number of points inside and outside the bone volume, as the iterations proceed. Similarly as for the collision constraint, weights $W_i^{\|}$ and W_i^p are computed as follows:

$$W_i^{\|} = \begin{cases} 1 & \alpha \leq \alpha_{th} \\ k^{\|} \| \alpha_{th} - \alpha \| & \alpha > \alpha_{th} \end{cases} \tag{4.6}$$

$$W_i^p = \begin{cases} 1 & p_i \in \Gamma \\ k_i^p \| p_i - z_p \| & p_i \notin \Gamma \end{cases} \tag{4.7}$$

Where α is the angle between the implant main axis and the bone main axis, α_{th} is a threshold angle chosen by the user to set together with the weighting factor $k^{\|}$, the sensitivity of the parallelism constraint. The scalar value z_p is the z-coordinate of the plateau region interface, and Γ is the 3-D space above the bone plateau.

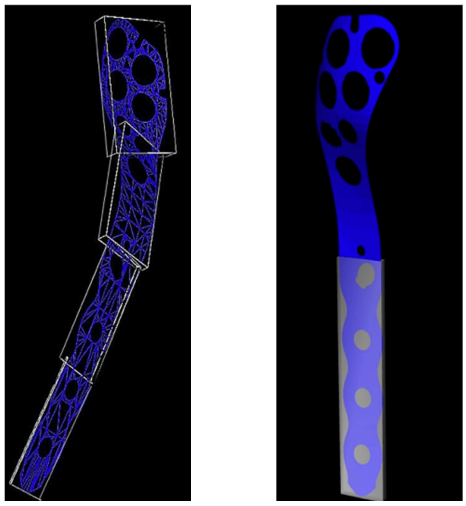

(a) (b)

Figure 4.4: Oriented Bounding Box (OBB) decomposition of the implant shape used to measure deviation of the angle between the main axis of the bone and the lower part of the implant shape. Figure (a) shows a 4-level decomposition and figure (b) shows the main axis of the lower part of the implant obtained after applying a further OBB decomposition of the lower part of the implant.

For the computation of α the main axis of the implant model and the bone are required. This is performed through an Oriented-Bounding-Box (OBB) decomposition of both shapes. Furthermore, for the implant model, only the lower region is used in order to improve the alignment between the bone shaft and the implant. Fig. 4.4a shows a 4-level OBB decomposition of the implant, while Fig. 4.4b shows the aligned bounding-box to the main axis of the implants' lower region.

4.2.4 Biomechanical FE simulations

Finite Element (FE) analysis is a numerical technique to solve partial differential equations over domains of complex shapes. FE techniques find a natural application in biomechanical studies, such as for structural analysis of orthopaedic implants. FE models are useful to assess the design, position and fixation of new implants [17]. A technique to generate FE models representing the target population in terms of shape and mechanical properties is proposed in this study. The statistical models obtained in the former step, average and modes of variation are used to create 3D bone solids representing instances of the population. The obtained bone geometries (both parts of the fractured tibia) are then meshed with a finite number (about 100000) of 3D tetrahedrons. 10-nodes elements with quadratic shape functions were used to ensure good quality to the results. The mechanical properties used in the model are inhomogeneous and depend on the bone density distribution. Since calibrated CT scans were used for the construction of the statistical model, instances of the model will maintain a proportional relationship between the bone relative density and the grey level (Hounsfield Units) in the images. It has been shown that the bone's Young's modulus can be obtained directly from the bone density [112]:

$$E = 6.95\rho^{1.49} \tag{4.8}$$

where E is the Young's modulus in GPa and ρ is the bone relative density (g/cm^3). The Poisson ratio is chosen equal to 0.3 because this parameter is not dependent on bone density. The implant was also discretized with finite elements. The position of the implant on the bone surface was defined by the fitting algorithm described previously. The implant mechanical properties were E = 110 000 Mpa and a Poisson's ratio of 0.3 corresponding to titanium. 3D beam elements were used to fix the implant to the bone. Six beams were used in total - 3 in the proximal part of the bone and 3 in the distal part. The cross section of the beam was assumed circular with a radius of 3.3 mm, which correspond to the diameter of the fixation screws. The attachment of the beam to the bone was performed using an embedded element technique. The embedded element technique is used to specify that an element or group of elements is embedded in 'host' elements. In our situation the beam elements (modeling the screws) are embedded in the bone. If a node of an embedded element lies within a host element, the translational degrees of freedom at the node are eliminated and the node becomes an 'embedded node'. The translational degrees of freedom of the embedded node are constrained to the interpolated values of the corresponding degrees of freedom of the host element. The loading conditions correspond to a 1600 N force (2 times body weight) on the tibia plateau while the distal part of the bone is maintained fixed. A frictionless

unilateral contact law was use to account for the interactions between both bone fragments. In the simulations, locking screws were considered. The locking of the screw on the plate avoids any relative motion between theses two parts and also avoids the compression of the plate on the bone; therefore no contact was considered at the bone/plate interface. In total 26 FE models were built. Only small deformations and displacements were expected, therefore a geometrically linear solver was used for the calculations. The commercial finite element package ABAQUS was used for the simulations.

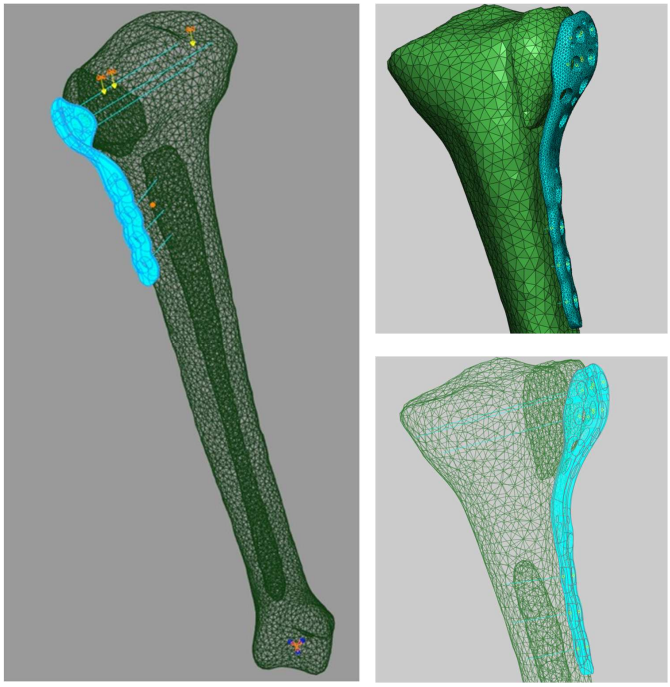

Figure 4.5: Finite element mesh of the bone (including the fracture) with the implant. Beam elements used to model the screws are shown as blue lines. These elements are 'embedded' within the bone elements.

4.3 Results

The quality of the implant fitting was evaluated on each of the bone generated with the statistical model. Results show that the implant better fits the Caucasian population than the Asian group (Fig. 4.6 and Table 4.1). For the Asian bones, the maximal bone/implant distance was found to be up to 7mm. The difference between the two populations was expected since the implant was first designed to target the Caucasian market.

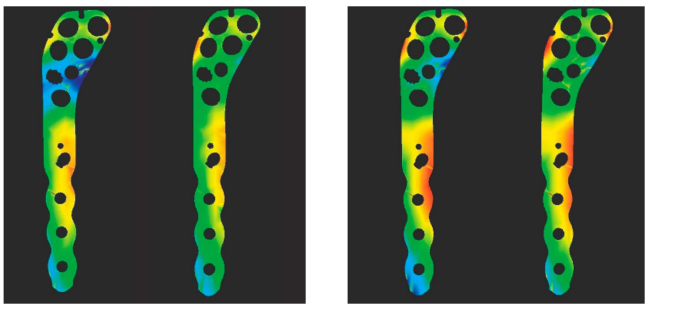

Figure 4.6: Maximal (right) and average (left) distance map for the Asian and Caucasian bone populations. Red indicated a small distance (0mm) and blue indicates a large bone/implant distance up to 7mm for the maximal distance in the Asian population.

Once the optimal position for the implant has been found, biomechanical simulations are used to evaluate the mechanical behavior of the implant for the different populations. For the simple fracture considered in this study, stresses in the implant remain far below Yield stress. However, some differences were visible between the two populations (Table 4.1). The stresses calculated in the plate as well as in the screws are significantly higher ($p < 0.05$) for the Asian than for the Caucasian population. However, no statistical difference was found for the fitting distance in the two populations. Even if the average distance between the bone and the implant was larger for the Asian bones than for the Caucasian bones, the quality of the fit was statistically identical. This result highlights the importance of including biomechanical simulations in the optimization process and that optimization based on the geometrical fitting of the plate is not enough to capture the complexity of the implant biomechanics. Stresses in the implant also correlate to the bone size in the Asian population. A linear correlation (R^2 higher than 0.6) was found between the length of the bone and the maximum von Mises stress in the plate. Higher stresses were calculated for the short bones than for the long one. On the other hand, no correlation was found for the Caucasian bones. This observation indicates that probably more care is required to account for implant size scaling in the Asian bones than for the Caucasian bones.

Table 4.1: Comparison of the biomechanical and geometrical variables between the Asian and the Caucasian models. The first row shows the average of the maximal bone/implant distance calculated using the image-based method described in sections 2-4, while the other two rows contain the average of the maximal von Mises stress in the plate and maximal principle stress in the screws. Variations are given in %.

	Caucasian	Asian
Bone-implant distance [mm]	3.7	4.3
Mises stresses in the plate [MPa]	61	61
Max principal stress in the screws [MPa]	61	80

4.4 Discussion

We presented a framework for statistical biomechanical assessment including a combined statistical model of shape and finite element analysis. The application of our methods for modelling bone shape and mechanical behaviour has been shown for the evaluation of a given peri-articular plate. The statistical model construction and fracture propagation are based on non-rigid registration. This has the advantage that no landmarks or parametric representations need to be defined and the fractures can be placed automatically at the same anatomical site. Future developments will combine shape and intensity information into the statistical model; the model contains information about the correlation between shape and density. This could allow predicting bone density when only shape is known, and this is one of our directions of future work. The FE analysis shown in this work could be improved by addressing a set of experiment setup issues. For example, bone screws were modeled with simple beams embedded in the bone. Obviously, the screw/bone interactions are more complex than this idealized model. Hence, accuracy of this approximation needs to evaluated and validated. Further, the bone geometries were meshed independently from each other, resulting in different FE meshes for the different bones. This leads to difficulties in the direct comparison of the stress distribution between the different bone shapes under consideration, as well as discrepancies in the location of the loading forces applied. The alternative is to deform a pre-defined mesh, such as was done by Yao et al in 2000 [125]. However, it is extremely difficult to ensure the validity of the mesh for further FEA under arbitrary deformations. The target application is orthopaedic implant design. Virtual testing of new implants will in the future replace cadaver testing. Furthermore, being able to study the whole range of bone shapes and densities of the target population will lead to better fitting implants, as well as a considerable cost reduction in the design process. In order to assess the appropriateness of an implant, further development should be done to define the different scenarios of the implant, in terms of positions were the implant is likely to be placed and the force loading conditions. A complementary application of these techniques will be the patient-specific pre-clinical evaluation of an implant; taking into account the particular skeletal anatomy, bone quality, and implant position to assess the biomechanical performance of the implant on the patient.

Chapter 5

Conclusion and outlook

The presented work proposed statistical model of shape and density for population-based studies of bone mechanics, with applications to bone fracture risk and implant design. The first aim was to create and compare two statistical appearance models for the human femur, one image-based and one mesh-based, in order to evaluate the most suitable for finite element simulations. The second aim was to use statistical models for population-based studies investigating bone behavior. Two studies were therefore proposed. The first study investigated femur fracture risk for men and women. The second study analysed bone-plate fitting for Asian and Caucasian.

Image-based vs. mesh-based statistical appearance model of the femur

Recently statistical appearance models have been introduced in bone mechanics for population-based studies. Statistical appearance models allow the description of a dataset in terms of shape and intensity variability. Moreover statistical models allow the creation of new instances that are part of the same distribution of the original dataset, implying the possibility of population-based studies. The main technical challenge about the creation of such models concerns the detection of anatomical correspondences. Correspondences are fundamental for the calculation of principal component analysis, which is the mathematical core of statistical models. The choice of the correspondence detection technique determines the approach to be used for both the creation of statistical models and the calculation of new instances. The use of mesh morphing techniques implies the creation of a mesh-based pipeline whose output is constitute by meshes that can be directly used for finite element simulations. The use of image registration algorithms determine the generation of an image-based pipeline whose output is made of images that need to be meshed in order to be compatible with finite element tools.

A study was realized to compare image-based and mesh-based statistical appearance models. The techniques used for correspondence detection were image registration based on polyaffine demons, and mesh morphing based on radial basis functions, respectively. Two independent automatic pipelines were implemented for the calculation of each statistical appearance model and the creation of new instances. The original dataset was composed of 130 left femur CT images, and 1000 plausible femurs were created with the two pipelines. The two approaches were compared on four main aspects: quality of the correspondences, quality of the model, quality of the created finite element meshes and computational costs. From these analyses, it resulted that the mesh morphing algorithm was more successful at detecting correct correspondences on bone surface, whereas the image registration techniques had better results in bone volume. The statistical appearance

model created with the mesh-based approach described the original dataset in a more compact way than the image-based. The image-based approach had better abilities at reproducing intensities of instances that were either part of the initial dataset or external. The finite element meshes created from the image-based approach had higher quality in terms of element size, shape and volume, whereas the meshes created with the mesh-based approach were isotopological. Finally computational costs were lower for the mesh-based approach than for the image-based approach.

The comparison of the two approaches was done implementing correspondence detection techniques considered as state of the art for statistical models for bone mechanics. Since the aim of the work was to evaluate which approach could be the most suitable for the creation of valid finite element meshes, the comparison of several different techniques was beyond the aim of this study. Moreover the choice of specific morphing or registration techniques does not affect the global findings of the study, which consider the two pipelines as a whole. The original training dataset comprised not calibrated CT images. However this is a factor to be taken into account when performing finite element simulations, to proper define the mechanical properties associated to bone meshes for biomechanical studies. This study was a first step for the comparison of the two methods. A further step will consider finite element simulations.

Many questions are still to be addressed about the use of statistical appearance models in bone mechanics. The meaning of the modes of statistical models still needs to be investigated. It is commonly recognized that in statistical shape models, modes one and two represent bone length and bone torsion, respectively. However a deeper analysis would give the community a better understanding of the patterns of the bone variability described by the model. The meaning of modes of variation that describe either intensity or interaction between shape and intensities is still completely unknown and needs to be investigated. The interaction between shape and intensity, in particular, could give information about the reciprocal influence of bone shape and bone mechanical characteristics allowing prediction of bone mineral density when bone shape is known. So far, the mathematical core of statistical models has been principal component analysis. Principal component analysis describes data as a linear combination of orthogonal modes. However the variability of data could be further investigated using other non linear multivariate statistical techniques, like kernel PCA. These further analyses could contribute to a more conscious rationalisation and handling of bone variability.

Statistical appearance model for fracture risk assessment

Bone fracture risk is clinically assessed considering bone mineral density measurements from dual-emission X-ray absorptiometry (DXA) images. Further information about fracture risk evaluations are given from bone mechanical computations, where bone strains, stresses and strengths are taken into account. Strains are considered the most appropriate and reliable measurement for the assessment of bone fracture risk. Mechanical analysis is usually performed on small datasets, in patient-specific oriented studies. The introduction of statistical appearance models in bone mechanics allows the implementation of population-based studies, with the possibility of comparing various groups, created for different gender, ethnicity, age, etc. In this study, bone fracture risk was

calculated for two different groups, men and women, both in stance and sideways fall situations, in order to evaluated the different femur mechanical behavior for the two genders. Moreover, the findings were correlated to bone geometrical features, mechanical characteristics and applied loadings, to detect the influence of these factors on femur fracture risk.

A completely automatic procedure was implemented for the calculation of femur fracture risk for both men and women. Starting from 72 CT images for each gender, image-based statistical appearance models were created. The obtained models described the two different dataset with comparable compactness. A total of 1000 new instances were generated as images and converted to finite element meshes. Fracture risks were calculated in the femoral neck volume using a maximum principal strain criterion. In both configurations, stance and sideways falling, the fracture risk resulted statistically significant higher for women than for men. From the single and multiple regression analyses the body weight resulted to be the predominant factor for fracture risk prediction, both for men and women, and both in stance and sideways fall situations. Among geometrical features, the neck-shaft angle had the main role, with a predominance in the stance configuration. The femur length resulted to be a relevant factor for women. Finally, the Young's modulus resulted to have higher prediction power for men than for women.

The main limitation of this study consisted in the use of non calibrated CT images. A proper calibration of images is fundamental for a correct conversion of image grey levels to Young's modulus. However efforts were made to provide a pseudo-calibration to images and therefore obtain plausible mechanical properties. Whereas bone geometry and mechanical properties assignment are well defined, comprehensive information is still missing about physiological boundary conditions. In particular, magnitudes and directions of the applied forces due to muscles are still not completely known. However, thanks to the linear behavior of the system, it is possible to determine the load magnitude that causes bone elastic deformation, initial failure and therefore fracture.

The evaluation of mechanical fracture risk using population-based finite element simulations opens several directions of investigation. Beyond considering bone shape and density, other features could be integrated in statistical models. The considered features could regard patient characteristics not only in terms of age, height, weight, etc., but also in terms of muscle attachment points, muscle width and ligament attachment points, for example. Moreover studies could be performed on various population groups, analysing differences between Caucasian, Asian and African, or on different age groups, in order to evaluating the influence of age on bone fracture risk.

Statistical shape model for orthopaedic implant design

Bone plates are commonly designed integrating information from literature with data from cadaver studies. This results in the manufacturing of standardized plates. Therefore plates need to be contoured during surgery in order to be adapted to bone anatomy. No adjustment is done to adapt plate and screw positions to the mechanical properties of the bone undergoing surgery. The ideal solution of patient-specific plates is still unavailable due to high time and economical costs. Therefore population-based studies represent a good solution to the issue. Statistical models are

an appropriate tool to evaluate bone variability and to create new instances where this variability can be handled. In this preliminary study, bone implant fitting was assessed for two ethnic groups, Caucasian and Asian. The assessment concerned not only the anatomical shape fitting, but also a mechanical evaluation of the obtained coupling.

An image-based statistical shape model of the human tibia was created for a Caucasian and an Asian dataset. For each ethnic group, 13 instances were created as new shapes containing the dataset average intensities. The tibial 41-B1 fracture was created on the reference bone and then automatically propagated to all instances using deformation vector fields. A periarticular plate was then fitted to the fractured tibia using an automatic algorithm. The bone-plate fitting were of higher quality for Caucasian than for Asian, confirming the result expectations, since the plate had been designed for a Caucasian market. Finally mechanical simulations were performed in order to evaluate the mechanical response of the bone-plate fitting. Plates were connected to bones through screws represented as beams and embedded into the bone. Results showed that stresses in bone-implant distances and in screws were higher for Asian than for Caucasian, confirming that the available plate was more suitable for Caucasian.

This preliminary study was performed considering instances created from a statistical model of shape, where average intensities from Caucasian and Asian images were considered for each bone of the new dataset. Different mechanical properties distributions were therefore not taken into account. However preliminary results could show a difference between Caucasian and Asian in terms of mechanical response. Moreover the new created datasets were constitute by a small amount of new instances, limiting a broad range investigation. However the few instances could represent the two group general behavior both in terms of shape fitting and mechanical response.

Further interesting investigation could rise from this preliminary study. First, the automation of screw positioning both in plate and bone could allow analyzing the mechanical response of a higher number of bones. Moreover different positioning of screws could be taken into account, in order to evaluate their optimal location according to stress and strain distributions in bones. Finally the analysis of various type of fractures in different bone location could allow the creation of site-specific plates.

This thesis has shown the potential of statistical modeling for bone mechanics applications. Statistical models, combined with automatic and robust procedures, can open to a broad range of population-based investigations. Differences between genders, age groups, ethnic groups, pathological and non pathological subjects, etc. can be analyzed. Moreover statistical models can have strong influence on subject-specific studies. Parameters can be calculated to fit subjects to population models. With a small amount of data could therefore be possible to assess the characteristics of each subjects, and create useful information for clinical evaluation. Parameters could also be identified from 2D/3D reconstruction of bone structures from X-ray images, diminishing also radiation for subjects. In conclusion, the use of statistical models in bone mechanics can enhance our knowledge of bone behavior and add useful information to clinical evaluation.

Bibliography

[1] Arsigny, V., Commowick, O., Pennec, X., Ayache, N., Jan. 2006. A log-euclidean framework for statistics on diffeomorphisms. In: Medical Image Computing and Computer-Assisted Intervention - MICCAI 2006. Vol. 9. pp. 924–31.

[2] Baldwin, M. A., Langenderfer, J. E., Rullkoetter, P. J., Laz, P. J., Mar. 2010. Development of subject-specific and statistical shape models of the knee using an efficient segmentation and mesh-morphing approach. Computer Methods and Programs in Biomedicine 97 (3), 232–40.

[3] Bayraktar, H. H., Morgan, E. F., Niebur, G. L., Morris, G. E., Wong, E. K., Keaveny, T. M., Jan. 2004. Comparison of the elastic and yield properties of human femoral trabecular and cortical bone tissue. Journal of Biomechanics 37 (1), 27–35.

[4] Benameur, S., Oct. 2003. 3D/2D registration and segmentation of scoliotic vertebrae using statistical models. Computerized Medical Imaging and Graphics 27 (5), 321–337.

[5] Bergmann, G., Graichen, F., Rohlmann, A., Aug. 1993. Hip joint loading during walking and running, measured in two patients. Journal of biomechanics 26 (8), 969–90.

[6] Bergmann, G., Graichen, F., Rohlmann, A., Westerhoff, P., Heinlein, B., Bender, A., Ehrig, R., Apr. 2008. Design and calibration of load sensing orthopaedic implants. Journal of biomechanical engineering 130 (2), 021009.

[7] Blanc, R., Reyes, M., Seiler, C., Székely, G., 2009. Conditional variability of statistical shape models based on surrogate variables. In: Medical Image Computing and Computer-Assisted Intervention - MICCAI 2009.

[8] Blanz, V., Mehl, A., Vetter, T., Seidel, H.-P., 2004. A statistical method for robust 3D surface reconstruction from sparse data. In: Second International Symposium on 3D Data Processing, Visualization and Transmission - 3DPVT'04.

[9] Boichon, C., Rochette, M., Schileo, E., Grassi, L., Taddei, F., Viceconti, M., 2011. Shape indexing of human femora using morphing and principal component analysis. In: 1st Virtual Physiological Human Conference - VPH2010. No. 1.

[10] Bonaretti, S., Seiler, C., Boichon, C., Reyes, M., Büchler, P., 2011. Image-based vs. mesh-based approaches to create statistical appearance models of the human femur: Implications for finite element simulations. Submetted to Medical engineering & physics.

[11] Bou-Sleiman, H., Ritacco, L. E., Nolte, L.-P., Reyes, M., Jan. 2011. Minimization of intra-operative shaping of orthopaedic fixation plates: a population-based design. Medical Image Computing and Computer-Assisted Intervention - MICCAI 2011 14 (Pt 2), 409–16.

[12] Bredbenner, T. L., Eliason, T. D., Potter, R. S., Mason, R. L., Havill, L. M., Nicolella, D. P., Jun. 2010. Statistical shape modeling describes variation in tibia and femur surface geometry between control and incidence groups from the osteoarthritis initiative database. Journal of Biomechanics 43 (9), 1780–6.

[13] Brekelmans, W. a., Poort, H. W., Slooff, T. J., Jan. 1972. A new method to analyse the mechanical behaviour of skeletal parts. Acta orthopaedica Scandinavica 43 (5), 301–17.

[14] Bryan, R., 2010. Large scale, multi femur computational stress analysis using a statistical shape and intensity model. Ph.D. thesis, University of Southampton.

[15] Bryan, R., Mohan, P. S., Hopkins, A., Galloway, F., Taylor, M., Nair, P. B., Jan. 2010. Statistical modelling of the whole human femur incorporating geometric and material properties. Medical Engineering & Physics 32 (1), 57–65.

[16] Bryan, R., Nair, P. B., Taylor, M., Sep. 2009. Use of a statistical model of the whole femur in a large scale, multi-model study of femoral neck fracture risk. Journal of Biomechanics 42 (13), 2171–6.

[17] Büchler, P., Farron, A., 2004. Benefits of an anatomical reconstruction of the humeral head using shoulder arthroplasty: A finite element analysis. Clinical Biomechanics 19 (1), 16–23.

[18] Burge, R., Dawson-hughes, B., Solomon, D. H., Wong, J. B., King, A., Tosteson, A., 2007. Incidence and economic burden of osteoporosis-related fractures in the United States, 20052025. Journal of bone and mineral research 22 (3), 465–475.

[19] Carter, D. R., Hayes, W. C., 1977. The compressive behavior of bone as a two-phase porous structure. J Bone Joint Surgery Am 59, 954–962.

[20] Chandrupatla, T. R., Belegundu, A. D., 1991. Introduction to finite elements in engineering, 2nd Edition. Prentice Hall.

[21] Ciarelli, M. J., Goldstein, S. A., Kuhn, J. L., Cody, D. D., Brown, M. B., Sep. 1991. Evaluation of orthogonal mechanical properties and density of human trabecular bone from the major metaphyseal regions with materials testing and computed tomography. Journal of Orthopaedic Research 9 (5), 674–82.

[22] Colton, C. L., 2000. Plate fixation. http://www2.aofoundation.org/www/elearning/ modules/dlmat_ plates/dlmat_ plates_ en.htm.

[23] Colton, C. L., Dell'Oca, A. F., Holz, U., Kellam, J. F., Ochsner, P. E., 2000. AO principles of fracture management. Thieme, Stuttgart - New York.

[24] Cootes, T., Taylor, C., 2004. Statistical model of appearance for computer vision. Tech. rep., Imaging Science and Biomedical Engineering, University of Manchester.

[25] Cootes, T., Taylor, C., Cooper, D., Graham, J., 1995. Active shape models - Their training and application. Computer Vision and Image Understanding 61 (1), 38–59.

[26] Cootes, T. F., Taylor, C. J., 2001. Statistical models of appearance for medical image analysis and computer vision. In: SPIE Medical Imaging. Spie, pp. 236–248.

[27] Cowin, S. C., Doty, S. B., 2007. Tissue mechanics. Springer.

[28] Cristofolini, L., Juszczyk, M., Martelli, S., Taddei, F., Viceconti, M., Jan. 2007. In vitro replication of spontaneous fractures of the proximal human femur. Journal of biomechanics 40 (13), 2837–45.

[29] Cummings, S. R., Cawthon, P. M., Ensrud, K. E., Cauley, J. A., Fink, H. A., Orwoll, E. S., 2006. BMD and risk of hip and nonvertebral fractures in older men: A prospective study and comparison with older women. Journal of Bone and Mineral Research 21 (10), 1550–1556.

[30] Currey, J. D., 2006. Bones: structure and mechanics, 1st Edition. Princeton University Press.

[31] Davies, R., Twining, C., Taylor, C., 2008. Statistical models of shape: optimization and evaluation. Springer.

[32] de Bakker, P. M., Manske, S. L., Ebacher, V., Oxland, T. R., Cripton, P. a., Guy, P., Aug. 2009. During sideways falls proximal femur fractures initiate in the superolateral cortex: evidence from high-speed video of simulated fractures. Journal of biomechanics 42 (12), 1917–25.

[33] De Laet, C., Kanis, J. a., Odén, A., Johanson, H., Johnell, O., Delmas, P., Eisman, J. a., Kroger, H., Fujiwara, S., Garnero, P., McCloskey, E. V., Mellstrom, D., Melton, L. J., Meunier, P. J., Pols, H. a. P., Reeve, J., Silman, A., Tenenhouse, A., Nov. 2005. Body mass index as a predictor of fracture risk: a meta-analysis. Osteoporosis international 16 (11), 1330–8.

[34] De Laet, C., van Hout, B., Burger, H., Hofman, A., Pols, H., 1997. Bone density and risk of hip fracture in men and women: corss sectional analysis. British medical journal 315.

[35] Deligianni, F., Chung, A. J., Yang, G.-Z., Nov. 2006. Nonrigid 2-D/3-D registration for patient specific bronchoscopy simulation with statistical shape modeling: phantom validation. IEEE Transactions on Medical Imaging 25 (11), 1462–71.

[36] Fritscher, K. D., Grünerbl, A., Schubert, R., Feb. 2007. 3D image segmentation using combined shape-intensity prior models. International Journal of Computer Assisted Radiology and Surgery 1 (6), 341–350.

[37] Fritton, S. P., Rubin, C. T., 2001. In vivo measurement of bone deformation using strain gauges. In: Cowin, S. (Ed.), Bone mechanics handbook, 2nd Edition. Informa Healthcare, Ch. 8, p. 980.

[38] Gnudi, S., Ripamonti, C., Gualtieri, G., Malavolta, N., Aug. 1999. Geometry of proximal femur in the prediction of hip fracture in osteoporotic women. The British journal of radiology 72 (860), 729–33.

[39] Goodall, C., 1991. Procrustes methods in the statistical analysis of shape. Journal of the Royal Statistic society. Series B (Methodological) 53 (2), 285–339.

[40] Goodship, A. E., Cunningham, J. L., 2001. Pathophysiology of functional adaptation of bone in remodeling and repair in vivo. In: Cowin, S. (Ed.), Bone mechanics handbook, 2nd Edition. Informa Healthcare, Ch. 26, p. 980.

[41] Goulet, R. W., Goldstein, S. a., Ciarelli, M. J., Kuhn, J. L., Brown, M. B., Feldkamp, L. A., Apr. 1994. The relationship between the structural and orthogonal compressive properties of trabecular bone. Journal of biomechanics 27 (4), 375–89.

[42] Gray, H., 1985. Gray's anatomy, 15th Edition. Chancellor Press.

[43] Gregory, J. S., Aspden, R. M., Dec. 2008. Femoral geometry as a risk factor for osteoporotic hip fracture in men and women. Medical engineering & physics 30 (10), 1275–86.

[44] Grujicic, M., Arakere, G., Xie, X., LaBerge, M., Grujicic, A., Wagner, D., Vallejo, A., Aug. 2010. Design-optimization and material selection for a femoral-fracture fixation-plate implant. Materials & Design 31 (7), 3463–3473.

[45] Helgason, B., 2008. Subject specific finite element analysis of bone with particular application in direct skeletal attachment of a femoral prosthesis. Ph.D. thesis, University of Iceland.

[46] Helgason, B., Perilli, E., Schileo, E., Taddei, F., Brynjólfsson, S., Viceconti, M., Feb. 2008. Mathematical relationships between bone density and mechanical properties: A literature review. Clinical Biomechanics 23 (2), 135–46.

[47] Helgason, B., Taddei, F., Pálsson, H., Schileo, E., Cristofolini, L., Viceconti, M., Brynjólfsson, S., May 2008. A modified method for assigning material properties to FE models of bones. Medical Engineering & Physics 30 (4), 444–53.

[48] Heller, M. O., Bergmann, G., Deuretzbacher, G., Dürselen, L., Pohl, M., Claes, L., Haas, N. P., Duda, G. N., Jul. 2001. Musculo-skeletal loading conditions at the hip during walking and stair climbing. Journal of biomechanics 34 (7), 883–93.

[49] Heller, M. O., Bergmann, G., Kassi, J.-P., Claes, L., Haas, N. P., Duda, G. N., May 2005. Determination of muscle loading at the hip joint for use in pre-clinical testing. Journal of biomechanics 38 (5), 1155–63.

[50] Hraiech, N., 2010. Mesh morphing and shape indexing in human femur modeling applications. Ph.D. thesis, Université de Rennes.

[51] Hraiech, N., Boichon, C., Rochette, M., Marchal, T., Horner, M., 2010. Statistical shape modeling of femurs using morphing and principal component analysis. J. Med. Devices 4 (June), 27534.

[52] Huiskes, R., Chao, E. Y. S., 1983. A Survey of Finite Element Analysis in Orthopedic Biomechanics: The First Decade. J Biomechanics 16 (6), 385–409.

[53] Huiskes, R., Hollister, S. J., Dec. 1993. From structure to process, from organ to cell: recent developments of FE-analysis in orthopaedic biomechanics. Journal of biomechanical engineering 115 (4B), 520–7.

[54] Humbert, L., Whitmarsh, T., De Craene, M., del Rio Barquero, L. M., Fritscher, K., Schubert, R., Eckstein, F., Link, T., Frangi, A. F., 2010. 3D reconstruction of both shape and bone mineral density distribution of the femur from DXA images. 2010 IEEE International Symposium on Biomedical Imaging: From Nano to Macro, 456–459.

[55] Jee, W. S. S., 2001. Integrated bone tissue physiology: Anatomy and physiology. In: Cowin, S. C. (Ed.), Bone mechanics handbook, 2nd Edition. Vol. 56. Informa Healthcare, Ch. 1, p. 980.

[56] Johnell, O., Kanis, J. a., Dec. 2006. An estimate of the worldwide prevalence and disability associated with osteoporotic fractures. Osteoporosis international : a journal established as result of cooperation between the European Foundation for Osteoporosis and the National Osteoporosis Foundation of the USA 17 (12), 1726–33.

[57] Jolliffe, I., 1986. Principal Component Analysis. Springer, New York.

[58] Kanis, J. a., Borgstrom, F., De Laet, C., Johansson, H., Johnell, O., Jonsson, B., Oden, A., Zethraeus, N., Pfleger, B., Khaltaev, N., Jun. 2005. Assessment of fracture risk. Osteoporosis international : a journal established as result of cooperation between the European Foundation for Osteoporosis and the National Osteoporosis Foundation of the USA 16 (6), 581–9.

[59] Kaufman, J. J., Siffert, R. S., 2001. Noninvasive measurement of bone integrity. In: Cowin, S. (Ed.), Bone mechanics handbook2, 2nd Edition. Informa Healthcare, Ch. 34, p. 980.

[60] Keaveny, T. M., Bouxsein, M. L., 2008. Theoretical Implications of the Biomechanical Fracture Threshold. Journal of Bone and Mineral Research 23 (10), 1541–1547.

[61] Keaveny, T. M., Wachtel, E. F., Ford, C. M., Hayes, W. C., Sep. 1994. Differences between the tensile and compressive strengths of bovine tibial trabecular bone depend on modulus. Journal of biomechanics 27 (9), 1137–46.

[62] Keyak, J. H., Lee, I. Y., Skinner, H. B., 1994. Correlations between orthogonal mechanical properties and density of trabecular bone: use of different densitometric measures. Journal of Biomedical Materials Research 28, 1329–1339.

[63] Keyak, J. H., Meagher, J. M., Skinner, H. B., Mote, C. D., Sep. 1990. Automated three-dimensional finite element modelling of bone: a new method. Journal of biomedical engineering 12 (5), 389–97.

[64] Keyak, J. H., Rossi, S. A., 2000. Prediction of femoral fracture load using finite element models: an examination of stress- and strain-based failure theories. Society 33, 209–214.

[65] Keyak, J. H., Rossi, S. a., Jones, K. a., Skinner, H. B., Feb. 1998. Prediction of femoral fracture load using automated finite element modeling. Journal of biomechanics 31 (2), 125–33.

[66] Keyak, J. H., Sigurdsson, S., Karlsdottir, G., Oskarsdottir, D., Sigmarsdottir, A., Zhao, S., Kornak, J., Harris, T. B., Sigurdsson, G., Jonsson, B. Y., Siggeirsdottir, K., Eiriksdottir, G., Gudnason, V., Lang, T. F., Jun. 2011. Male-female differences in the association between incident hip fracture and proximal femoral strength: a finite element analysis study.

[67] Kopperdahl, D. L., Keaveny, T. M., Jul. 1998. Yield strain behavior of trabecular bone. Journal of biomechanics 31 (7), 601–8.

[68] Kozic, N., Weber, S., Büchler, P., Lutz, C., Reimers, N., González Ballester, M. A., Reyes, M., Jun. 2010. Optimisation of orthopaedic implant design using statistical shape space analysis based on level sets. Medical Image Analysis 14 (3), 265–275.

[69] Lamecker, H., Lange, T., Seebass, M., 2002. A statistical shape model for the liver. In Medical Image Computing and Computer-Assisted Intervention - MICCAI 2002, 421–427.

[70] Lang, T. F., 2010. Quantitative Computed Tomography. Radiologic Clinics of NA 48 (3), 589–600.

[71] Laz, P. J., Stowe, J. Q., Baldwin, M. a., Petrella, A. J., Rullkoetter, P. J., Jan. 2007. Incorporating uncertainty in mechanical properties for finite element-based evaluation of bone mechanics. Journal of Biomechanics 40 (13), 2831–6.

[72] Liu, T., Shen, D., Davatzikos, C., 2004. Predictive modeling of anatomic structures using canonical correlation analysis. In: International Symposium on Biomedical Imaging: Nano to Macro, 2004. IEEE.

[73] Lorensen, W. E., Cline, H. E., 1987. Marching cubes: A high resolution 3D surface construction algorithm. Computer Graphics 21 (4), 163–169.

[74] Lötjönen, J., Kivistö, S., Koikkalainen, J., Smutek, D., Lauerma, K., Sep. 2004. Statistical shape model of atria, ventricles and epicardium from short- and long-axis MR images. Medical Image Analysis 8 (3), 371–86.

[75] Lotz, J., Cheal, E., Hayes, W., 1991. Fracture prediction for the proximal femur using finite element models: Part II - non linear analysis. Journal of biomechanical engineering 113, 361–365.

[76] Marks, S. C., Odgren, P. R., 1996. Structure and development of the skeleton. In: Bilezikian, J. P., Raisz, L. G., Rodan, G. A. (Eds.), Principles of bone biology. Ch. 1, p. 1398.

[77] McBroom, R. J., Hayes, W. C., Edwards, W. T., Goldberg, R. P., White, A. A., 1985. Prediction of vertebral body compressive fracture using quantitative computed tomography. The journal of bone and joint surgery. 67 (8), 1206–1214.

[78] McLeod, K. J., Rubin, C. T., 1992. The effect of low-frequency on osteogenesis. The Journal of bone and joint surgery. 8, 920–929.

[79] Miller, M. I., Trouve, A., Younes, L., Jan. 2002. On the metrics and euler-lagrange equations of computational anatomy. Annual Review of Biomedical Engineering 4, 375–405.

[80] Morgan, E., Bayraktar, H., Keaveny, T., Jul. 2003. Trabecular bone modulusdensity relationships depend on anatomic site. Journal of Biomechanics 36 (7), 897–904.

[81] Müller, M., Allgower, M., Schneider, R., 1979. Manual of internal fixation: technique recommended by the A.O. group. Springer-Verlag, New-York.

[82] Netter, F. H., 2002. Atlas of human anatomy, 3rd Edition. Saunders.

[83] Orwoll, E. S., Marshall, L. M., Nielson, C. M., Cummings, S. R., Lapidus, J., Cauley, J. A., Ensrud, K., Lane, N., Hoffmann, P. R., Kopperdahl, D. L., Keaveny, T. M., 2009. Finite Element Analysis of the Proximal Femur and Hip Fracture Risk in Older Men. Journal of bone and mineral research 24 (3), 475–483.

[84] Oxford University Press, Jul. 2009. 6. Quantitative Computed Tomography. Journal of the ICRU 9 (1), 59–69.

[85] Paulsen, R. R., Baerentzen, J. A., Larsen, R., 2010. Markov random field surface reconstruction. IEEE Transactions on Visualization and Computer Graphics 16 (4), 636–46.

[86] Paulsen, R. R., Nielsen, C., Laugesen, S., Larsen, R., 2004. Using a shape model in the design of hearing aids. SPIE - Medical Imaging.

[87] Pinilla, T. P., Boardman, K. C., Bouxsein, M. L., Myers, E. R., Hayes, W. C., 1996. Impact direction from a fall influences the failure load of the proximal femur as much as age-related bone loss. Journal of Bone and Mineral Research 58, 231–235.

[88] Prendergast, P., Sep. 1997. Finite element models in tissue mechanics and orthopaedic implant design. Clinical Biomechanics 12 (6), 343–366.

[89] Querol, L., Büchler, P., Rueckert, D., Nolte, L., 2006. Statistical finite element model for bone shape and biomechanical properties. In: Medical Image Computing and Computer-Assisted Intervention - MICCAI 2006. pp. 405 – 411.

[90] Rajamani, K. T., Styner, M., Talib, H., Zheng, G., Nolte, L. P., González Ballester, M. A., Apr. 2007. Statistical deformable bone models for robust 3D surface extrapolation from sparse data. Medical Image Analysis 11 (2), 99–109.

[91] Rao, A., Aljabar, P., Rueckert, D., Feb. 2008. Hierarchical statistical shape analysis and prediction of sub-cortical brain structures. Medical Image Analysis 12 (1), 55–68.

[92] Reilly, D. T., Burstein, a. H., Jan. 1975. The elastic and ultimate properties of compact bone tissue. Journal of biomechanics 8 (6), 393–405.

[93] Rho, J. Y., Kuhn-Spearing, L., Zioupos, P., Mar. 1998. Mechanical properties and the hierarchical structure of bone. Medical engineering & physics 20 (2), 92–102.

[94] Rubin, C. T., Lanyon, L. E., 1984. Regulation of bone formation by applied dynamic loads. J Bone Joint Surgery Am 66, 397–402.

[95] Rubin, C. T., Sommerfeldt, D. W., Judex, S., Qin, Y. X., Aug. 2001. Inhibition of osteopenia by low magnitude, high-frequency mechanical stimuli. Drug discovery today 6 (16), 848–858.

[96] Rueckert, D., Aljabar, P., Heckemann, R. a., Hajnal, J. V., Hammers, A., Jan. 2006. Diffeomorphic registration using B-splines. Medical Image Computing and Computer-Assisted Intervention - MICCAI 2006 9 (Pt 2), 702–9.

[97] Rueckert, D., Frangi, A. F., Schnabel, J., Aug. 2003. Automatic construction of 3-D statistical deformation models of the brain using nonrigid registration. IEEE Transactions on Medical Imaging 22 (8), 1014–25.

[98] Rueckert, D., Sonoda, L. I., Hayes, C., Hill, D. L., Leach, M. O., Hawkes, D. J., Aug. 1999. Nonrigid registration using free-form deformations: Application to breast MR images. IEEE Transactions on Medical Imaging 18 (8), 712–21.

[99] Schileo, E., Dall'Ara, E., Taddei, F., Malandrino, A., Schotkamp, T., Baleani, M., Viceconti, M., Aug. 2008. An accurate estimation of bone density improves the accuracy of subject-specific finite element models. Journal of Biomechanics 41 (11), 2483–91.

[100] Schileo, E., Taddei, F., Cristofolini, L., Viceconti, M., Jan. 2008. Subject-specific finite element models implementing a maximum principal strain criterion are able to estimate failure risk and fracture location on human femurs tested in vitro. Journal of Biomechanics 41 (2), 356–67.

[101] Schileo, E., Taddei, F., Malandrino, A., Cristofolini, L., Viceconti, M., Jan. 2007. Subject-specific finite element models can accurately predict strain levels in long bones. Journal of biomechanics 40 (13), 2982–9.

[102] Schiuma, D., Brianza, S., Tami, a. E., Mar. 2011. Development of a novel method for surgical implant design optimization through noninvasive assessment of local bone properties. Medical engineering & physics 33 (2), 256–62.

[103] Schmid, J., Magnenat-Thalmann, N., 2008. MRI bone segmentation using deformable models and shape priors. In: Medical Image Computing and Computer-Assisted Intervention - MICCAI 2008. pp. 562–569.

[104] Schnabel, J. A., Rueckert, D., Quist, M., Blackall, J. M., Castellano-Smith, A. D., Hartkens, T., Penney, G. P., Hall, W. A., Liu, H., Truwit, C. L., Gerritsen, F. A., Hill, D. L. G., Hawkes, D. J., 2001. A generic framework for non-rigid registration based on non-uniform multi-level free-form deformations. In: Medical Image Computing and Computer-Assisted Intervention - MICCAI 2001. Utrecht, NL, pp. 573–581.

[105] Schöberl, J., 1997. NETGEN An advancing front 2D/3D-mesh generator based on abstract rules. Computing and Visualization in Science 1, 41–52.

[106] Schuler, B., Fritscher, K. D., Kuhn, V., Eckstein, F., Link, T. M., Schubert, R., 2010. Assessment of the individual fracture risk of the proximal femur by using statistical appearance models. Medical Physics 37 (6), 2560–2571.

[107] Seiler, C., Pennec, X., Ritacco, L., Reyes, M., 2011. Femur specific polyaffine model to regularize the log-domain demons registration. In: In SPIE Medical Imaging. Vol. 7962.

[108] Speirs, A. D., Heller, M. O., Duda, G. N., Taylor, W. R., Jan. 2007. Physiologically based boundary conditions in finite element modelling. Journal of biomechanics 40 (10), 2318–23.

[109] Styner, M., Gerig, G., Lieberman, J., Jones, D., Weinberger, D., Sep. 2003. Statistical shape analysis of neuroanatomical structures based on medial models. Medical Image Analysis 7 (3), 207–20.

[110] Summerlee, A., 2002. Bone formation and development. In: Sumner-Smith, G. (Ed.), Bone in clinical orthopedics, 2nd Edition. Thieme, Ch. 1, pp. 1–20.

[111] Taddei, F., Pancanti, A., Viceconti, M., Jan. 2004. An improved method for the automatic mapping of computed tomography numbers onto finite element models. Medical Engineering & Physics 26 (1), 61–69.

[112] Taddei, F., Schileo, E., Helgason, B., Cristofolini, L., Viceconti, M., Nov. 2007. The material mapping strategy influences the accuracy of CT-based finite element models of bones: an evaluation against experimental measurements. Medical engineering & physics 29 (9), 973–9.

[113] Taylor, B. C., Schreiner, P. J., Stone, K. L., Fink, H. a., Cummings, S. R., Nevitt, M. C., Bowman, P. J., Ensrud, K. E., Sep. 2004. Long-term prediction of incident hip fracture risk in elderly white women: study of osteoporotic fractures. Journal of the American Geriatrics Society 52 (9), 1479–86.

[114] Testi, D., Viceconti, M., Baruffaldi, F., Cappello, A., Jul. 1999. Risk of fracture in elderly patients: a new predictive index based on bone mineral density and finite element analysis. Computer methods and programs in biomedicine 60 (1), 23–33.

[115] Turner, C. H., Burr, D. B., 2001. Experimental techniques for bone mechanics. In: Cowin, S. C. (Ed.), Bone mechanics handbook, 2nd Edition. Informa Healthcare, Ch. 7, p. 980.

[116] Tustison, N. J., Gee, J. C., 2009. Introducing dice , jaccard , and other label overlap measures to ITK. Insight Journal.

[117] Valliappan, S., Svensson, N. L., Wood, R. D., Oct. 1977. Three dimensional stress analysis of the human femur. Computers in biology and medicine 7 (4), 253–64.

[118] Vercauteren, T., Pennec, X., Perchant, A., Ayache, N., Jan. 2008. Symmetric log-domain diffeomorphic registration: A demons-based approach. Medical Image Computing and Computer-Assisted Intervention - MICCAI 2008 11, 754–61.

[119] Vercauteren, T., Pennec, X., Perchant, A., Ayache, N., Mar. 2009. Diffeomorphic demons: efficient non-parametric image registration. NeuroImage 45 (1 Suppl), S61–72.

[120] Viceconti, M., Bellingeri, L., Cristofolini, L., Toni, A., Jan. 1998. A comparative study on different methods of automatic mesh generation of human femurs. Medical engineering & physics 20 (1), 1–10.

[121] Viceconti, M., Davinelli, M., Taddei, F., Cappello, A., Oct. 2004. Automatic generation of accurate subject-specific bone finite element models to be used in clinical studies. Journal of Biomechanics 37 (10), 1597–605.

[122] Villarraga, M. L., Ford, C. M., 2001. Applications of bone mechanics. In: Cowin, S. (Ed.), 2Bone mechanics handbook, 2nd Edition. Informa Healthcare, Ch. 33, p. 980.

[123] Wirtz, D. C., Schiffers, N., Pandorf, T., Radermacher, K., Weichert, D., Forst, R., Oct. 2000. Critical evaluation of known bone material properties to realize anisotropic FE-simulation of the proximal femur. Journal of biomechanics 33 (10), 1325–30.

[124] Wolff, J., 1892. Das gesetz der trasformation der knochen. Springer, Berlin.

[125] Yao, J., Taylor, R., 2000. Tetrahedral mesh modeling of density data for anatomical atlases and intensity-based registration. In: Medical Image Computing and Computer-Assisted Intervention - MICCAI 2000. Pittsburgh, PA, USA, pp. 531–540.

[126] Yao, J., Taylor, R., 2003. Assessing accuracy factors in deformable 2D/3D medical image registration using a statistical pelvis model. In: Proceeding of the Ninth IEEE International Conference on Computer Vision - ICCV 2003. Vol. 2. pp. 1329–1334.

[127] Zannoni, C., Mantovani, R., Viceconti, M., Dec. 1998. Material properties assignment to finite element models of bone structures: a new method. Medical Engineering & Physics 20 (10), 735–40.

[128] Zheng, G., 2010. Statistical shape model-based reconstruction of a scaled, patient-specific surface model of the pelvis from a single standard AP x-ray radiograph. Medical Physics 37, 1424–1439.

[129] Zheng, G., Gollmer, S., Schumann, S., Dong, X., Feilkas, T., González Ballester, M. A., Dec. 2009. A 2D/3D correspondence building method for reconstruction of a patient-specific 3D bone surface model using point distribution models and calibrated X-ray images. Medical Image Analysis 13 (6), 883–99.

Resume

Personal data

Name	Serena Bonaretti
Date of birth	March 12, 1981
Place of birth	Novara, Italy
Nationality	Italian

Education

2008- 2011	PhD student at the Institute for Surgical Technology and Biomechanics, University of Bern, Switzerland
2003-2005	M.Sc. in Biomedical Engineering, Politecnico di Milano, Italy
2000-2003	B.Sc. in Biomedical Engineering, Politecnico di Milano, Italy

Work experience

2005-2007	Clinical engineer at Fondazione Audiologica Varese ONLUS, Ospedale di Circolo-Fondazione Macchi, Varese, Italy
2003,2005	Assistant researcher at Institute of Biomedical Engineering (ISIB CNR), Milano, Italy

Publications

Journal papers

Bonaretti, S., Seiler, C., Boichon, C., Reyes, M., Büchler, P., 2011. Image-based vs. mesh-based approaches to create statistical appearance models of the human femur: Implications for finite element simulations. Submitted To Medical engineering and physics.

Conf. papers

Bonaretti, S., Seiler, C., Boichon, C., Büchler, P., Reyes, M., 2011. Mesh-based vs . image-based statistical appearance model of the human femur : A preliminary comparison study for the creation of finite element meshes. In: Mesh Processing in Medical Image Analysis - MICCAI 2011 workshop. Toronto, Ontario, Canada.

Bonaretti, S., Kistler, M., Seiler, C., Reyes, M., Buechler, P., 2010. Combined statistical model of bone shape and mechanical properties for bone and implant modeling. In: 9th International Symposium on Computer Methods in Biomechanics and Biomedical Engineering. Valencia, Spain.

Bonaretti, S., Reimers, N., Reyes, M., Nikitsin, A., Joensson, A., Nolte, L., Büchler, P., Jul. 2008. Assessment of Peri-Articular Implant Fitting Based on

Statistical Finite Element Modeling. In: Workshop on Computational Biomechanics for Medicine III - MICCAI 2008. New York, New York, USA.

Conf. abstracts

Sigurardóttir, B., Bonaretti, S., Örlygsson, G., Sigurjónsson, O. E., Ferguson, S., Helgason, B., 2011. Are iso-elastic femoral stems beneficial for secondary implant stability in cementless THA? In: The Annual Meeting of the Swiss Society for Biomedical Engineering. No. 1. Bern, Switzerland.

Bonaretti, S., Helgason, B., Seiler, C., Kistler, M., Reyes, M., Büchler, P., 2010. A statistical shape model of bone anatomical variability for finite element assessment of bone mechanics. In: Proceedings of the 17th Congress of the European Society of Biomechanics. Vol. 39. Edinburgh, Scotland.

Bonaretti, S., Seiler, C., Büchler, P., Reyes, M., Technology, S., 2009. Computing average anatomical images: Comparison between thin plate spline and log-euclidean approach. In: The Annual Meeting of the Swiss Society for Biomedical Engineering. Vol. 11. Bern, Switzerland, pp. 5416–5416.

Bonaretti, S., Büchler, P., Reimers, N., Schmidt, W., Seiler, C., Weber, S., Reyes, M., 2009. Automatic bone density evaluation from CT images. In: Computer Assisted Orthopaedic Surgery. Boston, Massachusetts, USA.

Bonaretti, S., Reimers, N., Rückert, D., Reyes, M., González, M., Büchler, P., Jul. 2008. Statistical Finite Element Analysis for Bone Modeling. In: 16th Congress European Society of Biomechanics. Vol. 41. Luzern, Switzerland, p. S369.

Declaration of Originality

Last name, first name: Bonaretti, Serena
Matriculation number: 07-130-412

I hereby declare that this thesis represents my original work and that I have used no other sources except as noted by citations. All data, tables, figures and text citations which have been reproduced from any other source, including the internet, have been explicitly acknowledged as such.

I am aware that in case of non-compliance, the Senate is entitled to divest me of the doctorate degree awarded to me on the basis of the present thesis, in accordance with the Statut der Universität Bern (Universitätsstatut; UniSt), Art. 20, of 17 December 1997.

Place, date	Signature
.....	.....